Dissertation

Chiral and Deconfinement Phase Transitions in $N_f = 2$ and $N_f = 2+1$ Quantum Chromodynamics

Jan Lücker

July 2013

Justus-Liebig-Universität Gießen
Fachbereich 7
Institut für theoretische Physik

Contents

Contents

1 Introduction

In the standard model of particle physics, fermionic matter is divided into two categories, leptons and quarks. While all of these have a charge with respect to the electroweak interaction, by definition only quarks have a charge under the strong nuclear force, *i.e.* a colour charge. This seemingly small difference leads to a nature of the quarks that is drastically different from that of the leptons. While the latter can be detected directly in detectors, quarks can not – they are confined in bound states, the hadrons. Explaining the spectrum of hadrons had been the initial motivation for introducing the quark model. However, when quarks where introduced by Gell-Mann and Zweig in 1964 [1, 2], they where not believed in as physical particles, but a mere mathematical trick. This is of course owed to the alleged property of confinement which means that the existence of quarks can never be proven directly in an experiment.

That quarks are indeed more than a counting scheme has been realised when deep inelastic scattering of electrons on nucleons confirmed a sub-structure of hadrons that matched the prediction of the quark model. [3, 4] The structure of hadrons is, after the general hadron spectrum, the second way how we can test the quark model, especially its modern interpretation in terms of a quantum field theory, quantum chromodynamics (QCD).

The third way was first proposed in 1975 [5, 6], when it was realised that the quark model predicts a new state of matter that exists at high temperatures or densities. In these extreme conditions confinement is lost, and quarks and gluons form a plasma. These conditions are believed to have existed about 14 billion years ago, when the universe was in a very hot and dense state, as well as in the interior of neutron stars. The experimental creation of this form of matter is the driving force behind the programme of heavy-ion collision. Evidence for the existence of the quark-gluon plasma has been found in the SPS experiment at CERN [7], in RHIC at BNL [8], and most recently at the LHC (CERN) [9]. This makes the experimental evidence for such a phase an important pillar of our modern believe in the existence of quarks, and the exploration of high temperatures and densities an excellent testing ground of QCD.

Not only on the experimental, but also on the theory side, describing the phases of QCD is an ongoing endeavour. This is due to the complex structure of this theory, and especially its strong coupling. This is a problem for standard perturbative schemes which rely on a small coupling. Owing to asymptotic freedom, they can thus be applied at large energy scales, but not in the infrared. However, many interesting phenomena are found in the infrared, *i.e.* in non-perturbative QCD. Most importantly there is the dynamical generation of quark mass (dynamical chiral symmetry breaking) and

confinement. The existence of both is firmly established, although for confinement this is only true in the limit of infinitely heavy quarks. The interrelation between those two phenomena is also not well understood today. There are examples of theories with dynamically broken chiral symmetry but without confinement, like strongly-coupled QED or the Nambu–Jona-Lasinio model. In three-dimensional QED a logarithmic potential gives rise to confinement, while chiral symmetry is not necessarily broken.

There are speculations that QCD at large density [10] or magnetic field [11] might be in a state of restored chiral symmetry but with confinement, however the existence of this new phase is not proven yet.

At some large temperature both phenomena are known to vanish. In simulations of full QCD at zero density on a lattice it has been established [12,13] that the transition temperature for both, chiral symmetry restoration and deconfinement, are near-by. It has also been established that the transition is a cross-over for physical quark masses. If one allows the light and strange quark masses to vary, this is not always the case. In the limit of infinitely heavy quarks (thus in the pure Yang-Mills theory) one finds a first order phase transition. The same is true in the opposite limit of three massless quarks, where one has a first order chiral phase transition. On the other hand, the deconfinement transition in this case is not well defined.[1] The situation for two massless quarks is not resolved yet. If one assumes that the $U_A(1)$-anomaly is broken at the critical temperature, one finds a second order phase transition. On the other hand, a restored anomaly is believed to lead to a phase transition of first order. This situation is summarised in Fig. (1.1).
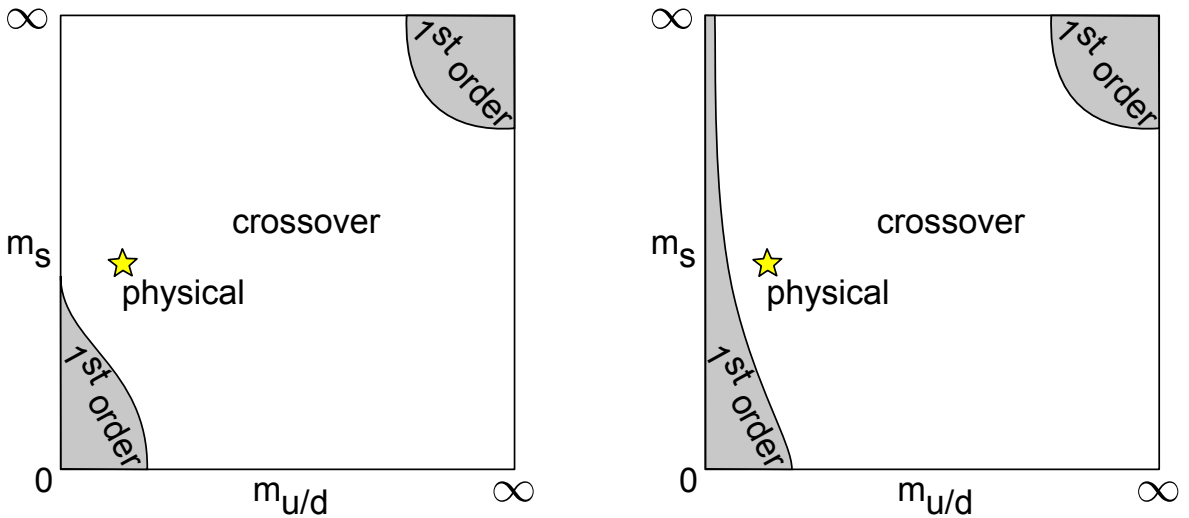
Figure 1.1: So-called "Columbia plot" [14], the conjectured phase diagram in $m_{u/d}$-m_s space. In the version to the left, the anomaly is not restored, in the version to the right it is.

---

[1] In the sense of a linear rising potential / vanishing Polyakov loop.

When we now turn to a finite net quark density, lattice simulations are running into the so-called fermion sign problem, see e.g. [15] for a review. This prohibits the direct evaluation of large densities on the lattice. One way of dealing with this situation is to extrapolate from zero to finite density, which yields valuable insights in the phase diagram at small densities. [16, 17]

In the past, a large effort was made to apply effective field theories to the problem of the phase diagram. One example is the Nambu–Jona-Lasinio (NJL) model, see [18] for a review. In the NJL model the gluon degrees of freedom are replaced by an effective four-fermion coupling. This yields a theory that is technically much easier to treat than QCD. The same holds for quark-meson models, where mesonic degrees of freedom are explicitly taken into account, see for example [19]. To amend for the gluonic sector of QCD, these models where extended to include Polyakov-loop variables. This yields the Polyakov-loop extended NJL (PNJL) [20–22] and quark-meson (PQM) [23–25] models.
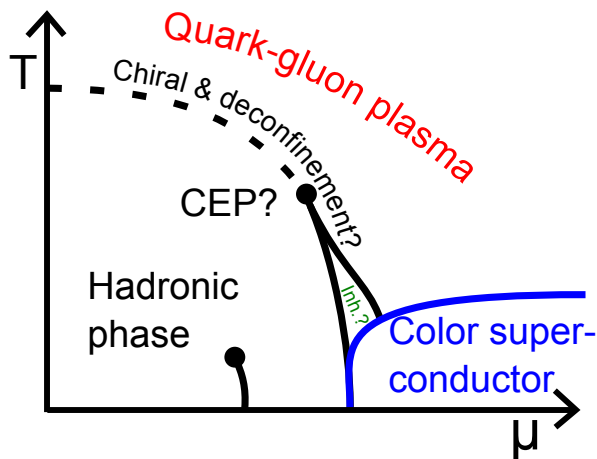
Figure 1.2: A sketched phase diagram in the $\mu - T$ plane.

In studies of effective field theories a picture for the phase diagram has emerged that we show in Fig. (1.2). There, one finds a cross-over for the chiral transition at small chemical potentials, that turns into a first order phase transition at a second order critical end-point (CEP). The existence and position of the CEP depends strongly on the parameters used in the model studies. In lattice QCD, a CEP has been reported e.g. in [26] and [27]. However, the lattices in those studies where rather coarse. It is also under debate whether the extrapolation methods in those works can be trusted at the chemical potentials where the CEP is found. In a different approach, the line separating the crossover from the first order region in Fig. (1.1) has been extended to finite chemical potential e.g. in [28]. There, the first order region tends to shrink with chemical potential. This is in contrast to the standard picture, where this region grows until the physical point is inside the first order region. In consequence these results hint against the existence of a CEP at least at not too large density. On the other hand, the critical surface could bend back at larger density, or the critical end-point

might not be connected to this surface at all. We therefore can not reliably determine the existence and position of the CEP from the lattice yet.

At large densities at least one colour-superconducting phase appears, as can be shown from studies at asymptotically large density. See e.g. [29] for a review on the colour-superconducting phases. The area at low temperatures and medium densities is the one least understood in the phase diagram. One new phase that might appear is an inhomogeneous phase with space-dependent condensate, see e.g. [30, 31]. In this area the effects of baryons are also believed to be important, which poses the difficult question on how to include baryon and quark degrees of freedom in the same model.

Clearly, our methods of accessing the phase diagram are limited today, and we need to develop complementary approaches to refine our understanding of in-medium QCD. One set of non-perturbative frameworks that can be applied to QCD are the functional methods, like the functional renormalisation group (FRG) and the Dyson-Schwinger equations (DSEs). In contrast to the effective models, the functional methods yield tools to directly describe the Yang-Mills sector of QCD. The idea is to use functional relations to obtain infinite sets of equations that describe QCD (or any other quantum field theory) exactly. For most practical purposes, however, we have to apply a truncation scheme which cuts the infinite tower of equations and yields a finite solvable set which approximates full QCD. The FRG method for QCD has been used in [32] to study finite temperature and imaginary chemical potential. In [33] the gluon and ghost propagators have been studied in quenched QCD. Determining the phase diagram at real chemical potential from the FRG equations of QCD is an ongoing effort.

From Dyson-Schwinger equations some fundamental work concerning the QCD phase diagram has been done in [34], and references therein. In [35] the colour-superconducting phases at zero temperature and in [36, 37] also at finite temperature have been studied. The pure Yang-Mills sector was subject of a study in [38, 39]. Also in the quenched case, the DSEs have been used to study the confinement-deconfinement transition in [40–42]. This was the starting point to also include dynamical quarks and finite chemical potential [43, 44], which is the line of work that we will continue here.

The idea in this work is to employ the quark and gluon Dyson-Schwinger equations at finite temperature and chemical potential to study the phase transitions of QCD. In general, from DSEs the quark sector is more accessible than the Yang-Mills sector. The opposite is true in lattice QCD; there, light fermions are expensive and a finite chemical potential only accessible by extrapolation methods while quenched QCD is comparatively cheap. We will exploit this complementarity by using lattice results for the quenched gluon propagator and the DSEs for the quark and unquenched gluon propagators. This allows us to study the interrelation of quarks and gluons at all temperatures and chemical potentials. This is novel, since previous studies relied on simpler approximations for the gluon input to the quark DSE. Also, in effective models the coupling of quarks and gluons can only be described effectively by the Polyakov-loop potential. From solutions of our truncated set of DSEs we can then study the chiral and deconfinement phase transitions. As an order parameter for the chiral transition

we will use the quark condensate, while for the confinement-deconfinement transition an order parameter is much harder to access from DSEs. We will therefore use and contrast different ways of describing confinement from the propagators. These are the so-called dressed Polyakov loop, the Polyakov-loop potential and we shortly discuss positivity violations in the quark spectral function.

This work is organised as follows: In chapter 2 we will discuss some general properties of QCD. In chapter 3 our order parameters for chiral symmetry breaking and confinement will be introduced. We then turn towards our truncation scheme and discuss our choice for the quark-gluon vertex in chapter 4. In the same chapter we also discuss some technicalities of solving the quark DSE in the medium. In the following three chapters we will concentrate on different gluon propagators as an input for the quark DSE. In chapter 5 the quenched case will be discussed, which serves as a cross-check for our methods and as an input for the following work on unquenching the gluon. In chapter 6 we will introduce an HTL/HDL-like truncation scheme for the unquenched gluon propagator and study the resulting phase diagram. This truncation will be improved in chapter 7, where the non-perturbatively unquenched gluon DSE will be introduced. With the unquenched gluon we study the chiral and deconfinement phase transitions and obtain the phase diagrams for $N_f = 2$ and $N_f = 2+1$ QCD. The results for the propagators will be used in chapter 8 to study the Polyakov-loop potential. We will further improve our truncation scheme in chapter 9 where we will include Goldstone modes explicitly. In chapter 10 we will summarise and give an outlook.

2 Quantum chromodynamics

2.1 General properties

Quantum chromodynamics can be derived as a non-Abelian gauge theory for the gauge group $SU(3)$, where three is the number of colours. It is insightful to also study generalisations to two colours, which we will briefly do in chapter 5. This is especially of interest at finite chemical potential, where $SU(2)$ lattice studies are not plagued by the fermion sign problem. [45] It is also useful to take the limit of infinitely many colours, where the theory becomes much simpler. This case is also frequently studied by use of the gauge/gravity duality. For the rest of this chapter we can safely assume the general case of an $SU(N_c)$ gauge group, with generators T^a. In Euclidean space-time (see appendix A for our conventions), the Lagrangian of QCD is given by

$$\mathcal{L}_{QCD} = \bar{q}\left(-\slashed{D} + M\right)q - \frac{1}{4}\mathrm{Tr}_c F_{\mu\nu}F_{\mu\nu}, \tag{2.1}$$

with quark fields $q = (u, d, s, \dots)$, the quark mass matrix $M = \mathrm{diag}(m_u, m_d, m_s, \dots)$, the covariant derivative $D_\mu = \partial_\mu + \mathrm{i}gA_\mu$, the field-strength tensor $F_{\mu\nu} = [D_\mu, D_\nu]$ and the gauge-fields $A_\mu = A_\mu^a T^a$. The Lagrangian in Eq. (2.1) is not the most general Lagrangian that satisfies gauge symmetry and renormalisability. An additional term $\propto \theta F_{\mu\nu}\tilde{F}_{\mu\nu}$ with $\tilde{F}_{\mu\nu} = \epsilon_{\mu\nu\sigma\rho}F_{\sigma\rho}$ is also allowed. This θ-term is CP violating, and has been shown to be close to zero, since it would give rise to an electric dipole moment for the neutron, which is experimentally disfavoured [46, 47]. It is therefore usually neglected, which we will also do here.

With the Lagrangian in Eq. (2.1) we can define the generating functional of QCD as

$$Z_{QCD}[\eta, \bar{\eta}, j] = \int \mathcal{D}\psi \mathcal{D}\bar{\psi}\mathcal{D}A \exp\left(-\int d^4x \mathcal{L}_{QCD} + \bar{\eta}\psi + \bar{\psi}\eta + jA\right), \tag{2.2}$$

where we introduced Graßmannian sources η and $\bar{\eta}$ for the fermion fields and the source j_μ for the gauge field.

The QCD Lagrangian is by construction gauge-invariant, that is under a transformation

$$q \rightarrow V(x)q, \tag{2.3}$$

$$A_\mu \rightarrow V(x)A_\mu V^\dagger(x) - (\partial_\mu V(x))V^\dagger(x), \tag{2.4}$$

for a local gauge transformation $V(x) \in SU(N_c)$. In the generating functional, Eq. (2.2), all configurations of A_μ are taken into account. Since gauge fields that are connected

via a gauge transformation, Eq. (2.4), have the same physical content, this leads to over-counting. This necessitates the procedure of gauge fixing, *i.e.* of picking one field configuration from the gauge orbit. This procedure is conventionally done along the lines of Fadeev-Popov, see e.g. [48]. The result in a covariant gauge with gauge parameter ξ is

$$\mathcal{L}_{g.f.} = \bar{q}\left(-\not{D} + M\right)q - \frac{1}{4}\text{Tr}_c F_{\mu\nu}F_{\mu\nu} + \frac{1}{2\xi}\text{Tr}_c\partial_\mu A_\mu\partial_\nu A_\nu + \mathrm{i}\bar{c}\partial_\mu D_\mu c, \qquad (2.5)$$

with the ghost fields $c, \bar{c}$. We will use Landau gauge throughout this work, which is defined by taking the limit

$$\xi \to 0. \qquad (2.6)$$

Gribov has shown in [49] that the Fadeev-Popov method of gauge fixing is incomplete. Even in the gauge-fixed theory, the gauge fields are not unique, but multiple Gribov copies of the same physical fields exist. This problem is dominant in the deep infrared. However, we will study a medium with typical temperature scales well above the energy scale where this ambiguity becomes important. We can therefore safely neglect the Gribov problem in this work.

Having fixed the gauge in our Lagrangian we have to introduce a renormalisation scheme before we can use the final Lagrangian. To this end we use a multiplicative renormalisation scheme, where

$$\begin{aligned}
\bar{\psi}\psi &\to Z_2\bar{\psi}\psi, & M &\to Z_m M, & g &\to Z_g g, \\
A_\mu &\to \sqrt{Z_3}A_\mu, & \bar{c}c &\to \tilde{Z}_3\bar{c}c, & (\xi &\to Z_\xi\xi),
\end{aligned} \qquad (2.7)$$

with the renormalisation constants Z_2, Z_m, Z_g, Z_3, $\tilde{Z}_3$ and possible Z_ξ. In Landau gauge Z_ξ is not needed. From these factors one can find the vertex renormalisation constants

$$Z_{1F} = Z_g Z_2\sqrt{Z_3}, \qquad\qquad Z_1 = Z_g\sqrt{Z_3}^3, \qquad (2.8)$$

$$\tilde{Z}_1 = Z_g\tilde{Z}_3\sqrt{Z_3}, \qquad\qquad Z_4 = Z_g^2 Z_3^2, \qquad (2.9)$$

for the quark-gluon, three-gluon, ghost-gluon and four-gluon vertices. The renormalisation constants depend on the cutoff Λ and the renormalisation point ζ. They are used to trade the Λ-dependence of a fundamentally divergent diagram for a ζ-dependence.

2.1.1 Chiral symmetry

One important symmetry of the QCD Lagrangian is chiral symmetry. This symmetry and its breaking give rise to the hadron spectrum, and to the very existence of a phase transition of QCD with light quarks.

Let us consider QCD for N_f massless quarks. With $q = (u, d, s, \dots)^T$ the quark part of the Lagrangian 2.1 separates into parts for the left and right handed fields:

$$\bar{q}\left(-\not{D}\right)q = \bar{q}_L\left(-\not{D}\right)q_L + \bar{q}_R\left(-\not{D}\right)q_R, \qquad (2.10)$$

where $q_L = \frac{1-\gamma^5}{2}q$ and $q_R = \frac{1+\gamma^5}{2}q$. We can now rotate the left and right handed fields separately in flavour space:

$$q_L \to V_L q_L, \quad q_R \to V_R q_R, \tag{2.11}$$

with $V_{L,R} \in U(N_f)$. That means we have a $U_L(N_f) \times U_R(N_f)$ symmetry on the level of the Lagrangian. This symmetry group can be decomposed as $SU_V(N_f) \times SU_A(N_f) \times U_V(1) \times U_A(1)$, where V and A denote vector and axial-vector, respectively. The $SU_V(N_f)$ group describes isospin symmetry and is conserved even on a quantum level, while the $SU_A(N_f)$ group is broken by dynamical mass generation. This effect will play a prominent role in this thesis. The $U_V(1)$ symmetry is associated with baryon number conservation, which is an exact symmetry on the quantum level as well. In contrast to that, the $U_A(1)$ is broken by the anomaly term.

When we add a mass matrix $M = \text{diag}(m_u, m_d, m_s, \dots)$ to the Lagrangian we note that

$$\bar{q}\left(-\slashed{D} + M\right)q = \bar{q}_L\left(-\slashed{D}\right)q_L + \bar{q}_R\left(-\slashed{D}\right)q_R + \bar{q}_L M q_R + \bar{q}_R M q_L, \tag{2.12}$$

i.e. the left- and right-handed fields mix. This breaks the $U_L(N_f) \times U_R(N_f)$ symmetry in the following way. The $U_V(1)$ and for $m_u = m_d = m_s = \dots$ also the $SU_V(N_f)$ symmetries are preserved, while the $SU_A(N_f)$ and $U_A(1)$ are broken explicitly by the quark mass, additionally to their breaking due to quantum effects.

The up and down quarks have a bare mass of about $m_{u/d} = 2-6$ MeV, which is much smaller than the scale of QCD, $\Lambda_{QCD} = \mathcal{O}(1\text{GeV})$. This gives rise to an approximate $SU(2)$ chiral symmetry on the classical level, which is broken dynamically. The pseudo-Goldstone bosons that correspond to the generators of the broken symmetry are the three pions. The strange quark has a bare mass of $m_s = \mathcal{O}(100\text{MeV})$. If one considers m_s as light, the chiral symmetry group is $SU(3)$, with the additional pseudo-Goldstone bosons being the four kaons and the eta meson. The η' is a special meson, since it is a would-be pseudo-Goldstone boson. However, the $U_A(1)$ anomaly gives a mass to the η' even for $m_u = m_d = m_s = 0$.

At finite temperature and/or finite baryon density, it is long established that dynamical mass generation is lost above some (pseudo-)critical temperature/density, and the chiral $SU_A(N_f)$ is approximately restored. It is not settled yet whether or not the $U_A(1)$ symmetry is restored as well, *i.e.* if the anomaly term vanishes. A restoration of this symmetry would have implications for the order of the phase transition for two massless quarks, see [50].

2.2 Functional relations

From the generating functional of correlation functions $Z[J]$, with J being a short-hand notation for all source terms, we can define the Schwinger functional

$$W[J] = \ln(Z[J]), \tag{2.13}$$

which generates connected correlation functions. The effective action is defined as the Legendre transform of W with respect to the sources

$$\Gamma[\Phi] = \sup_{J} \left(-W[J] + J\Phi \right), \tag{2.14}$$

and depends on the classical fields $\Phi = \langle \varphi \rangle$. Here φ is a short-hand notation for all fields, $\varphi = (\psi, \bar{\psi}, A_\mu, c, \bar{c})$. The effective action generates one-particle irreducible (1PI) correlation functions. This includes the propagators

$$D_{ij}^{-1}(x, y) = \left. \frac{\delta^2 \Gamma[\Phi]}{\delta \Phi_i(x) \delta \Phi_j(y)} \right|_{J=0}, \tag{2.15}$$

where the sources are set to zero. For the derivation of higher correlation functions, we will also need the propagators D^J, where the sources are not set to zero.

2.3 Dyson-Schwinger equations

In this work we will employ the Dyson-Schwinger equations for the quark and gluon propagators in order to describe the thermal properties of QCD. Here we show their derivation in the vacuum. In the medium the derivation is formally equal. We can thus discuss the changes necessary for the introduction of finite temperature and density later.

The key idea from which all DSEs are derived is that when a functional derivative is added in the generating functional, Eq. (2.2) for QCD, the integral over the fields vanishes:

$$\int \mathcal{D}\varphi \frac{\delta}{\delta \varphi} e^{-S + \int J\varphi} = 0, \tag{2.16}$$

which is owed to Gauss' theorem. Here $S = \int d^4x \mathcal{L}$ is the action of our theory. From Eq. (2.16) we can derive (see for example [51]) the master Dyson-Schwinger equation

$$\frac{\delta \Gamma}{\delta \Phi} = \left. \frac{\delta S}{\delta \varphi} \right|_{\varphi \to \Phi + D^J \frac{\delta}{\delta \Phi}}, \tag{2.17}$$

with the propagator D^J that still depends on the sources. Now if we apply n more derivatives on Eq. (2.17) and set, in the final step, the sources J to zero, we arrive at the DSE for the $n + 1$-point function. All of these equations depend on at least $n + 2$-point functions. Thus we are dealing with an infinite tower of equations that define the theory at hand in an exact way. This, most notably, constitutes a non-perturbative description of a QFT. As such, the DSEs are capable of describing phenomena like dynamical chiral symmetry breaking and confinement, which shall be the exploited in this thesis.
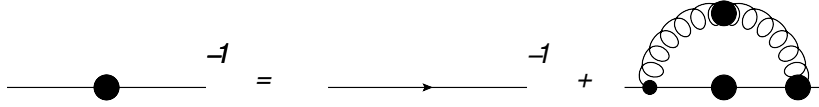
Figure 2.1: The quark DSE. The lines with and without the blob are the full and bare quark propagators. The curly line is the (fully dressed) gluon propagator, and the right vertex with the big blob is the fully dressed quark-gluon vertex.

Most important for the following is the DSE for the quark propagator. This propagator is defined by

$$S^{-1}(x, y) := \left. \frac{\delta^2 \Gamma}{\delta \Psi(x) \bar{\Psi}(y)} \right|_{J=0}, \tag{2.18}$$

for which the DSE can be derived by using Eq. (2.17). For the vacuum theory in momentum space the result is

$$S^{-1}(p) = Z_2 S_0^{-1}(p) + Z_{1F} C_F \int \frac{d^4 l}{(2\pi)^4} g \gamma_\nu S(l) g \Gamma_\mu(l, p; q) D_{\mu\nu}(q), \tag{2.19}$$

where $C_F = \frac{N_c^2 - 1}{2N_c}$ is the Casimir operator, stemming from the colour trace. We have the bare propagator $S_0^{-1}(p) = \mathrm{i} \not{p} + m$, the fully dressed quark-gluon vertex Γ_μ and the full gluon propagator $D_{\mu\nu}$. These correlation functions satisfy their own DSEs. For practical purposes this necessitates the application of a truncation scheme. In vacuum, the quark propagator S can be decomposed as

$$S^{-1}(p) = \mathrm{i} \not{p} A(p^2) + B(p^2), \tag{2.20}$$

with the vector and scalar dressing functions A and B. Sometimes one defines the wave function renormalisation $Z = 1/A$ and the mass function $M = B/A$. The dressing functions are obtained from a self-consistent solution of Eq. (2.19).

2.4 Bound states in the Bethe-Salpeter framework

The Dyson-Schwinger framework is regularly used for studying bound states. This can be done by referring to Bethe-Salpeter equations (BSEs) for two-body problems, and the Fadeev equation for three-body problems, see e.g. [52]. Although studying Bethe-Salpeter equations at finite temperature is outside the scope of this thesis, we will use some concepts and results of the Bethe-Salpeter framework. One reason for this is that contact to physical input in a confining theory can only be made via bound states. Secondly we will use a model of the pion back-reaction in chapter 9. For these reasons we now introduce the Bethe-Salpeter framework.
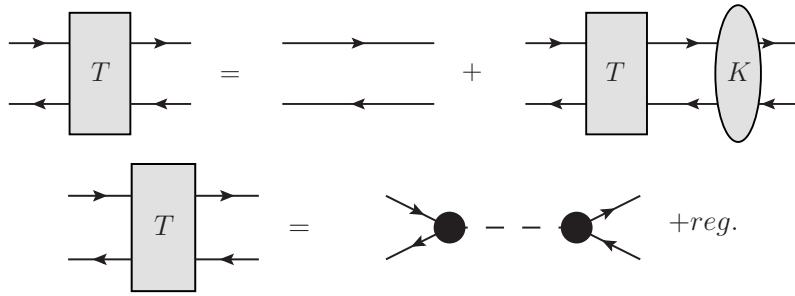
Figure 2.2: The rectangle represents the two-body propagator, while the elliptical blob represents the 2PI scattering kernel.

The inhomogeneous Bethe-Salpeter equation describes the quark-antiquark two-body propagator T in terms of the scattering kernel K. This equation is shown diagrammatically in the upper part of Fig. (2.2).

We now assume a bound-state pole of the two-body propagator in the total momentum P, see the lower part of Fig. (2.2). Thus

$$T = reg. + \bar{\Gamma}\frac{N}{P^2 + M^2}\Gamma, \tag{2.21}$$

where Γ is the quark-meson vertex (Bethe-Salpeter amplitude), N is some normalisation constant, M the mass and P the momentum of the bound state. When we put this form into the inhomogeneous BSE, we can project onto the bound state. This yields the homogeneous BSE, which describes an on-shell meson.

Figure 2.3: The homogeneous Bethe-Salpeter equation in its full (left) and ladder-truncated (right) form.

In the untruncated form, we show the homogeneous BSE in the left part of Fig. (2.3). It translates to

$$\Gamma_{tu}(p, P) = \int \frac{d^4l}{(2\pi)^4} K_{tu,rs}(p, l, P) \left[S(l_+)\Gamma(l, P)S(l_-)\right]_{rs}, \tag{2.22}$$

and describes the coupling of a bound state, such as a pion, with quarks (Γ) in terms of the quark-antiquark interaction kernel (K). This interaction is tightly linked to the self-energy of the quarks via the axial-vector Ward-Takahashi identity (AxWTI). The AxWTI is given by

$$-iP_\mu\Gamma_{5\mu}(p, P) = S^{-1}(p_+)\gamma_5 + \gamma_5 S^{-1}(p_-) - 2m\Gamma(p, P), \tag{2.23}$$

where $\Gamma_{5\mu}$ is the axial-vector vertex and $p_\pm = P \pm p/2$. This can be put in a form where the connection between the quark self-energy Σ and the interaction kernel K, becomes apparent:

$$(\Sigma(p_+)\gamma_5 + \gamma_5\Sigma(p_-))_{tu} = \int \frac{d^4l}{(2\pi)^4} K_{tu,rs}(p,l,P) \left(S(p_+)\gamma_5 + \gamma_5 S(p_-)\right)_{rs}. \qquad (2.24)$$

This tells us that when we have specified the self-energy of the quark by choosing a truncation, the kernel K has to take a specific form in order to comply with chiral symmetry. A truncation that is often used in the quark DSE is the rainbow approximation. In this scheme, the quark-gluon vertex does not depend on the quark propagator, in contrast to the Ball-Chiu construction that we will use later. Then, a kernel that solves Eq. (2.24) is given by the ladder approximation, see the right part of Fig. (2.3).

The Bethe-Salpeter amplitude (BSA) for the pion can (in vacuum) be decomposed as

$$\Gamma^i_\pi(p,P) = \tau^i\gamma_5 \left[E(p,P) - i\slashed{P}F(p,P) - i\slashed{p}\, p \cdot P G(p,P) + [\slashed{p},\slashed{P}]H(p,P) \right], \qquad (2.25)$$

with the four scalar dressing functions E, F, G, H and the Pauli matrices τ^i which describe the flavour content of the pion. The amplitude depends on the relative quark momentum p and the total momentum P, which is on-shell. If we choose the pion rest frame as our frame of reference, then $P = (0,0,0,iM_\pi)^T$.
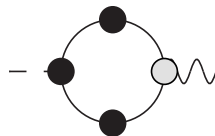
Figure 2.4: The pion couples to axial-vector and pseudo-scalar currents. These are represented by the wiggly line on the right with a vertex denoted by the grey blob.

The amplitude needs to be normalised, either by the procedure described in [53,54] or the equivalent one in [55]. With the normalised amplitude, it is possible to calculate the axial-vector and pseudo-scalar residues for the pion, f_π and r_π. It can be shown that f_π is the pion decay constant, which is defined as

$$\langle 0 | J^a_{5,\mu} | \pi^b(P) \rangle = if_\pi \delta^{ab} P_\mu, \qquad (2.26)$$

where an axial-vector current J_5 couples to a pion. In vacuum, our normalisation is such that $f_\pi \approx 93$ MeV. The pseudo-scalar residue r_π is proportional to the quark condensate in the chiral limit. [56] The coupling of the pion to axial-vector/pseudo-scalar currents is shown diagrammatically, in Fig. 2.4. The corresponding equations

read

$$f_\pi P_\mu = 3Z_2 \int \frac{d^4l}{(2\pi)^4} \text{Tr}\left[\Gamma(l,P)S(l_+)\gamma_5 P_\mu S(l_-)\right], \tag{2.27}$$

$$r_\pi = 3Z_2 \int \frac{d^4l}{(2\pi)^4} \text{Tr}\left[\Gamma(l,P)S(l_+)\gamma_5 S(l_-)\right]. \tag{2.28}$$

From these constants one can, by referring to the AxWTI, find the generalised Gell–Mann-Oakes-Renner relation

$$f_\pi M_\pi^2 = 2mr_\pi, \tag{2.29}$$

with the renormalised bare quark mass m. [56]

The pion is the Goldstone boson of dynamical chiral symmetry breaking, and as such tightly connected to the chiral dynamics in the quark sector. This can be used to solve the BSE analytically in the chiral limit, by invoking the AxWTI. The result is

$$\Gamma_\pi^i(p,0) = \tau^i \gamma_5 \frac{B(p)}{f_\pi}, \tag{2.30}$$

with $M_\pi = 0$. This relation can now be used to obtain f_π, by plugging Eq. (2.30) into Eq. (2.27). The result is the Pagels-Stokar formula [57]:

$$f_\pi^2 \approx 12Z_2 \int \frac{d^4l}{(2\pi)^4} \frac{B(l^2)A(l^2)}{(l^2A^2(l^2)+B^2(l^2))^2}\left(B(l^2) - A(l^2)\frac{l^2}{2}\frac{dM(l^2)}{dl^2}\right), \tag{2.31}$$

where $M = B/A$. This is nevertheless only an approximation. The BSA dressing functions F, G and H come with a factor P, which is set to zero. They contribute to the final expression nonetheless, since the factor is balanced by the factor P on the left-hand side of Eq. (2.27), such that not only E contributes to f_π, even in the chiral limit. However, it is a good approximation, even at small pion masses.

In a similar way we can obtain r_π from

$$r_\pi \approx 12Z_2 \int \frac{d^4l}{(2\pi)^4} \frac{1}{l^2A^2(l^2)+B^2(l^2)}\frac{B(l^2)}{f_\pi}, \tag{2.32}$$

where the F, G and H functions do not contribute. This allows us to approximate the pion mass by using Eq. (2.29) for a small quark mass m. In chapter 7 we will use this procedure to fix one vertex parameter and the quark mass to the pion decay constant and mass. We will then generalise these formulas to finite temperature in chapter 9, when we study the back-reaction of pions on the quark propagator.

2.5 Finite temperature and density

From now on we will consider QCD at finite temperature T and density n, or equivalently chemical potential μ. Since we already introduced QCD in a Euclidean space-time

in the last section, it is particularly easy to go to finite temperature. We have to constrain the time direction to a finite interval $\tau \in [0, \beta]$, where $\beta = 1/T$, and apply appropriate boundary conditions for the bosonic and fermionic fields. The QCD action changes according to

$$S = \int\limits_{-\infty}^{\infty} d\tau \int d^3x \, \mathcal{L}_{QCD} \rightarrow S = \int\limits_{0}^{\beta} d\tau \int d^3x \, \mathcal{L}_{QCD}. \tag{2.33}$$

For fermionic fields the boundary condition $\psi(\vec{x}, \tau) = -\psi(\vec{x}, \tau + \beta)$, for bosonic fields $\phi(\vec{x}, \tau) = +\phi(\vec{x}, \tau + \beta)$ is applied.

We introduce the net density $n = \int d^4x \psi^\dagger \psi$, which counts the difference of quarks and antiquarks of one flavour per volume, by adding the chemical potential μ as a Lagrange multiplier. For one flavour, this modifies the generating functional

$$\int \mathcal{D}\varphi \exp\left(-S + \int J\varphi\right) \rightarrow \int \mathcal{D}\varphi \exp\left(-S + \mu n + \int J\varphi\right). \tag{2.34}$$

Since $\psi^\dagger = \bar{\psi}\gamma_4$, we can move the $n\mu$ term to the quarks' kinetic part of the Lagrangian

$$\int d^4x \left[\bar{\psi}(-\slashed{\partial} + m)\psi\right] + n\mu = \int d^4x \left[\bar{\psi}(-\vec{\gamma}\vec{\partial} - \gamma_4(\partial_4 - \mu) + m)\psi\right], \tag{2.35}$$

and therefore the effect of the chemical potential is nothing but a modification of the bare quark propagator. We thus find for the in-medium bare propagator in momentum space

$$S_0(p) = \frac{1}{i\gamma_4(\omega_p + i\mu) + i\vec{\gamma}\vec{p} + m}, \tag{2.36}$$

with the Matsubara mode $\omega_p = \pi T(2n_p + 1)$, $n_p \in \mathbb{Z}$. We will use the short-hand notation $\tilde{\omega}_p = \omega_p + i\mu$ for the fermionic Matsubara modes with chemical potential μ.

2.5.1 Fully dressed quark propagator in the medium

The full in-medium quark propagator can be decomposed with four dressing functions as

$$S^{-1}(p) = i\vec{p}\vec{\gamma}A(p) + i\tilde{\omega}_p\gamma_4 C(p) + B(p) + i\vec{p}\vec{\gamma}\,\tilde{\omega}_p\gamma_4 D(p), \tag{2.37}$$

where the dressing functions depend on $\vec{p}^2$ and ω_p only, *e.g.* $A(p) = A(\vec{p}^2, \omega_p)$. The functions A and C are the generalisation of the inverse wave function renormalisation in vacuum, $A_{vac.} = Z^{-1}$, to finite temperature. The scalar dressing function B plays the role of a momentum-dependent mass, *i.e.* $B \neq 0$ signals chiral symmetry breaking, either by an explicit quark mass or by dynamical mass generation. We have introduced the fourth dressing function D here, which is not to be confused with the gluon propagator $D_{\mu\nu}$. The D function signals breaking the of chiral symmetry just like the B function, since

$$[\vec{p}\vec{\gamma}\,\tilde{\omega}_p\gamma_4, \gamma_5] = 0. \tag{2.38}$$

Usually, D is neglected. This is well justified, since D is small in a number of limits. Firstly, $D \equiv 0$ in the vacuum ($T = \mu = 0$), but it also vanishes at large temperatures/densities when chiral symmetry is restored. Secondly, in the UV, D is power-law suppressed since it does not have a perturbative expression. Finally, one can show that in the rainbow-ladder truncation $D \equiv 0$ because the vertex is proportional to γ_μ. Only when $\vec{\gamma}$ and γ_4 are dressed differently, D can acquire a non-zero value. Additionally we performed an explicit numerical evaluation and confirmed our expectation that D does not contribute significantly to any observable. To conclude, D is found to be unimportant and will be neglected throughout this work, and we use the propagator

$$S^{-1}(p) = \mathrm{i}\vec{p}\vec{\gamma}A(p) + \mathrm{i}\tilde{\omega}_p\gamma_4 C(p) + B(p). \tag{2.39}$$

The dressing functions at finite μ are complex, with vanishing imaginary part only at $\mu = 0$. The physical interpretation for this is the asymmetry of quarks and antiquarks in a medium with a non-vanishing net quark density. They behave like

$$A(\vec{p}^2, -\omega_p) = A^*(\vec{p}^2, \omega_p), \tag{2.40}$$

where * denotes complex conjugation. The same applies for B, C, D, which renders many Matsubara sums involving the quark propagator real.

2.5.2 Fully dressed gluon and ghost propagators in the medium

In the medium, the gluon propagator can be written as

$$D_{\mu\nu}(p) = P_{\mu\nu}^L(p)\frac{Z^L(\vec{p}^2, \omega_p)}{p^2} + P_{\mu\nu}^T(p)\frac{Z^T(\vec{p}^2, \omega_p)}{p^2}, \tag{2.41}$$

where the projectors $P_{\mu\nu}^L(p)$ and $P_{\mu\nu}^T(p)$ project onto the components longitudinal and transversal to the heat bath:

$$P_{\mu\nu}^T(p) = (1 - \delta_{\mu 4})(1 - \delta_{\nu 4})\left(\delta_{\mu\nu} - \frac{p_\mu p_\nu}{\vec{p}^2}\right), \tag{2.42}$$

$$P_{\mu\nu}^L(p) = P_{\mu\nu}(p) - P_{\mu\nu}^T(p), \tag{2.43}$$

$$P_{\mu\nu}(p) = \delta_{\mu\nu} - \frac{p_\mu p_\nu}{p^2}, \tag{2.44}$$

where $P_{\mu\nu}$ projects transversal to the gluon momentum. The gluon is a boson and thus $\omega_p = 2\pi T n_p$, corresponding to periodic boundary conditions.

Being scalar, the ghost does not receive additional structure at finite temperature and can be defined as

$$D_G(p) = -\frac{G(\vec{p}^2, \omega_p)}{p^2}, \tag{2.45}$$

where again $\omega_p = 2\pi T n_p$ corresponds to a particle with periodic boundary conditions.

2.5.3 Dyson-Schwinger equations in the medium

We will obtain the propagators S and $D_{\mu\nu}$ in the medium from their Dyson-Schwinger equations. At finite T and μ, the derivation and formal structure of the DSEs is the same as in the vacuum, which we outlined in section 2.3. To summarise the discussion above, we have to apply three changes when we go to the medium.

1. The integral over momentum space now involves a sum over Matsubara modes

$$\int \frac{d^4 p}{(2\pi)^4} \to T \sum_n \int \frac{d^3 p}{(2\pi)^3} =: \sum_p \!\!\!\!\!\! \int, \qquad (2.46)$$

   where $p_4 \to \omega_p$ with $\omega_p = 2\pi T n_p$ for bosons and $\omega_p = \pi T (2n_p + 1)$ for fermions. We will often use the short-hand notation on the right hand side of Eq. (2.46).

2. The bare quark propagator includes the chemical potential according to Eq. (2.36). We introduce

$$\tilde{\omega}_p = \omega_p + i\mu, \qquad (2.47)$$

   for quarks as a short-hand notation.

3. The four-velocity u_μ of the medium introduces an additional vector that has to be taken into account when decomposing fully dressed Green's functions. This also entails that the dressing functions in general depend on more variables, e.g. p^2 and $u \cdot p$ instead of only p^2. Alternatively, we can choose to take $(u_\mu) = (0, 0, 0, 1)^T$, *i.e.* take the reference frame of the medium, and therefore give up explicit Lorentz invariance. This is what we have done above, and means that the propagators' dressing functions depend on $\vec{p}^2$ and ω_p separately.

Following these changes, the quark DSE, which we introduced in Eq. (2.19) for the vacuum, becomes

$$S^{-1}(p) = Z_2 S_0^{-1}(p) + Z_{1F} C_F T \sum_n \int \frac{d^3 l}{(2\pi)^3} g\gamma_\nu S(l) g\Gamma_\mu(l, p; q) D_{\mu\nu}(q), \qquad (2.48)$$

in the medium. In order to solve the DSE we need to specify the full quark-gluon vertex Γ_μ and the gluon propagator $D_{\mu\nu}$ at finite temperature and chemical potential. Then, with the decomposition Eq. (2.39), we project the DSE on the dressing functions A, B and C by using the projectors

$$P_A = \frac{\vec{p}\vec{\gamma}}{4i\vec{p}^2}, \qquad P_B = \frac{1}{4}, \qquad P_C = \frac{\gamma_4}{4i\tilde{\omega}_p}, \qquad (2.49)$$

and taking the trace in Dirac space. The resulting coupled equations for A, B and C will then be solved self-consistently.

3 Order parameters for chiral symmetry and confinement from propagators

In this work we will solve the Dyson-Schwinger equations for the quark and gluon propagators in a truncation to be defined below. The goal is to study the chiral and deconfinement transitions. In this chapter we will make the connection between the propagators and order parameters that describe these transitions.

3.1 Chiral symmetry: the quark condensate

From a solution of the quark DSE, a non-vanishing B function directly tells us that chiral symmetry is broken. Since we want to study QCD with physical quark masses, B is always non-zero, and there is strictly speaking no chiral phase transition. However, at large temperature/density chiral symmetry is approximately restored and B becomes small compared to its value in vacuum.

There are several equivalent order parameters for the approximate restoration of chiral symmetry, for instance $B(0)$, the pion decay constant or the commonly used quark condensate. We will use the latter here, since it is a gauge-independent quantity that can also be measured in lattice QCD.

From the quark propagator, Eq. (2.39), one can obtain the condensate[1]

$$\langle \bar{\psi}\psi \rangle = N_c Z_2 Z_m T \sum_n \int \frac{d^3 l}{(2\pi)^3} \mathrm{Tr}_D \left[S(l) \right], \tag{3.1}$$

where Tr_D is the trace in Dirac space. We find

$$\langle \bar{\psi}\psi \rangle = 4 N_c Z_2 Z_m T \sum_n \int \frac{d^3 l}{(2\pi)^3} \frac{B(l)}{C^2(l)\tilde{\omega}_l^2 + A^2(l)\vec{l}^2 + B^2(l)}, \tag{3.2}$$

and it becomes obvious that for $B = 0$ we have $\langle \bar{\psi}\psi \rangle = 0$. This leads us to the behaviour of our chiral order parameter

$$\langle \bar{\psi}\psi \rangle = \begin{cases} 0 & \text{if chiral symmetry is exact} \\ \text{non-zero} & \text{if chiral symmetry is broken.} \end{cases} \tag{3.3}$$

---

[1]We define the condensate to be positive in this work.

For finite bare quark mass m the resulting quantity diverges quadratically with cutoff Λ, it contains a term $\propto m\Lambda^2$. Since the divergence is independent of temperature and density, it can safely be ignored when the order parameter is used only to find the (pseudo-)critical temperature. We will later compare our results for the condensate to lattice data, and therefore have to remove the divergence. This can be done by using the condensates for light and strange quarks

$$\Delta_{l,s} = \langle\bar{\psi}\psi\rangle_l - \frac{m_l}{m_s}\langle\bar{\psi}\psi\rangle_s\,, \tag{3.4}$$

where the divergent part $m_s\Lambda^2$ from the strange quark condensate $\langle\bar{\psi}\psi\rangle_s$ cancels the corresponding part of the light quark condensate $\langle\bar{\psi}\psi\rangle_l$ when multiplied with the ratio m_l/m_s of light to strange quark masses.

3.2 Confinement

One of the most important properties of QCD is the phenomenon of confinement, where the theoretical understanding is still incomplete. See for example [58] for a discussion of confinement in lattice QCD. There exist several confinement scenarios, which are mainly concerned with the absence of free coloured particles (colour confinement) or a linear rising potential between heavy quarks (quark confinement). In the first class falls the Kugo-Ojima scenario [59, 60]. There, it can be shown that the colour charge of a physical state vanishes, if the ghost dressing function is singular for $p^2 \to 0$ and under a few more conditions. On the other hand, there is quark confinement. When we look at the potential between an infinitely heavy quark and antiquark, we find a form

$$V(r) = \frac{\alpha}{r} + \sigma r, \tag{3.5}$$

where we have a linear component σr. This means that the energy needed to separate a quark-antiquark pair rises to infinity with the distance, which is a widely used notion of confinement. However, in QCD with physical quark masses, the energy will eventually be large enough for a quark-antiquark pair to be created, which is denoted as string breaking [61]. The potential will therefore flatten above a certain distance. In this sense, QCD with physical quarks is not confining. However, this does not mean that coloured particles could be found in an experiment, since the string breaking always happens in such a way that the asymptotic particles are colour-neutral.

3.2.1 Centre symmetry and the Polyakov loop

The Polyakov loop is an order parameter related to the linear rising potential, and thus is most often used to study the confinement/deconfinement phase transition. It is derived from the Wilson loop in time direction

$$P(\vec{x}) = \mathcal{P}e^{\mathrm{i}g\int_0^\beta d\tau A_4(\vec{x},\tau)}, \tag{3.6}$$

where $\mathcal{P}$ denotes the path-ordered product. From this we obtain the Polyakov loop $L(\vec{x})$ by taking

$$L(\vec{x}) = \frac{1}{N_c} \text{Tr} P(\vec{x}), \tag{3.7}$$

and its expectation value

$$\Phi = \langle L(\vec{x}) \rangle. \tag{3.8}$$

It can now be shown that Φ is related to the free energy of a static quark, see e.g. [62]. One finds

$$\Phi \propto e^{-F_q/T}, \tag{3.9}$$

and thus

$$\Phi = \begin{cases} 0 & \text{if } F_q = \infty \\ \text{non-zero} & \text{if } F_q < \infty. \end{cases} \tag{3.10}$$

If $F_q = \infty$, a free quark can not be produced and we are in that sense in the confined phase. We therefore found the order parameter Φ, which is 0 in the confined phase, and non-zero otherwise.

The Polyakov loop turns out to be sensitive to centre symmetry. The centre of an $SU(N_c)$ group is $\mathbb{Z}_{N_c}$, containing the Nth roots of unity, where the elements are

$$z_n = e^{2\pi i n/N_c} \in SU(N_c), \tag{3.11}$$

with $n \in 0, \ldots, N_c - 1$. To show the relation to centre symmetry, it is advantageous to go to a lattice formulation. There, the gauge fields are described by the link variables $U_\mu(\vec{x}, \tau)$. The Polyakov loop is then obtained from

$$L(\vec{x}) = \frac{1}{N_c} \text{Tr} \left[\Pi_i \, U_4(\vec{x}, \tau_i) \right], \tag{3.12}$$

such that we have a product of links along the time direction. A centre transformation can now be performed by

$$U_4(\vec{x}, \tau_j) \rightarrow z U_4(\vec{x}, \tau_j), \tag{3.13}$$

for one time slice τ_j and a centre element z. It is then owed to the commutativity of the centre that we find

$$L(\vec{x}) \rightarrow z L(\vec{x}). \tag{3.14}$$

Thus we have a broken centre symmetry[2] if $\Phi \neq 0$, where the theory picks one direction of the centre group spontaneously. In the symmetric phase we find $\Phi = 0$. The breaking of centre symmetry is therefore equivalent to a finite F_q, and thus signals deconfinement.

When dynamical quarks are taken into account, centre symmetry is broken explicitly. We therefore always find $\Phi \neq 0$ in unquenched QCD, and can only define a pseudo-critical temperature for a crossover transition. This might change when the full centre

---

[2]Centre symmetry is a global symmetry, its breaking does therefore not violate the Elitzur theorem [63].

symmetry Z_6 of the standard model is taken into account, see [64]. If that is the case, the fractional charges of the quarks have a natural role in the description of confinement, which they lack in the pure QCD treatment.

The connection between centre symmetry and confinement allows us to construct an order parameter for the latter by requiring it to be sensitive to a centre transformation. We will exploit this by using the dressed Polyakov loop, which is more readily obtained from the propagators of QCD than the Polyakov loop itself.

3.2.2 The dressed Polyakov loop

The idea of dual condensates has been introduced in [65–67]. We now shortly summarise how this is connected to the Polyakov loop, which we discussed above.

The key observation is the following. We allow the quarks to not be anti-periodic in Euclidean time. Instead, we let them adhere to generalised $U(1)$-valued boundary conditions, such that $\psi(\vec{x}, 1/T) = e^{i\varphi}\psi(\vec{x}, 0)$ with $\varphi \in [0, 2\pi[$. Physical boundary conditions are the special case of $\varphi = \pi$. In a lattice formulation one can write the φ-dependent condensate as (see [41, 67])

$$\langle\bar{\psi}\psi\rangle_\varphi = \sum_{l \in \mathcal{L}} \frac{e^{i\varphi n(l)}}{(2am)^{|l|}} U(l), \qquad (3.15)$$

where we sum over loops l of gauge connections in the set $\mathcal{L}$ of all closed loops. The lattice spacing is a, $|l|$ is the length of such a loop, and $n(l)$ counts how many times it winds around the Euclidean-time direction. As an abbreviation we define

$$U(l) \propto \langle\mathrm{Tr}_c\Pi_l U_\mu(x)\rangle, \qquad (3.16)$$

which is proportional to an expectation value of a product of gauge connections. Since we sum over all closed loops, this includes a straight line going once around the Euclidean time direction, $\langle\mathrm{Tr}_c\Pi_i U_4(\vec{x}, \tau_i)\rangle$. This is nothing but the Polyakov loop, Eq. (3.12). Thus the Polyakov loop is "hidden" in the quark condensate. Extracting this particular loop consists of two steps. First we take the Fourier transform of Eq. (3.15) with respect to the boundary angle φ, from which we obtain the dual condensate

$$\Sigma_n = \int_0^{2\pi} \frac{d\varphi}{2\pi} e^{-i\varphi n} \langle\bar{\psi}\psi\rangle_\varphi. \qquad (3.17)$$

This contains only such loops that wind n times around the time direction. For $n = \pm 1$ this includes the Polyakov loop, but also spatial detours. For this reason the dual condensate Σ_{+1} is called the dressed Polyakov loop. In contrast, the standard definition of the Polyakov loop is sometimes called the "thin" Polyakov loop. In a medium with finite net quark density the dual condensate Σ_{-1} corresponds to the conjugated dressed Polyakov loop and is in general different from Σ_{+1}. The second step is to take the limit

$m \to \infty$. Since loops are suppressed with $1/m^{|l|}$, see Eq. (3.15), the Polyakov loop is the leading contribution in this limit. Note that this second step is not necessary for Σ_n to be an order parameter for centre symmetry breaking. As it has been shown in [67], it transforms under centre transformations like

$$\Sigma_n \to z^n \Sigma_n, \tag{3.18}$$

for a centre element z. Loops that are not straight have to pick up a factor $z^\dagger$ for every extra factor z they pick up, thus leaving an over-all factor z^n.

Since the necessary input for obtaining the dressed Polyakov loop is the quark condensate at varied boundary conditions, we can access this order parameter for confinement from functional methods. This has first been done in [40] for quenched QCD.

For unquenched QCD there are two possibilities to implement the boundary conditions. If we implement them equally for the test quark in Eq. (3.17) and the sea quarks, we can identify

$$\varphi = \mu_I/T \pm \pi, \tag{3.19}$$

where μ_I is an imaginary chemical potential. This situation has been studied in the PNJL model in [68]. The disadvantage of this is that we want to study a real chemical potential. This would result in a complex chemical potential, and thus a theory where every object becomes complex. The physical interpretation of this is unclear.

The other possibility is to employ sea quarks at the usual anti-periodic boundary conditions $\varphi = \pi$. This is implemented by using for the φ-dependent condensate in Eq. (3.17) the definition

$$\langle \bar{\psi}\psi \rangle_\varphi = \int \mathcal{D}\psi \mathcal{D}\bar{\psi} \mathcal{D}A \left(\bar{\psi}_\varphi \psi_\varphi \right) e^{-S[\psi,\bar{\psi},A] + \int J\varphi}, \tag{3.20}$$

where ψ_φ is the φ-dependent test quark field, while ψ is the physical quark field. We neglect the ghost fields for simplicity. On the lattice this means to use a fermion determinant with $\varphi = \pi$. This has been studied in [69]. In the PNJL model, the fermionic fluctuations are subsumed in the Polyakov-loop variable. Taking this to be independent of φ leads to a similar set-up. This has been studied in [70]. We will follow this line here. In our approach this means that all quark loops are evaluated at $\varphi = \pi$. The φ-dependent condensate is then obtained from the quark DSE defined for Matsubara modes shifted by φ. Roberge-Weiss symmetry is broken by this procedure. [32, 71]

3.2.3 The Polyakov loop potential

In chapter 8 we will investigate another possibility to access the Polyakov loop from functional methods, which is based on [72–74]. We will use the background-field method to obtain a potential $V(\bar{A}_4)$. Here $\bar{A}_4$ is a constant non-Abelian background that can be connected to the Polyakov loop, Eq. (3.6). The Polyakov loop for the background

field is an upper bound for the Polyakov loop for a non-constant field. As we will see, this leads to a second way how we can construct an order parameter for centre symmetry breaking from solutions of Dyson-Schwinger equations.

3.2.4 Positivity violations

So far, we used a notion of confinement that relies on the linear rising potential between static quarks. A different confinement criterion is that of colour confinement, which is connected to the spectral functions of quarks and gluons. The Osterwalder-Schrader axioms for physical particles include the axiom of reflection positivity [75], which implies the existence of a Källén-Lehmann spectral representation of the corresponding propagator. For a propagator $\Delta(x)$ the condition of reflection positivity is

$$\int d^4x d^4y f^*(\vec{x}, -x_0)\Delta(x - y)f(\vec{y}, y_0) \geq 0, \tag{3.21}$$

where $f(x) \in \mathbb{C}$ is a test function. The positivity of the spectral function is connected to the Schwinger function, which is defined as a Fourier transformation

$$\Delta(t) = T \sum_n e^{-\mathrm{i}\omega_n \tau}\Delta(\omega_n, \vec{p} = 0) \tag{3.22}$$

of the propagator in momentum space $\Delta(\omega_n, \vec{p})$. If the Schwinger function is negative for some t, the spectral function must violate positivity as well. This was studied in [76] for gluon and quark propagators in the vacuum. Positivity violations where found for both.

In [77, 78] the quark spectral functions have been studied at finite temperature. For the quark propagator above T_c, the spectral function was fitted to HTL results with good agreement. Below T_c, positivity violations where found from the Schwinger function, with no sign of them above T_c. We will follow that line of argument in this thesis in section 7.8. In [79, 80] a maximum-entropy method (MEM) has been applied to determine the spectral function. It was found that at small temperatures the result clearly has negative contributions, which vanish at temperatures slightly smaller than the chiral critical temperature.

4 The quark-gluon vertex and the quark DSE at finite temperature

A truncation for the quark DSE consists of two parts, the gluon propagator and the quark-gluon vertex. In vacuum studies, one often uses a combination of both in the so-called rainbow truncation. In this approximation, the resulting effective coupling is chosen such that hadronic observables are reproduced. This can then be used to obtain many properties of e.g. hadrons. In this work, on the other hand, we want to study effects of the medium. This makes a careful analysis of the temperature and density dependence of the truncation necessary. To this end, we treat the gluon propagator and the quark-gluon vertex separately. We will specify the gluon propagator in the next chapters in different approximations, and now concentrate on the vertex.

4.1 The quark-gluon vertex

In the vacuum, the full quark-gluon vertex has been investigated in a number of studies from its DSE, see [81–84]. At finite temperature such a study is lacking so far. The vertex DSE is already a serious task in the vacuum, in medium it becomes even more complex. One reason is the increase of tensor structures, that are given by

$$
\begin{pmatrix} \gamma_\mu \\ k_\mu \\ q_\mu \\ u_\mu \end{pmatrix} \otimes \begin{pmatrix} \mathbb{1} \\ \slashed{k} \\ \slashed{q} \\ \slashed{k}\slashed{q} \\ \slashed{u} \\ \slashed{k}\slashed{u} \\ \slashed{q}\slashed{u} \\ \slashed{k}\slashed{q}\slashed{u} \end{pmatrix}
\tag{4.1}
$$

where u is the medium velocity. This leads to 32 tensor structures, of which 24 remain after contracting with the transversal gluon propagator. The vertex satisfies the non-Abelian Slavnov-Taylor identity (STI) which has been derived in [85] for the vacuum. It is given by

$$
q_\mu \Gamma_\mu(p,k;q) = G(q) \left[H(p,k)S^{-1}(p) - S^{-1}(k)H(p,k) \right],
\tag{4.2}
$$

where G is the ghost dressing function and H is the quark-ghost scattering kernel. This identity gives us valuable insight in the full vertex. If we simplify the situation

by going to the Abelian version of the STI, the Ward identity, we find

$$q_\mu \Gamma_\mu(p, k; q) = S^{-1}(p) - S^{-1}(k). \tag{4.3}$$

A solution of this equation has been presented by Ball and Chiu. [86] We will use the leading part of the Ball-Chiu vertex construction as a first approximation to the medium effects of the vertex. This is given by

$$(\Gamma_\mu(p, k; q)) = \left(\frac{A(p) + A(k)}{2} \vec{\gamma}, \frac{C(p) + C(k)}{2} \gamma_4 \right), \tag{4.4}$$

in the medium. This term alone is not sufficient to allow for dynamical chiral symmetry breaking. This is understandable, since in QCD the vertex receives further contributions from the ghost and ghost-quark scattering kernel, see Eq. (4.2). We compensate this by further dressing the vertex with an *ansatz* function Γ, which subsumes the non-Abelian contributions. In the UV this function is constrained from perturbation theory. The combination of $\Gamma^2 Z/A^2$, where Z is the gluon dressing, has to behave like the running coupling. [81] Furthermore, in the UV temperature and density effects are suppressed, and we can therefore safely use a function constant in T and μ. In the IR, however, not only is Γ unknown, we can also expect medium effects. Lacking knowledge of this function, we have to rely on a model input, which leads to a vertex strength that is sufficient to allow for dynamical chiral symmetry breaking. We will later fix the parameters in this IR part by demanding correct scales to emerge.

The resulting expression has already been used in [40, 42] and reads

$$\Gamma_\mu(p, k; q) = \gamma_\mu \cdot \Gamma(x) \cdot \left(\delta_{\mu,4} \frac{C(p) + C(k)}{2} + \delta_{\mu,i} \frac{A(p) + A(k)}{2} \right),$$

$$\Gamma(x) = \frac{d_1}{d_2 + x} + \frac{x}{\Lambda^2 + x} \left(\frac{\beta_0 \alpha(\mu) \ln[x/\Lambda^2 + 1]}{4\pi} \right)^{2\delta} \tag{4.5}$$

for quark momenta p, k and the gluon momentum q. In the upper line of Eq. (4.5) no summation over μ is implied. We used x as a place holder for a squared momentum. In the quark DSE we will use the gluon momentum, $x = q^2$. In contrast to that, in the gluon DSE we will have to use a different momentum dependence, discussed later. We introduce d_1 and the scales d_2 and Λ as parameters of our vertex model. The form of Γ is a simplified version of the so-called "soft-divergent model" introduced in [87]. Here, d_1 sets the strength of the vertex in the IR, and will be the parameter that we tune to get e.g. the expected amount of dynamical chiral symmetry breaking. The parameters d_2 and Λ control the running from the UV to the IR. For the UV part, we have the anomalous dimension $\delta = -9 \frac{N_c}{44N_c - 8N_f}$ and $\beta_0 = \frac{11N_c - 2N_f}{3}$. We will later use the abbreviations

$$\Gamma_s(p, q) = \frac{A(p) + A(q)}{2}, \quad \Gamma_4(p, q) = \frac{C(p) + C(q)}{2}, \tag{4.6}$$

for the Ball-Chiu part of the vertex.

This vertex construction has two insufficiencies. Firstly, the infrared enhancement $\frac{d_1}{d_2+x}$ in Eq. (4.5) does not depend on temperature. We expect this part to be suppressed by temperature effects, which might be expressed by making d_1 a function of T and μ. We find that an *ansatz* with $d_1 \propto 1/T$ above T_c leads to results closer to lattice QCD at $\mu = 0$. However, for now we will not introduce such a model since it can barely be generalised to include a finite chemical potential.

Secondly, the full vertex contains 12 tensor structures in the vacuum, and 24 in the medium. We only take one (two in the medium) of them into account. Especially a scalar part $\propto p_\mu$ is believed to be important for chiral symmetry breaking [84], and can thus be expected to play an important role around the phase transition where chiral symmetry is restored. However, in this work we will not take this kind of tensor structure into account, and a study of an improved vertex model will have to be explored in future work.

4.2 Solving the Dyson-Schwinger equations in a medium

In Eq. (2.48) we showed the quark DSE in the medium and defined the projectors $P_{A,B,C}$ in Eq. (2.49). With the vertex *ansatz* Eq. (4.5) we can now apply the projectors to get the equations for the quark dressing functions A, B and C. This results in

$$A(p) = Z_2 \cdot 1 \qquad + Z_2 C_F g^2 \sum\!\!\!\!\!\!\int_l \frac{\Gamma(q^2)}{D_q(l)\vec{p}^2} \left\{ A(l)K_{AA} + C(l)K_{AC} \right\}, \qquad (4.7)$$

$$B(p) = Z_2 Z_m \cdot m_r \quad + Z_2 C_F g^2 \sum\!\!\!\!\!\!\int_l \frac{\Gamma(q^2)}{D_q(l)} B(l)K_{BB}, \qquad (4.8)$$

$$C(p) = Z_2 \cdot 1 \qquad + Z_2 C_F g^2 \sum\!\!\!\!\!\!\int_l \frac{\Gamma(q^2)}{D_q(l)\tilde{\omega}_p} \left\{ A(l)K_{CA} + C(l)K_{CC} \right\}, \qquad (4.9)$$

where the gluon momentum is $(\omega_q, \vec{q}) = (\omega_p - \omega_l, \vec{p} - \vec{l})$ and we introduced some abbreviations. The quark denominator is $D_q(p) = \vec{p}^2 A^2(p) + \tilde{\omega}_p^2 C^2(p) + B^2(p)$, and the

kernels are

$$K_{AA} = \Gamma_s \left[2\frac{Z_T}{q^2}\frac{\vec{p}\cdot\vec{q}\,\vec{l}\cdot\vec{q}}{\vec{q}^2} + \frac{Z_L}{q^2}\left(\frac{\vec{p}\cdot\vec{l}\,\omega_q^2 + 2\vec{p}\cdot\vec{q}\,\vec{l}\cdot\vec{q}}{q^2} - 2\frac{\vec{p}\cdot\vec{q}\,\vec{l}\cdot\vec{q}}{\vec{q}^2} \right) \right] + \Gamma_4 \frac{Z_L}{q^2}\frac{\vec{q}^2\vec{p}\cdot\vec{l}}{q^2}, \tag{4.10}$$

$$K_{AC} = \frac{Z_L}{q^2}(\Gamma_s + \Gamma_4)\frac{\tilde{\omega}_l\omega_q\vec{p}\cdot\vec{q}}{q^2}, \tag{4.11}$$

$$K_{BB} = \Gamma_s \left(2\frac{Z_T}{q^2} + \frac{Z_L}{q^2}\frac{\omega_q^2}{q^2} \right) + \Gamma_4 \frac{Z_L}{q^2}\frac{\vec{q}^2}{q^2}, \tag{4.12}$$

$$K_{CA} = \frac{Z_L}{q^2}(\Gamma_s + \Gamma_4)\frac{\omega_q\vec{l}\cdot\vec{q}}{q^2}, \tag{4.13}$$

$$K_{CC} = \Gamma_s \left(2\frac{Z_T}{q^2}\tilde{\omega}_l + \frac{Z_L}{q^2}\frac{\tilde{\omega}_l\omega_q^2}{q^2} \right) - \Gamma_4 \frac{Z_L}{q^2}\frac{\vec{q}^2\tilde{\omega}_l}{q^2}, \tag{4.14}$$

with the vertex dressings $\Gamma_s = \frac{A(l)+A(p)}{2}$ and $\Gamma_4 = \frac{C(l)+C(p)}{2}$ from the Ball-Chiu constructions, as defined in Eq. (4.6). The momentum dependence in the vertex which was left open in Eq. (4.5) is chosen here such that Γ depends on the gluon momentum, q^2, only. This is in line with rainbow-ladder truncations.

Eqs. (4.7-4.9) will be used throughout the rest of this work, since they are the same for quenched and unquenched QCD. This only changes in Chapter 9 where we will introduce a model for the back-reaction of pions on quarks, which will add an additional self energy to the quark DSE. In order to solve Eqs. (4.7-4.9), we need to specify the gluon propagator. This will be the task for a large part of this thesis.

For the numerical solution of Eqs. (4.7-4.9), we apply a fix-point iteration procedure. Some numerical details on the solution of the quark DSE are given in App. B.1.

5 Quenched QCD

Before we continue with unquenched QCD, we will briefly study the pure Yang-Mills system, *i.e.* quenched QCD, in this chapter. This will not only serve as the basis for the unquenched gluon DSE, it is also an important cross-check for our method and our order parameters to reproduce the behaviour of quenched QCD. This is especially true for the confinement order parameters, since confinement, if defined as a linear rising potential, is strictly present only in quenched QCD. Dynamical quarks lead to string breaking, respectively centre symmetry breaking, and therefore the Polyakov loop will not be zero below T_c for $N_f > 0$. It is therefore crucial to show that an order parameter for confinement has the expected properties in the quenched case.
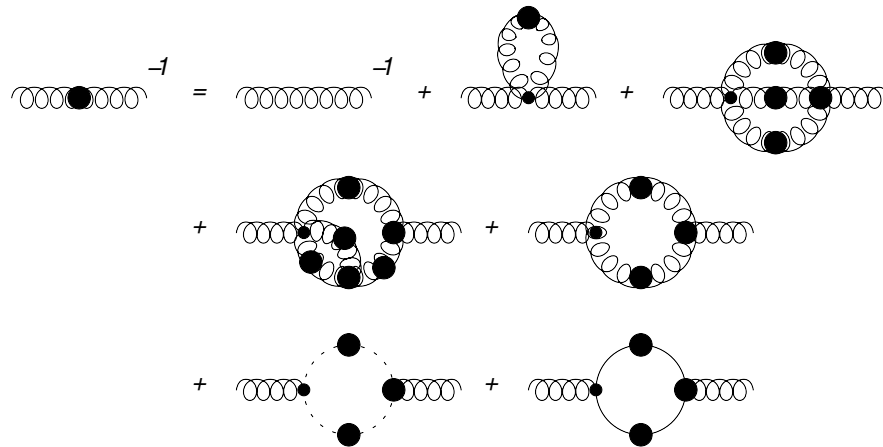
Figure 5.1: The untruncated gluon DSE. The wiggly line is the gluon propagator, the dashed line the ghost and the solid line the quark propagator. Propagators and vertices denoted by a blob are fully dressed.

Figure 5.2: The ghost DSE. The dashed line is the ghost and the wiggly line the gluon propagator. The blob denotes fully dressed propagators/vertices.

In Figs. (5.1,5.2) we show the gluon and ghost DSEs. If we neglect the quark loop, *i.e.* the last diagram in Fig. (5.1), we recover quenched QCD. A study of this set

of equations at finite temperature has been performed in [38, 39, 88, 89], and one is currently in progress [90]. The Yang-Mills system has also been studied with the functional renormalisation group (FRG) in [33].

However, all functional studies are plagued by truncation effects. These effects have so far hindered especially the resolution of the quenched phase transition. This leaves us with results from gauge-fixed lattice studies as the best source for the quenched gluon as an input in our equations. This will further be explored in this chapter, which is to a large degree a repetition of the work done in [40, 42, 91] with refined input data. In the next chapters we will use this as a starting point for unquenching QCD.

5.1 Gluon propagator from gauge-fixed lattice QCD

Gauge-fixed lattice simulations have been used to obtain the quenched gluon propagator in Landau gauge in several works. In [42, 92, 93] propagators on an improving temperature grid have been presented, and used in [40, 42, 91] as an input to the quark DSE in order to study dual condensates. We will continue this line of work here. In [94] a different group presented gluon propagators that are basically in agreement with those mentioned before.

Recalling Eq. (2.41), we can split the temperature-dependent gluon propagator into two dressing functions. These are Z_L and Z_T for the gluon longitudinal and transversal to the heat bath. In [40] an analytic function has been used as a fit of the dressing functions to the lattice data. This function had one parameter, $a_{T,L}(T)$, for each of the gluon dressing functions. The fit had been performed for a set of temperatures. In [42] the fit function has been generalised slightly by introducing a second parameter, $b_{T,L}(T)$. We will use this function here, which reads

$$Z_{T,L}(p) = \frac{\hat{p}^2}{(\hat{p}^2 + 1)^2} \left[\left(\frac{\hat{c}}{\hat{p}^2 + a_{T,L}(T)} \right)^{b_{T,L}(T)} + \hat{p}^2 \left(\frac{\beta_0 \alpha_\mu}{4\pi} \ln(\hat{p}^2 + 1) \right)^\gamma \right], \qquad (5.1)$$

where $a_{T,L}(T)$ and $b_{T,L}(T)$ are the fit parameters which depend on temperature and are different for the longitudinal and the transversal part. We use the abbreviations $\hat{p}^2 := p^2/\Lambda^2$ and $\hat{c} := c/\Lambda^2$. In the ultraviolet, the logarithmic term leads to the perturbative running with $\beta_0 = \frac{11N_c - 2N_f}{3}$ and the anomalous dimension $\gamma = \frac{-13N_c + 4N_f}{22N_c - 4N_f}$. Here, $N_f = 0$. The parameters are Λ, c, $a_{T,L}$ and $b_{T,L}$, where only the last two are taken to be temperature-dependent. The temperature-independent parameters are chosen as $c = 11.5 \text{ GeV}^2$ and $\Lambda = 1.4 \text{ GeV}$. In [42] the parameters $a_{T,L}(T)$ and $b_{T,L}(T)$ have been fitted to the lattice data at 16 temperatures. We perform a similar fit to the lattice data from [93], where the gluon propagator was calculated for 27 temperatures, where the additional data focusses around T_c. The resulting parameters are shown in App. D.

In Fig. 5.3 we show the gluon dressing functions from the lattice for three temperatures and the result of fitting Eq. (5.1) to them. The longitudinal part of the gluon shows an increasing behaviour with temperature, which stops already below T_c. At T_c
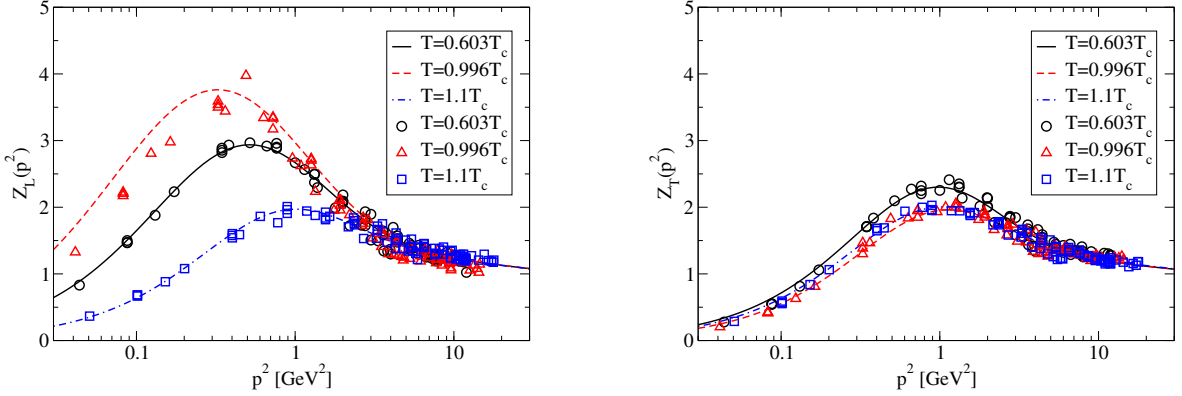
Figure 5.3: Longitudinal (left) and transversal (right) gluon dressing functions. We compare our fit to the lattice data from [93].

it shows a drastic decrease, and a further decreasing behaviour above T_c. In contrast to that, the transversal part shows little temperature dependence. It decreases and barely changes at T_c.

We will use the temperature grid on which the original gluon was obtained for our quenched calculations. However, for unquenched QCD we will have to interpolate between these data points. We do this by fitting polynomial functions to the fit results $a_{T,L}(T)$ and $b_{T,L}(T)$. The resulting functions read, for $t := T/T_c$ with $T_c = 277$ MeV, as

$$a_L(t) = \begin{cases} 0.595 - 0.9025 \cdot t + 0.4005 \cdot t^2 & \text{if } t < 1 \\ 3.6199 \cdot t - 3.4835 & \text{if } t > 1 \end{cases}, \tag{5.2}$$

$$a_T(t) = \begin{cases} 0.595 + 1.1010 \cdot t^2 & \text{if } t < 1 \\ 0.8505 \cdot t - 0.2965 & \text{if } t > 1 \end{cases}, \tag{5.3}$$

$$b_L(t) = \begin{cases} 1.355 - 0.5741 \cdot t + 0.3287 \cdot t^2 & \text{if } t < 1 \\ 0.1131 \cdot t + 0.9319 & \text{if } t > 1 \end{cases}, \tag{5.4}$$

$$b_T(t) = \begin{cases} 1.355 + 0.5548 \cdot t^2 & \text{if } t < 1 \\ 0.4296 \cdot t + 0.7103 & \text{if } t > 1 \end{cases}. \tag{5.5}$$

In Fig. 5.4 we compare the set of parameters from [42] to our polynomial fit. At $T = 2.2\, T_c$ the fits for b_L and b_T do not describe the data, but since we are mostly interested in temperatures well below the quenched T_c this will not affect our results. With this prescription our quenched gluon is fixed at all temperatures.

A note is in order here about the IR behaviour of the gluon and ghost propagators. There exist two types of solutions, a so-called scaling solution and a class of decoupling solutions, see e.g. [95]. This ambiguity is a consequence of Gribov copies, *i.e.* the incomplete gauge-fixing [96]. The dressing functions in general behave like

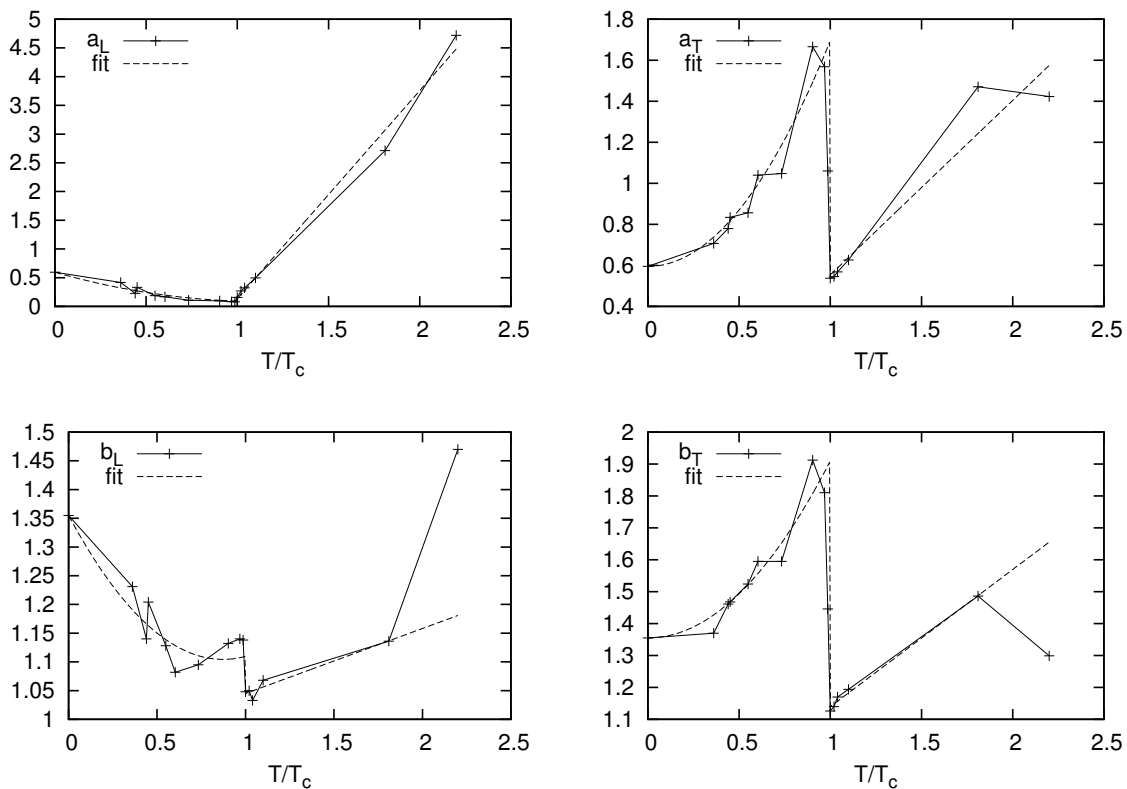$$Z(p^2) \to (p^2)^{-\kappa_A}, \qquad G(p^2) \to (p^2)^{-\kappa_C}, \tag{5.6}$$

Figure 5.4: The parameters $a_{L/T}$ and $b_{L/T}$ of the quenched gluon propagator compared to the fitted functions Eqs. (5.2-5.5).

where Z and G are the gluon and ghost dressing functions, respectively. For the scaling solution we have $\kappa = \kappa_C = -\kappa_A/2 \in [1/2, 1]$. For decoupling $\kappa_A = -1$ and $\kappa_C = 0$. In Eq. (5.1) we assumed the IR behaviour of the gluon to be in the decoupling class, since this is the favoured solution in most lattice simulations. The difference between scaling and decoupling only becomes important at very small energy scales. Since we have a temperature of order of 100 MeV, we expect that we will not be sensitive to this ambiguity.

5.2 Dressed Polyakov loop for two and three colours

With the gluon fixed, it only remains to fix the parameters in the quark-gluon vertex. We will use $d_2 = 0.5\,\mathrm{GeV}^2$ and $\Lambda = 1.4\,\mathrm{GeV}$ as typical scales for QCD. In this quenched calculation we set $d_1 = 4.5\,\mathrm{GeV}^2$. The quark mass is chosen as $m(80\text{ GeV}) = 3$ MeV.

In Fig. 5.5 we show the dressed Polyakov loop and the quark condensate as a function of temperature. Additional to the $SU(3)$ case, which we assume for the rest of this work, we also show results for $SU(2)$. T_c is 303 and 277 MeV for two and three
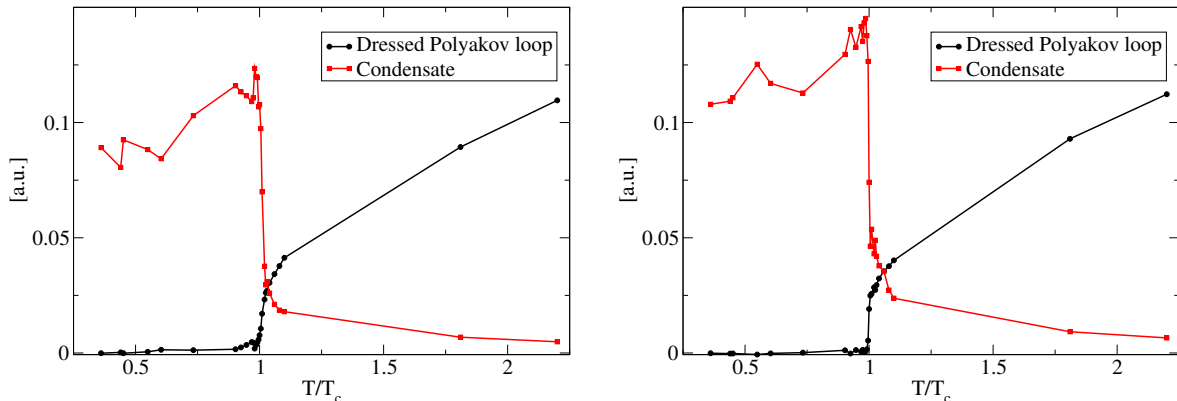
Figure 5.5: Dressed Polyakov loop and quark condensate for $SU(2)$ (left) and $SU(3)$ (right).

colours, respectively. On the lattice, T_c has been determined from the Polyakov loop. We inherit this scale from the gluon input. At T_c we observe a rapid change of both order parameters. While chiral symmetry is approximately restored, centre symmetry is broken. Both transitions happen at the same temperature, which is the same as the one determined from the Polyakov loop. Having more points on the temperature axis than in the previous studies [40, 42, 91], the order of the phase transition becomes more clearly visible. With the finite resolution on the temperature axis and with the finite-volume input from the lattice, it is, strictly speaking, impossible to distinguish between a first and a second order phase transition. Nonetheless, the transition determined from the dual condensate in the $SU(3)$-case is clearly stronger than for two colours. This is in agreement with the general expectation of a first (second) order phase transition for three (two) colours. From the chiral phase transition this distinction can not be made so clearly, although the condensate drops steeper for the three-colour case. Below T_c we observe a rise of the condensate. This is in line with lattice calculations [97] of quenched QCD. We can ascribe this behaviour to the longitudinal part of the gluon propagator, which shows a similar rise. Note that the noisy behaviour of the condensate below T_c is due to the lattice data, which are by nature noisy.

The most important result of this chapter is the consistency of the dressed Polyakov loop with zero below T_c. This shows conserved centre symmetry, and most importantly that our usage of the dressed Polyakov loop is capable of showing this. Had we used different gluon propagators as an input in our quark DSE, we could not have gotten this result. This is a non-trivial statement, although below T_c there is some dependence of Σ_1 on the vertex parameters. This has also been found in [98]. While Σ_1 is less consistent with zero for $d_1 \neq 4.5$ GeV^2, the fact that we can find a parameter d_1 for which $\Sigma_1 \approx 0$ for $T \in [0, T_c]$ proves that our vertex *ansatz* is sufficient for this purpose.

5.3 Summary

We introduced quenched QCD in the Dyson-Schwinger framework. To this end, we used results from gauge-fixed lattice QCD for the gluon propagator. We used a fit that has been employed successfully in [42] and applied it to recently refined lattice data. From this input we obtained the condensate and dressed Polyakov loop as order parameters for chiral symmetry breaking and confinement. This has been mainly a repetition of [42], but with the newer lattice data we could resolve the behaviour of the order parameters around T_c more precisely. Our results are consistent with a transition of first (second) order for SU(3) (SU(2)). This shows that our order parameters, especially the dressed Polyakov loop, indeed can be used to study chiral symmetry breaking and confinement.

To access the quenched gluon propagator at momenta outside the temperatures where lattice data are available, we proposed a polynomial fit through the gluon parameters. With this as a basis we will put forward a truncation scheme for unquenched QCD in the following two chapters.

6 $N_f = 2$ QCD with bare sea quarks

In general the quark and gluon DSEs, Figs. (2.1,5.1), are coupled integral equations which have to be solved simultaneously. In the last chapter we used lattice QCD results for the pure Yang-Mills gluon propagator. In this and the next chapter we will use this as the basis to develop an approximation for the unquenched gluon propagator. Here, we will additionally use bare quarks in the quark loop of the gluon DSE. This is a huge simplification in terms of numerics, since we can take the analytic results from the hard thermal/dense loop (HTL/HDL) scheme. This amounts of two approximation steps. First of all, the quarks in the loop are undressed and massless, which is a reasonable approximation in the quark-gluon plasma. Secondly, in HTL approximation appearances of the external momentum in the numerator of the integrand are neglected. This means to neglect the vacuum part of the loop, and does certainly not affect the thermal mass which is generated from the quark loop and which will turn out to be the most important thermal effect.

6.1 Unquenching the gluon propagator

In the last chapter we studied quenched QCD. Diagrammatically speaking, this means to drop the quark loop from the gluon DSE, see Fig. (5.1). Since we want to study full QCD and its phase diagram, we have to unquench the gluon. This means we have to take the quark loop into account, which will lead to a gluon propagator that depends on the quark mass and the chemical potential.

Figure 6.1: The truncated gluon DSE with bare quarks in the quark loop. The gluon propagator with the yellow dot denotes the quenched gluon propagator.

In general, one has to solve the fully coupled gluon, ghost and quark DSEs in order to access the unquenched gluon propagator. This is a tremendous task outside the scope of this work. Luckily, we can use an approximation that simplifies the situation considerably. We will substitute the Yang-Mills self-energies in the gluon DSE, Eq. (5.1), by the inverse quenched gluon propagator. We keep the quark loop and find the unquenched inverse gluon propagator as a result. In this approximation any

back-coupling effect of the sea quarks on the Yang-Mills self-energies is neglected. The assumption that this approximation is reasonable can be checked by comparing to explicit solutions of the full quark-gluon-ghost system in the vacuum. In Fig. 6.2, we show the result of this test on the ground of the Yang-Mills system as it was truncated in [99, 100]. We solve the full system of equations, with quark loop in the Yang-Mills self-energies taken into account, and in the approximation of merely adding the quark loop to the quenched gluon. On the quark side we use the same quark-gluon vertex as in the rest of this work, with $d_1 = 7.5$ GeV^2 and a quark mass of $m(80$ GeV$) = 2$ MeV.
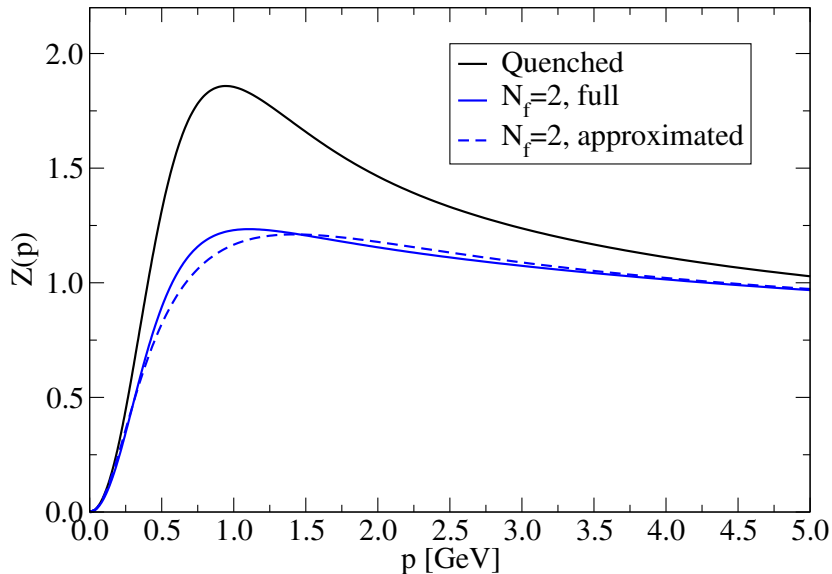

Figure 6.2: Comparison of the full solution of the coupled quark, gluon and ghost DSEs to our approximation. As a comparison we also show the quenched input. Figure courtesy of Christian Fischer.

Note that the scale of the Yang-Mills sector changes when the quark loop is taken into account. We accommodate this by requiring the gluon dressing function to have its peak at the same value as in the quenched case. We find that indeed the fully and the approximately unquenched gluon differ only on a 10 percent level.

However, at large temperatures and small quark masses the quark loop becomes more important. This can be expected to also increase the back-coupling effects in the Yang-Mills self-energies. In chapter 7, where we will include the full dressing of the quarks in the quark loop, we can expect that our approximation holds up to T_c similarly well as in the vacuum due to the dynamically generated quark mass. In this chapter, on the other hand, this is not the case and we can expect larger truncation effects. In section 7.5.1 we will furthermore compare the unquenched gluon with the fully dressed quark loop at finite temperature to lattice results. There, the agreement will be found to be on a similar level like in Fig. 6.2, but for a rather large quark mass.

6.1.1 Bare-quark approximation

The second approximation that we will use in this chapter is to use only bare quarks in the quark loop. We still dress the quark-gluon vertex with the same *ansatz* we use in the quark self-energy. This leads to a truncation that has also been used in studies of the colour-superconducting phases [35, 36]. This is certainly valid for large temperatures/densities, where QCD is in a weakly coupled phase. Around and below the phase transition we will have to use an improved truncation that takes the quark dressings into account. This will be studied in the next chapter.

The resulting gluon DSE is shown in Fig. 6.1. The quark loop is described by

$$\Pi_{\mu\nu}(p) = \frac{Z_{1F}N_f}{2} \sum_l \!\!\!\!\!\! \oint \ \text{Tr}\left[S_0(l)g\gamma_\mu S_0(q)g\Gamma^0_\nu(l,q;p) \right], \tag{6.1}$$

where S_0 is the bare quark propagator and Γ^0 is the quark-gluon vertex without the Ball-Chiu terms. With the projectors Eqs. (2.42,2.43) we project this tensor on its longitudinal and transversal parts. With this, the gluon DSE becomes

$$\left(Z_{T,L}(\vec{p}^2, \omega_p) \right)^{-1} = \left(Z^{qu.}_{T,L}(\vec{p}^2, \omega_p) \right)^{-1} + \Pi_{T,L}(\vec{p}^2, \omega_p)/p^2, \tag{6.2}$$

where $\Pi_T = P^T_{\mu\nu}\Pi_{\mu\nu}/2$ and $\Pi_L = P^L_{\mu\nu}\Pi_{\mu\nu}$. We evaluate $\Pi_{T,L}$ in HTL-like approximation, following the line of [101]. The only difference to HTL is that we take the vertex dressing function Γ into account, and take it to depend on the gluon momentum. This way, we can perform the loop integration in the usual way. The result is

$$\Pi_L(\vec{p}^2, \omega_p) = \Gamma(p^2)\frac{2m^2_{th.}p^2}{\vec{p}^2}\left[1 + \frac{\omega_p}{2|\vec{p}|}\left(-\pi + 2\text{atan}\left(\frac{\omega_p}{|\vec{p}|} \right) \right) \right], \tag{6.3}$$

$$\Pi_T(\vec{p}^2, \omega_p) = \Gamma(p^2)m^2_{th.} - \frac{\Pi_L(\vec{p}^2, \omega_p)}{2}, \tag{6.4}$$

where the thermal mass is given by

$$m^2_{th.} = \frac{g^2N_f}{12}\left(T^2 + \frac{3}{\pi^2}\mu^2 \right). \tag{6.5}$$

Note that $\lim_{\vec{p}^2 \to 0} \Pi_L(\vec{p}^2, 0) = 2m^2_{th.}\Gamma(0)$, while $\lim_{\vec{p}^2 \to 0} \Pi_T(\vec{p}^2, 0) = 0$. This means that the quark loop leads to Debye screening of the electric part of the gluon propagator. In the (colour-)superconducting phase a related Meissner mass appears in the magnetic part.

For the vertex parameters we will carry on with those used in the quenched study, *i.e.* $d_1 = 4.5 \text{ GeV}^2$.

6.2 Results for $\mu = 0$

We will first test our truncation for $\mu = 0$ and $N_f = 2$. Going from quenched to unquenched QCD has the main effect of reducing the gluon propagator. We thus
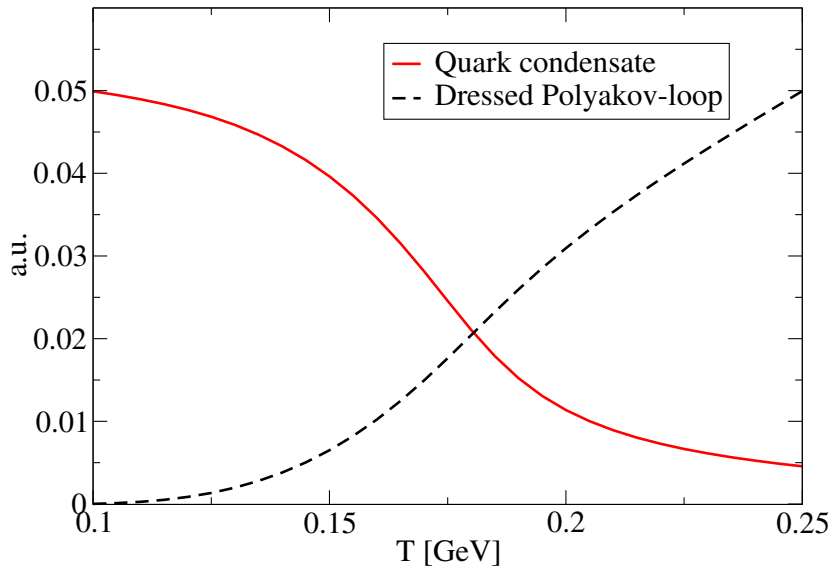
Figure 6.3: The quark condensate as well as the dressed Polyakov loop as a function of temperature in two-flavour QCD with bare sea quarks.

expect to find a lower value for T_c. In Fig. 6.3 we show the quark condensate and the dressed Polyakov loop. As expected, the transition temperature is reduced and we find a cross-over in contrast to the first order phase transition in quenched QCD. This is in line with results from lattice QCD, where for physical quark masses also a cross-over is found with a T_c in the same ballpark. We will define T_c by

$$\max\left[\frac{d\mathcal{O}}{dm}\right], \tag{6.6}$$

where $\mathcal{O}$ is the order parameter, either the quark condensate or the dual condensate. For the chiral transition we find $T_c^{N_f=2} = 180 \pm 5$ MeV and for deconfinement $T_{deconf}^{N_f=2} = 195 \pm 5$ MeV.

In the quenched case, as discussed in the last chapter, we found an increase of the quark condensate below T_c. This we attributed to the longitudinal part of the gluon propagator, which shows the same rising behaviour. This behaviour vanishes in the unquenched case, where we find a monotonically decreasing condensate. This can be understood by the Debye screening mass from the quark loop, which suppresses the longitudinal gluon propagator.

The dual order parameter shows a non-zero value for all temperatures, which is the same behaviour that the (thin) Polyakov loop in lattice simulations shows. This can be interpreted as the breaking of centre symmetry by the presence of dynamical quarks. We find that chiral restoration and deconfinement, which are of cross-over nature, happen in the same temperature regime. This is again in agreement with lattice simulations.
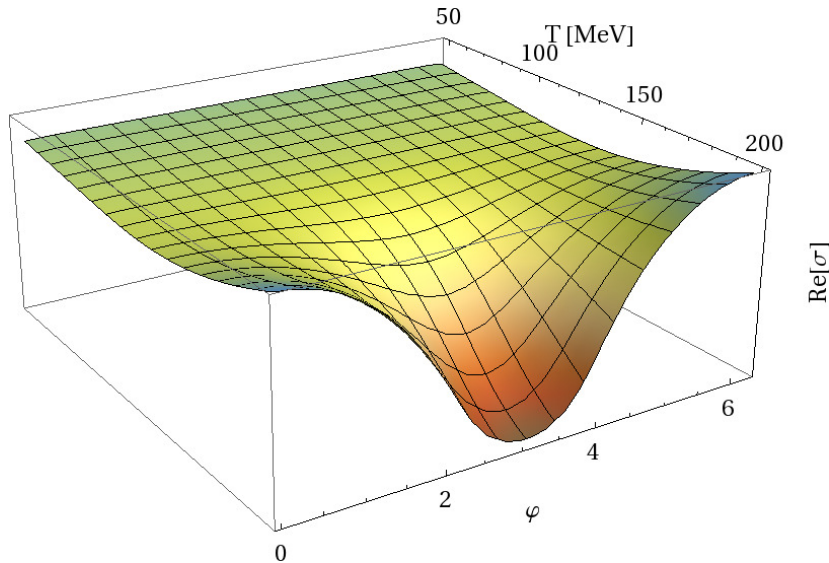
Figure 6.4: The quark condensate $\sigma = \langle\bar{\psi}\psi\rangle_\varphi$ as a function of temperature and boundary angle φ at fixed quark chemical potential $\mu = 0$ MeV.

In Fig. 6.4 we show the condensate as a function of temperature and the quark boundary angle φ. For small temperatures, we find a condensate that barely depends on φ. When the temperature is increased, chiral symmetry is restored and the condensate at $\varphi = \pi$ drops. In contrast to that, for $\varphi = 0, 2\pi$ the condensate continues to increase even in the chirally symmetric phase. This has already been discussed in Ref. [40]. In the Fourier transform for the dual condensate, this leads to a small value of Σ_1 for low temperatures, and a larger value of Σ_1 above T_c.

To conclude, we find the expected physics at $\mu = 0$. This shows that with our unquenched gluon propagator we capture the main effects when going from quenched to unquenched QCD. This gives us confidence to proceed with finite chemical potential, where a direct comparison with lattice results is no longer possible.

6.3 Finite chemical potential

When we switch on the chemical potential, we find a new feature of the condensate in the $T - \varphi$ plane. For $\varphi \neq 0, \pi, 2\pi$ the boundary angle acts similar to an imaginary chemical potential. Together with the finite value of μ, we have a situation similar to a complex chemical potential. This has the effect of rendering the quark condensate complex. The real and imaginary parts of the condensate are shown in Fig. 6.5 for $\mu = 200$ MeV. The imaginary part of the condensate is antisymmetric around $\varphi = \pi$. If we now look at the Fourier transform

$$\Sigma_{\pm 1} = \int_\varphi e^{\mp i\varphi}\langle\bar{\psi}\psi\rangle_\varphi = \int_\varphi \cos\varphi \mathrm{Re}\langle\bar{\psi}\psi\rangle_\varphi \pm \sin\varphi \mathrm{Im}\langle\bar{\psi}\psi\rangle_\varphi, \qquad (6.7)$$
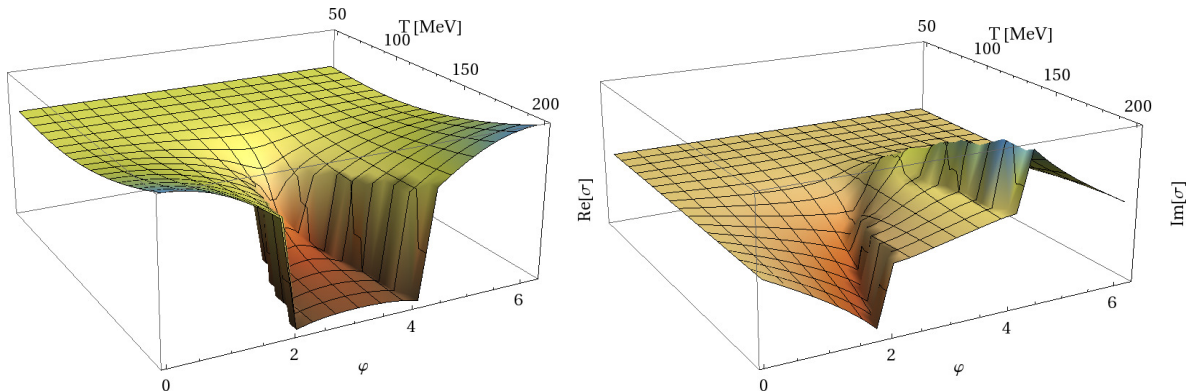
Figure 6.5: The real and imaginary parts of the quark condensate $\sigma = \langle \bar{\psi}\psi \rangle_\varphi$ as a function of temperature and boundary angle φ at fixed quark chemical potential $\mu = 200$ MeV.

we find a real result for $\Sigma_{\pm 1}$. However, $\Sigma_{+1} \neq \Sigma_{-1}$ for $\mu > 0$. This reflects that at finite μ quarks and antiquarks are different. It is well-known that the Polyakov loop and its conjugate behave differently at finite μ. What we find here is the same phenomenon, and we will call Σ_{-1} the dressed conjugated Polyakov loop. Also, we find a jump of the condensate in φ-direction for $T > T_c$ at finite μ. This structure has also been found in NJL studies of the dual condensate [102], although the interpretation of the dual condensate as an order parameter for centre symmetry does not hold in the NJL model. This points towards a general feature of the condensate at finite μ and unphysical φ. We observe that the temperature at which the jump is first developed decreases with increasing chemical potential. However, this jump does not reflect in a jump of the resulting dual condensates. The function $\Sigma_{\pm 1}(T)$ is still continuous, at least for chemical potentials up to the critical end-point. We can now calculate the phase diagram for chiral symmetry restoration and deconfinement. The result is shown in Fig. 6.6. At small chemical potential we find a crossover for both transitions, as explained above for $\mu = 0$. We find a pseudo-critical temperature for deconfinement that is larger than that for chiral restoration by up to 20 MeV. Although this difference increases slightly around $\mu = 50$ MeV, it decreases for larger μ, and vanishes at about $\mu = 200$ MeV. The deconfinement temperatures evaluated from Σ_{+1} and Σ_{-1} are identical in the limits of our numerical precision, although $\Sigma_{+1} > \Sigma_{-1}$ for $\mu > 0$. We will show the dual condensates at finite μ in the next chapter.

For the chiral transition we find a crossover that gets steeper with increasing chemical potential, until it turns into a first order phase transition at a critical end-point (CEP) which is located at $(\mu_{EP}, T_{EP}) \approx (280, 95)$ MeV. Above the CEP, we find a co-existence region, in which one needs to evaluate the pressure in order to obtain the phase that is realised physically. Since we do not have access to the pressure in this work, we can thus not resolve the transition temperature in the first order region and will only denote the spinodals. See App. B.1.2 for our numerical procedure for finding the spinodals.
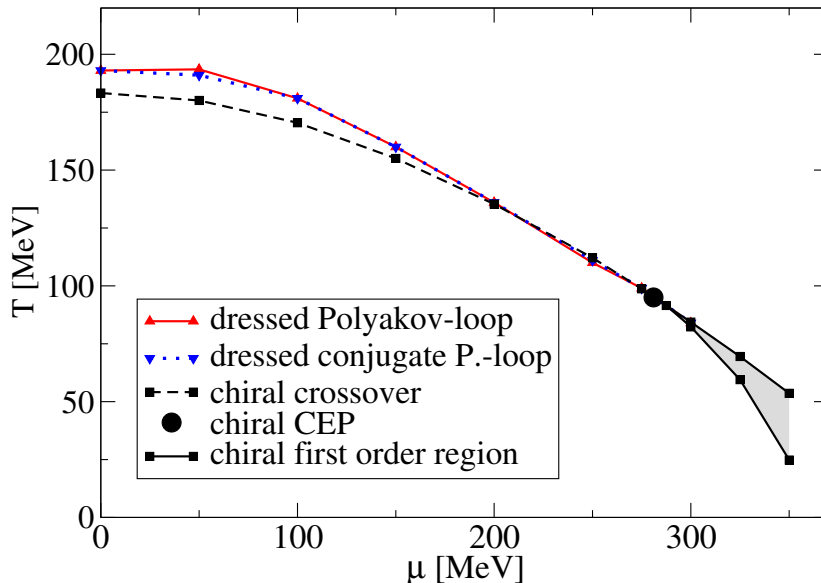
Figure 6.6: The phase diagram for chiral symmetry restoration and deconfinement of quarks (Σ_1) and antiquarks (Σ_{-1}) in the HTL-like approximation with two flavours.

The CEP is located at a relatively large chemical potential, with $\mu_{EP}/T_{EP} \approx 3$. This can be attributed to the inclusion of fermionic fluctuations. A similar conclusion has been drawn in the framework of the PQM model [25]. This is especially interesting for extrapolations of lattice simulations to finite chemical potential. These fail at $\mu/T \approx 1$. In [103] no signal for a CEP has been found for $\mu/T < 1$, which agrees with the findings in our and the PQM model.

On the other hand, we do not expect our current truncation to be valid in the area of the phase diagram where we find the CEP. For chemical potentials of this magnitude one expects that baryons play an important role. Also, entirely new phases may be found instead of the first order phase transition, for instance an inhomogeneous phase. [31]

We do not calculate the dual condensates in the first order region. To do so credibly one would have to obtain the phase of the lower pressure. This is not only hindered by our technical problems of accessing the pressure, it is also in general a problem at unphysical boundary conditions. There, one would find a complex pressure similar to the complex condensate that we discussed above. With the complex numbers being unordered, one could not determine which phase has the lower pressure. A possible solution would be to resort to e.g. taking the absolute value or the real part of the pressure for the comparison. This has been done in the NJL-model studies of the dual condensate [102]. However, this is merely a pragmatic treatment of a more fundamental problem. The solution of this problem might require a better understanding of the dual condensates. The only statement that can be made at the moment is that above

the upper spinodal, the dual condensates will acquire a large value. Thus a phase of confined but chirally symmetric matter could only be found inside the coexistence region, if at all.

6.4 Summary

In this chapter we introduced a truncation for unquenched gluon propagators with bare sea quarks. The idea is to add the quark loop to the quenched gluon propagator, neglecting unquenching effects in the Yang-Mills self-energies. This approximation was found to work well in the vacuum, where explicit calculations of both, the approximated and the full system are possible. We therefore applied it to finite temperature and density as well.

We found that our truncation reproduces a lot of the physics that is expected in unquenched QCD, namely a cross-over transition at $\mu = 0$ for both, chiral restoration and deconfinement. We obtain the standard version of the QCD phase diagram, with a CEP at relatively large μ. The dual order parameters lead to the expected behaviour at $\mu = 0$, and to a deconfinement transition that is near-by the chiral restoration at all accessible chemical potentials. A novel feature of the condensate appeared when finite chemical potentials and unphysical quark boundary conditions φ were taken into account. The condensate showed a first order transition in φ-direction, for μ sufficiently large and temperatures above T_c. This behaviour is independent of the truncation, and can even be found in the NJL model.

The success of obtaining the expected behaviour of unquenched QCD makes this technically relatively simple truncation for the unquenched gluon propagator a good choice for further studies of QCD at finite density with Dyson-Schwinger equations, when only qualitative features are of interest. However, we expect this truncation to be too simple to describe the physics close to the phase transition correctly. This is the main motivation to improve upon this situation in the next chapter, where we include fully dressed quarks in the quark loop. This is technically much more demanding than the HTL approximation. Nevertheless, this will be necessary to yield more quantitative results and to include strange quarks in a non-trivial way.

7 $N_f = 2$ and $N_f = 2 + 1$ QCD with fully dressed sea quarks

In the last chapter we approximated the quark loop in the gluon DSE by considering the quarks to be bare. We only dressed the quark-gluon vertex, which is only a reasonable approximation well above the phase transition. In this chapter we therefore improve the truncation by explicitly taking the fully dressed quark propagator in the quark loop into account. This leads to a coupled system of equations for the quark and gluon propagators, which will make the gluon sensitive to the chiral dynamics in the quark sector. In this truncation we are able to couple light and strange quarks.

7.1 Improved truncation scheme
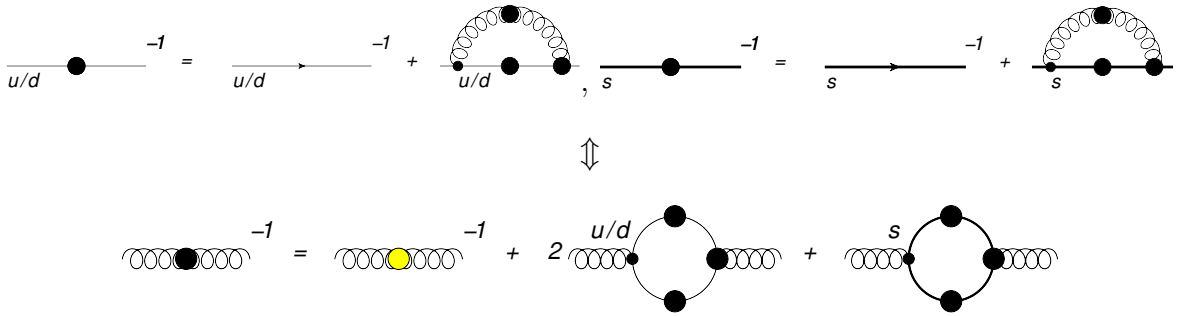
Figure 7.1: The coupled system of light-quark, strange-quark and gluon DSEs. The thin and thick lines represent light and strange quarks, the yellow dot in the gluon DSE the quenched gluon.

We show the system of quark and gluon DSEs in this truncation in Fig. 7.1, where we already add a strange quark for the $N_f = 2 + 1$ case. The DSEs read

$$\left[S^f(p)\right]^{-1} = Z_2^f \left[S_0^f(p)\right]^{-1} + C_F Z_2^f Z_{1F}^f \sum_l \!\!\!\!\!\!\int g\gamma_\mu S^f(l) g\Gamma_\nu^f(l,p;q) D_{\mu\nu}(q), \qquad (7.1)$$

$$D_{\mu\nu}^{-1}(p) = \left[D_{\mu\nu}^{qu.}(p)\right]^{-1} - \sum_f^{N_f} \frac{Z_2^f}{2} \underbrace{\sum_l \!\!\!\!\!\!\int \mathrm{Tr}\left[g\gamma_\mu S^f(l) g\Gamma_\nu^f(l,q;p) S^f(q)\right]}_{\Pi_{\mu\nu}(p)}, \qquad (7.2)$$

for quarks of flavour $f \in \{u, d, s\}$. We choose the relative momentum $q = p - l$ in the quark DSE, and $q = p + l$ in the quark loop $\Pi_{\mu\nu}$. In the quark loop we evaluate the vertex *ansatz* function at $\Gamma(l^2, q^2, p^2) = \Gamma(l^2 + q^2)$, *i.e.* for the sum of squared quark momenta. In the same way as in the previous chapter, we will project the quark loop on the transversal and longitudinal parts

$$\Pi^T(p) = P^T_{\mu\nu}(p)\Pi^T_{\mu\nu}(p)/2, \tag{7.3}$$

$$\Pi^L(p) = P^L_{\mu\nu}(p)\Pi^L_{\mu\nu}(p). \tag{7.4}$$

The quark loop contributes to the thermal masses of the gluon. This is the dominant thermal effect. To make the thermal mass explicit, we can split the quark-loop contribution into an IR-finite and vanishing part

$$\Pi^{T,L}(\vec{p}^2, \omega_p) = -2\left(m^{T,L}_{th.}\right)^2 + \Pi^{T,L}_{reg.}(\vec{p}^2, \omega_p), \tag{7.5}$$

where $\Pi^{T,L}_{reg.}$ is similar to the quark loop in vacuum. The thermal masses are defined as

$$\left(m^{T,L}_{th.}\right)^2 = -\frac{1}{2}\,\Pi^{T,L}(\vec{p}^2, \omega_p = 0)\big|_{\vec{p}\to 0}\,, \tag{7.6}$$

where the electric screening mass m^L is known as the Debye mass and is always present in the medium. In contrast to that, the magnetic screening mass m^T is the Meissner mass and appears only in the colour-superconducting phase.

7.2 UV finiteness of the quark loop

Before we can evaluate Eq. (7.2), we need to take care of a spurious quadratic divergence that appears in the gluon self-energies. This divergence appears due to the use of a cutoff, which breaks translational invariance. It leads to a term similar to a thermal mass, *i.e.* we get

$$\Pi^L(0) = aT^2 + b\mu^2 + c\Lambda^2, \tag{7.7}$$

with some constants a, b, c and the cutoff Λ. We have to remove only the last term carefully, without spoiling the other two terms.

Let us investigate the situation in the vacuum first, since medium effects do not contribute to the divergence. Additionally to the quadratic divergence, we find a spurious component longitudinal to the gluon momentum. We can split a general gluon self-energy $\Pi_{\mu\nu}$ into

$$\Pi_{\mu\nu} = \Pi^{\mathcal{L}}P^{\mathcal{L}}_{\mu\nu} + \Pi^{\mathcal{T}}P^{\mathcal{T}}_{\mu\nu}, \tag{7.8}$$

where $\mathcal{L}, \mathcal{T}$ now denote longitudinal and transversal with respect to the gluon momentum, and should not be confused with L, T which denote longitudinal and transversal with respect to the heat bath. The corresponding projectors are

$$P^{\mathcal{L}}_{\mu\nu} = \frac{p_\mu p_\nu}{p^2}, \qquad P^{\mathcal{T}}_{\mu\nu} = \delta_{\mu\nu} - \frac{p_\mu p_\nu}{p^2}. \tag{7.9}$$

The longitudinal part is quadratically divergent, $\Pi^{\mathcal{L}} \propto \Lambda^2$. We can use this to cancel the divergence in the transversal part by defining

$$\Pi^r_{\mu\nu} = \Pi_{\mu\nu} - \delta_{\mu\nu} \frac{p_\alpha p_\beta}{p^2} \Pi_{\alpha\beta} \tag{7.10}$$

$$= P^{\mathcal{T}}_{\mu\nu} \left(\Pi^{\mathcal{T}} - \Pi^{\mathcal{L}} \right), \tag{7.11}$$

see [104]. This is the same as using the Brown-Pennington projector $P^{BP}_{\mu\nu} = \delta_{\mu\nu} - 4\frac{p_\mu p_\nu}{p^2}$ [105, 106] on $\Pi_{\mu\nu}$ directly. The quadratic divergence from the transversal and longitudinal part cancel, and the result is only logarithmically divergent.

We can now use the projectors longitudinal and transversal with respect to the heat-bath on Eq. (7.10), which yields in some sense the generalisation of the Brown-Pennington projector to finite temperature. Thus we get the quark loop (or potentially the other gluon self-energies) at finite temperature without the quadratic divergence. With the quark-gluon vertex from Eq. (4.5) the result is

$$\Pi^T(\vec{p}^2, 0) = \frac{4Z_2 g^2}{2} \sum_l \!\!\!\!\!\!\!\!\!\!\int \frac{\Gamma(l^2, q^2, p^2)}{D_q(l) D_q(q)} \left\{ A(l) A(q) \Gamma_s \left(3\frac{(\vec{l} \cdot \vec{p})^2}{\vec{p}^2} + 2\vec{l}\vec{p} - \vec{l}^2 \right) \right\}, \tag{7.12}$$

$$\Pi^L(\vec{p}^2, 0) = \frac{4Z_2 g^2}{2} \sum_l \!\!\!\!\!\!\!\!\!\!\int \frac{\Gamma(l^2, q^2, p^2)}{D_q(l) D_q(q)} \left\{ A(l) A(q) \left[\Gamma_s \left(2\frac{\vec{l} \cdot \vec{p}\vec{p} \cdot \vec{q}}{\vec{p}^2} - \vec{l}\vec{q} \right) + \Gamma_4 \vec{l} \cdot \vec{q} \right] \right.$$

$$\left. + B(l) B(q) \left[\Gamma_4 - \Gamma_s \right] + C(l) C(q) \left[-\tilde{\omega}_l^2 (\Gamma_s + \Gamma_4) \right] \right\}, \tag{7.13}$$

where we have $q = p + l$, and the quark denominator $D_q(p) = \vec{p}^2 A^2(p) + \tilde{\omega}_p^2 C^2(p) + B^2(p)$. The factor 4 comes from the Dirac trace. We neglected the momentum dependence of $\Gamma_s(l, q)$ and $\Gamma_4(l, q)$ which we defined in Eq. (4.6) for brevity. These equations are defined for one quark flavour. Some further details on how we evaluate the resulting expressions are given in App. (B.2).

As indicated in Eqs. (7.12,7.13), we only evaluate the zero mode explicitly. The higher modes are accessed by using $\Pi^{T,L}(\vec{p}^2, \omega_p) \rightarrow \Pi^{T,L}(\vec{p}^2 + \omega_p^2, 0)$. We use the same approximation in the quenched gluon propagator, where we only have the zero mode from the lattice. As the most important medium effect we can now extract the thermal masses from Eqs. (7.12,7.13). To this end we take the limit $\vec{p}^2 \rightarrow 0$, and obtain

$$2 \left(m^T_{th.} \right)^2 = 0, \tag{7.14}$$

$$2 \left(m^L_{th.} \right)^2 = -\frac{4Z_2 g^2}{2} \sum_l \!\!\!\!\!\!\!\!\!\!\int \frac{\Gamma(l^2, l^2, 0)}{D_q^2(l)} \left\{ A^2(l)\vec{l}^2 \left(-\frac{1}{3}\Gamma_s(l, l) + \Gamma_4(l, l) \right) \right.$$

$$\left. + B^2(l) \left(-\Gamma_s(l, l) + \Gamma_4(l, l) \right) - C^2(l)\tilde{\omega}_l^2 \left(\Gamma_s(l, l) + \Gamma_4(l, l) \right) \right\}. \tag{7.15}$$

This includes the correct high-temperature/density limit, $\left(m^T_{th.} \right)^2 = 0$ and $\left(m^L_{th.} \right)^2 = \frac{g^2}{12} \left(T^2 + 3\frac{\mu^2}{\pi^2} \right)$ *i.e.* the HTL result from the last chapter. We therefore validated that

our approach of removing the quadratic divergence does not impair the medium effects of the quark loop, we only removed the Λ^2-term in Eq. (7.7).

7.3 The coupling of light and strange quarks

Our truncation scheme allows for a non-trivial coupling of light and strange quarks. In the vacuum, a similar set-up has been studied in [99], but the present work is the first study of in-medium QCD with $N_f = 2 + 1$ in the Dyson-Schwinger framework. In Fig. 7.1 we show the coupled system of light quark, strange quark and gluon. However, there are further unquenching effects that we do not take into account. Besides the back-coupling of the quark loop in the Yang-Mills self-energies, there are quark loop effects in the quark-gluon vertex. One possibility of addressing these effects is to take the back-coupling of mesons into account. We shall study this in chapter 9. Especially the exchange of kaons could lead to a further coupling of light and strange quarks that we do not include in the present chapter. Furthermore diquark and baryon effects might play an important role at high densities and low temperatures [107]. These are not discussed in this work.

We will set the strange-quark chemical potential to zero. It is possible in our framework to use different chemical potentials for up, down and strange quarks. This could be used to study non-zero charge and strangeness chemical potentials μ_Q and μ_S. This would be useful to better model the situation in heavy-ion collisions, see e.g. [108]. However, the biggest effect can be expected to come from the light-quark chemical potential, since strange quarks are suppressed by their larger mass. We will leave a further study of the different chemical potentials for future work.

7.4 Fixing the parameters

So far, we fixed the vertex parameters d_1, d_2 and Λ as well as the light-quark mass such that the results where in the right ballpark. In this chapter we will strive for more quantitative results. To this end, we will keep $d_2 = 0.5$ GeV^2 and $\Lambda = 1.4$ GeV as in the previous chapters. For the strange-quark mass we use $m_s/m_l = 27$, see e.g. [109]. We will use two sets for the two remaining parameters d_1 and m_l. In both cases we fix the parameters in the full $N_f = 2 + 1$ calculation, and use them also for $N_f = 2$. This effectively neglects the impact of the strange quark on the quark-gluon vertex.

For **set A** we choose d_1 and m_l such that in the vacuum f_π and M_π are reproduced. To do so, we first set $m_l = 0$, but keep an $m_s > 0$. We then use the Pagels-Stokar formulae Eqs. (2.31,2.32) to obtain the chiral f_π^χ and r_π^χ. We demand $f_\pi^\chi \approx 88$ MeV, which is the expected pion decay constant in the chiral limit, see [110]. With Eq. (2.29) we then determine m_l for $M_\pi = 137$ MeV, and thus m_s. From this procedure we obtain $d_1 = 7.6$ GeV^2, $m_l = 1.2$ MeV and $m_s = 32.4$ MeV.

For **set B** we fit the resulting condensate $\Delta_{l,s}$, see Eq. (3.4), to the results of corresponding lattice studies [12]. The best such fit is obtained for $d_1 = 8.3$ GeV^2 and $m_l = 0.9$ MeV, thus $m_s = 24.3$ MeV. We show the resulting condensate in Fig. 7.7. From these parameters we get $f_\pi^\chi \approx 96$ MeV and $M_\pi \approx 141$ MeV. Obviously f_π is slightly too large in this set, while M_π is reasonable.

Note that we use some approximations in the determination for f_π and M_π. First of all, the Pagels-Stokar formula is known to underestimate f_π. We would thus expect that in set A d_1 is too large, while in set B f_π would turn out larger in a full calculation. Secondly, the Gell–Mann-Oakes-Renner relation is only strictly valid for the trivial case $m_l = 0$. However, for the light quark masses, we do not expect a strong deviation from a full calculation.

	d_1	m_l	m_s	f_π^χ	M_π	T_c	$\langle\bar{\psi}\psi\rangle_\chi^{1/3}$
set A	7.6	1.2	32.4	88	137	149	397
set B	8.3	0.9	24.3	96	141	161	424
set C	7.5	2	54	88	179	156	397

Table 7.1: Summary of our parameter sets. d_1 is given in GeV^2, the other values in MeV. χ denotes chiral light quarks. The quark masses are given at a renormalisation scale of 80 GeV. The values for T_c have been obtained for $N_f = 2 + 1$.

We summarize the parameters and some results in table (7.1). It is noteworthy that the differences between sets A and B are not too large, although the philosophies in their determination are quite different. In simpler rainbow-ladder studies the parameters are tuned to vacuum observables, similar to our set A. In those studies T_c usually turns out rather small [111], while we find a reasonable agreement with the lattice here.

Note that in [44] we constructed our parameter set along the reasoning of set A. However, we made a mistake, and forgot the factor 2 in Eq. (2.29) which results in a too large pion mass. In Tab. (7.1) we called this set C and will only use it in results that show some qualitative features.

7.5 Results for $N_f = 2$

7.5.1 Comparison to unquenched gluon propagator from lattice QCD

Before we continue with physical quark masses and non-zero chemical potentials, we can test our truncation of the gluon DSE by comparing to lattice data that have recently been published in [112]. To match the lattice set-up, we choose a quark mass of $m_l = 6$ MeV at $d_1 = 7.6$ GeV^2, which leads to a pion mass of $M_\pi \approx 316$ MeV in the Gell-Mann–Oakes–Renner relation. This is the smallest pion mass that has been

used in [112]. Fig. 7.2 shows the resulting gluon dressing functions $Z_{L,T}(p^2)$ for three different temperatures. As a comparison we also show the quenched input into our calculations. This serves to better identify the influence of the quark loop.
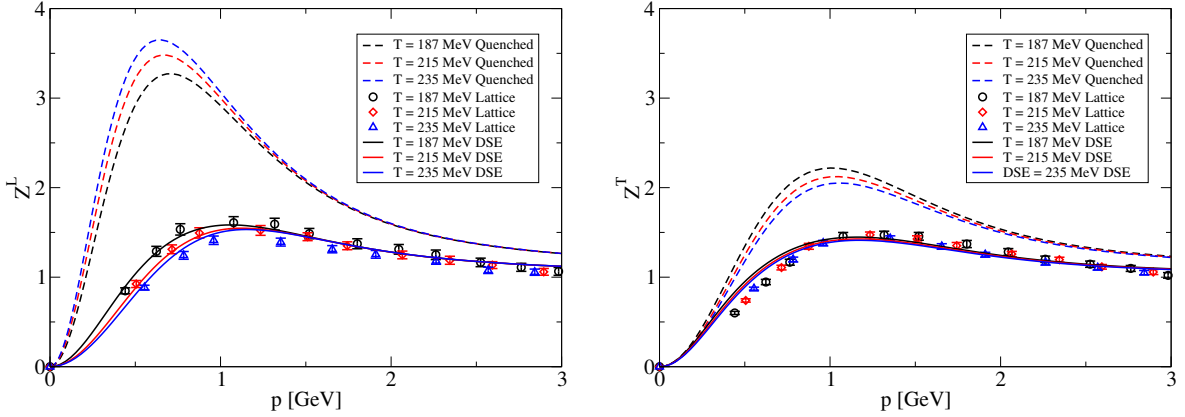

Figure 7.2: Longitudinal and transversal parts of the unquenched gluon propagator, compared to the lattice data for $M_\pi = 316$ MeV from [112].

There is a qualitative agreement of our model with the lattice data in three important effects. First of all, the quark loop leads to a reduction of the gluon propagator in the infrared and the mid-momentum regime. The strength of this reduction is very similar in our calculation and in the lattice data. Secondly, the transversal part is only moderately affected by the temperature, compared to the longitudinal part. This can be understood from Eq. (7.6), where a Debye mass is only generated in the longitudinal part. Thirdly, the longitudinal part decreases with temperature. This is most pronounced in the infrared. In contrast to this, the quenched propagator shows a growing Z_L in this temperature regime. This can again be attributed to the Debye mass, which affects the infrared longitudinal part.

However, there is also some disagreement between our results and the lattice data. In the IR around $p = 0.5$ GeV our solution of Z_T is larger than the lattice result. Also, the maximum of $Z_{L,T}$ is in our case somewhat smaller. These effects might hint at a change of scales that would be induced by the full back-coupling of the quark loop in the Yang-Mills self-energies. In the UV, not shown in Fig. 7.2, the lattice is plagued by artefacts from the missing $O(4)$ invariance. This leads to a bad comparison with our propagator, which is artificial.

Overall, this comparison assures us that we take at least the qualitative features of the unquenched gluon at finite temperature into account. Also the amount of unquenching, *i.e.* the difference of the quenched to the unquenched propagator, agrees on a quantitative level. This also shows that our quark-gluon vertex *ansatz* works well, since this is an input in the quark-loop diagram. In Fig. 6.2, we compared the approximation of adding the quark loop to the quenched propagator with a full solution of the coupled quark-gluon-ghost system in the vacuum, and found a good agreement. With

the comparison of Fig. 7.2, we now have proof that this approximation works well also at finite temperature. On the other hand, in this comparison we used a pion mass of 316 MeV and two flavours. With lighter quark masses, most importantly at their physical values and with $N_f = 2+1$, the quark loop will become stronger. This will also lead to stronger back-coupling effects in the Yang-Mills sector. Thus we can expect our truncation to be worse in this situation than in the comparison in Fig. 7.2. It would certainly be highly interesting to solve the full set of gluon, ghost and quark DSEs at finite temperature. With this full solution one could further test our truncation scheme also at physical quark masses.

Knowing that our truncation leads to reasonable results for the gluon propagator, we are encouraged to go on to physical quark masses and finite chemical potential.

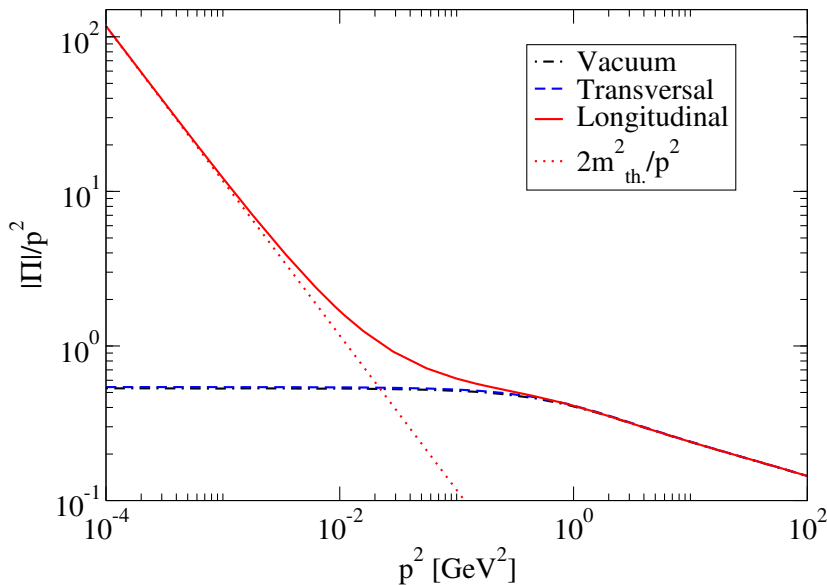## 7.5.2 The phase transition at $\mu = 0$

Figure 7.3: The quark loop dressing functions Π_L, Π_T and Π in the vacuum, without renormalisation. We also show the pure thermal mass term $m_{th.}^2/p^2$. Here we used parameter set A at $T = 100$ MeV and $\mu = 0$.

Let us now discuss physical quark masses in the two-flavour case. The general features that we will find here are also valid for $2 + 1$ flavours.

To illustrate again how the medium affects the quark loop, we show the quark-loop dressing functions in Fig. 7.3. This serves as a proof for Eq. (7.5), where we split the quark loop into an IR-vanishing and an IR-finite part from the thermal masses. While Π_T is very similar to the vacuum quark-loop, Π_L/p^2 clearly shows an $m_{th.}^2/p^2$ behaviour in the IR. This is evidently the dominant thermal effect in the quark loop, while the difference of the IR-vanishing part to the vacuum quark loop is comparably small. At
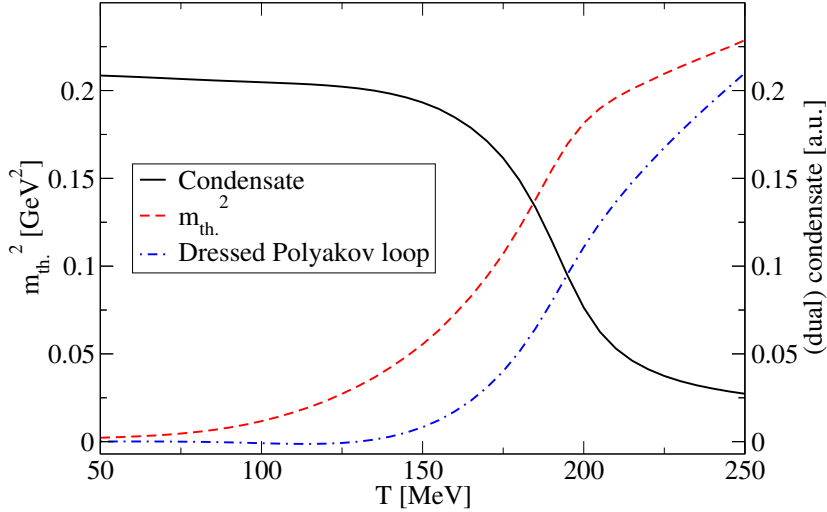
Figure 7.4: We show the quark condensate and the dressed Polyakov loop as the order parameters together with the squared thermal gluon mass as a function of T. We use $N_f = 2$ and $\mu = 0$ with parameter set A.

momenta $p > \pi T$, thermal effects are suppressed and $\Pi_{L,T}$ approach the vacuum quark loop.

In Fig. 7.4 we show the order parameters for chiral symmetry breaking and confinement together with the Debye mass the gluon acquires through the quark loop. We used parameter set A here. With set B the critical temperature is larger, while all qualitative features are the same. As expected in unquenched QCD with finite quark mass, both phase transitions are cross-overs. The quark condensate drops from a large to a small value at around $T_c = 198$ MeV. In the same temperature regime, the dressed Polyakov loop rises from a small to a large value. We find that in the temperature range $T \in [80, 125]$ MeV, the dressed Polyakov loop takes a slightly negative value. This happens because the condensate at $\varphi = \pi$ is larger than at $\varphi = 0, 2\pi$. The effect is rather small, and likely to be an artefact of our quark-gluon vertex, which has no dependence on φ.

So far, these results are qualitatively the same as in chapter 6, where we discussed the HTL-like approximation of the quark loop. That is, the quark loop leads to a smaller transition temperature than in quenched QCD, and turns the first order phase transition into a crossover. We also find similar critical temperatures for chiral restoration and deconfinement. The new feature in the improved truncation is visible in the behaviour of the Debye mass. For small temperatures, the quark loop and therefore also the Debye mass, is suppressed by the large dynamically generated quark mass. When the quark mass is reduced around the phase transition, the Debye mass increases and approaches the $m_{th.}^2 \propto T^2$ behaviour above T_c. In Fig. 6.3 we showed the order parameters at $\mu = 0$ in the HTL-like approximation. The most important difference to Fig. 7.4 is visible below T_c. There, the order parameters in HTL-like approximation

show a stronger dependence on the temperature. Also, the dual condensate is larger compared to the results from the fully dressed quark loop. We can attribute these observations to the over-estimation of the Debye mass in the hadronic phase in the HTL-like approximation. This explains the behaviour of the condensate, and can also be interpreted as an over-estimation of centre-symmetry breaking, and thus the larger dressed Polyakov loop.

The coupling of quark and gluon DSE has an accelerating effect on the phase transition. With the increasing thermal gluon mass, the unquenched gluon propagator is reduced. Since the quark self-energy depends linearly on the gluon, it is also reduced which leads to a smaller generated quark mass. A smaller quark mass in turn leads to an increased thermal gluon mass. This effect is certainly not present in the HTL-like approximation used above, and leads to a steeper crossover. We will see in the next section that this also strongly affects the phase diagram.

7.5.3 The phase diagram
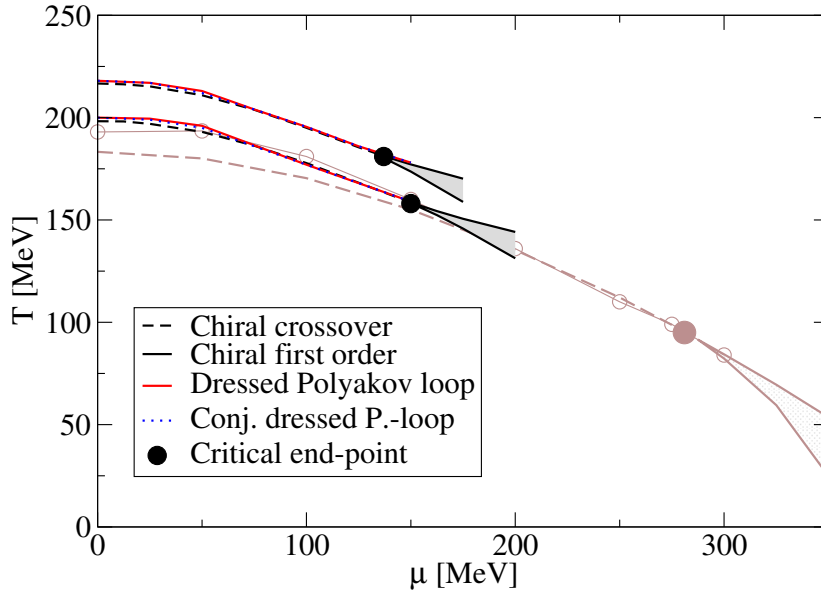
Figure 7.5: The phase diagram for 2 flavours in the $\mu - T$-plane. Here, like everywhere else in this work, μ is the quark chemical potential. The black/red lines correspond to the full solution of the dressed quark loop, while we repeat the results from the HTL-like approximation in lighter colours as a comparison. The results for the upper lines (higher T) are from parameter set B, the lower lines from parameter set A.

Let us now turn to finite chemical potential. We will again determine the critical temperatures from the derivative of the order parameters with respect to the quark

mass, see Eq. (6.6). In Fig. 7.5 we show the resulting phase diagram for chiral restoration and deconfinement and compare to the HTL-like approximation introduced in the last chapter. We find that at $\mu = 0$, $T_c \approx 198$ MeV in parameter set A and $T_c \approx 217$ MeV in set B. This difference of $\Delta T_c \approx 20$ MeV is approximately the same for all chemical potentials. Again, we find that the crossover turns into a first order phase transition at a second-order critical end-point (CEP). For parameter set A we find a CEP at $(\mu_{CEP}, T_{CEP}) \approx (150 \text{ MeV}, 158 \text{ MeV})$, and therefore $\mu_{CEP}/T_{CEP} \approx 0.95$. With parameter set B, the CEP is at slightly smaller chemical potential and larger temperature, with $(\mu_{CEP}, T_{CEP}) \approx (137 \text{ MeV}, 181 \text{ MeV})$, and $\mu_{CEP}/T_{CEP} \approx 0.76$. It is generally expected that the position of the CEP depends on the quark mass m, and is at smaller μ for smaller quark mass. Our results are consistent with this expectation, the smaller μ_{CEP} in set B can be understood from the smaller quark mass compared to set A. In set C, see [44] the CEP is at larger μ compared to set A, due to the even larger (and unphysical) quark masses. Since set A was designed to reproduce the physical pion mass and decay constant, we expect that our prediction of the CEP is more realistic in this parameter set.

For all parameter sets, the ratio μ_{CEP}/T_{CEP} found here is considerably smaller than in the HTL-like truncation. We can attribute this to the accelerated phase transition that we discussed above. Since we find a steeper crossover with growing chemical potential, we hit the CEP sooner when we start from a steeper crossover at $\mu = 0$. This shows the importance of non-perturbative effects around the phase transition. However, we will see below that the addition of strange quarks brings the CEP to larger μ again.

For the deconfinement transition we now determine T_d from Σ_{+1} and Σ_{-1}. See App. B.3 for some details on the numerical difficulties in the evaluation of the dual condensates. We again find near-by pseudo-critical temperatures for chiral restoration and deconfinement. Just like in the HTL-like approximation, the difference between T_d and T_χ is slightly increasing for small chemical potentials, and vanishes already before the CEP is encountered. This behaviour clearly is a general feature of the dual condensate in the way that we implement it. Compared to the HTL-like approximation, the difference between T_d and T_χ is now reduced to only a few MeV. This can be explained by the sensitivity of the gluon to the chiral transition when the full quark loop is taken into account, and means that the deconfinement transition is affected by chiral restoration. Below and close to the chiral phase transition, the sea quarks are suppressed by the generated quark mass. This leads to a smaller amount of centre-symmetry breaking, an effect that vanishes when chiral symmetry is restored. The smaller difference between T_χ and T_d is also connected to the accelerated phase transition, which makes the crossover region smaller, and thus leads to a more constraint definition of the pseudo-critical temperatures. We also find that the deconfinement temperatures determined from Σ_{+1} and Σ_{-1} are the same within the numerical precision.

In [25] and similar work, fermionic fluctuations were included by taking the Debye screening mass for bare quarks into account. The CEP was found at large chemical

potential and small temperature. This way of introducing fermionic fluctuations is quite similar to our HTL-like truncation, and indeed we found a CEP at a similar location in the last chapter. We thus agree on the effect of fermionic fluctuations, however, when we take the full dressing of the quark loop into account, this effect diminishes. We find the Debye mass to be strongly suppressed in the hadronic phase, and to change rapidly at the chiral transition. This leads to a CEP at much smaller chemical potential, which suggests that in [25] the influence of the fermionic fluctuations was overestimated.

7.6 Results for $N_f = 2 + 1$

We now include strange quarks, and study their effects on the order parameters as well as the phase diagram. This leads to the most enhanced truncation that we discuss in this chapter, which will also be the basis for the following chapter about the Polyakov-loop potential.

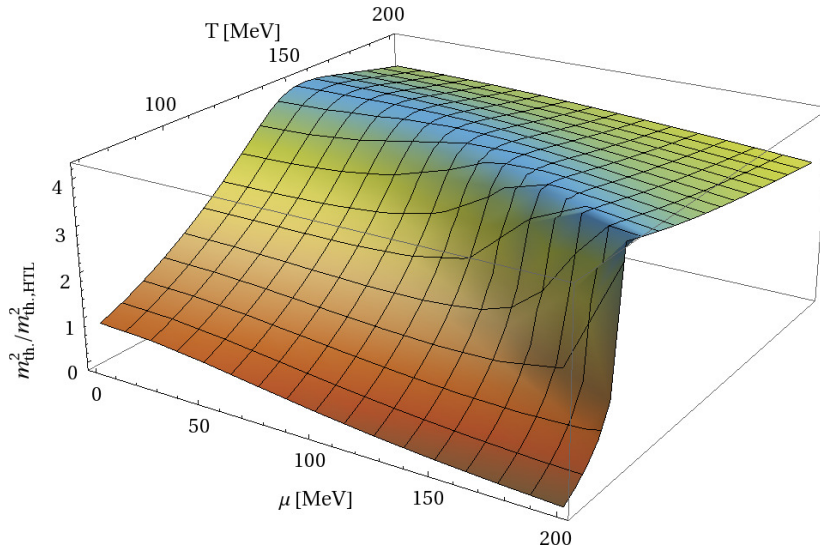### 7.6.1 Order parameters at zero and finite chemical potential

Figure 7.6: The Debye screening mass for the temperatures and chemical potentials that will be relevant for the phase diagram. We normalise by the asymptotic (HTL) value. For this plot, we used parameter set A.

Let us first have a look at the impact of the quark fluctuations on the gluon at all chemical potentials. This is most pronounced in the Debye mass, which we already discussed in the last section for $\mu = 0$ and $N_f = 2$. In Fig. (7.6) we show $m_{th.}^2/m_{th.,HTL}^2$, where $m_{th.,HTL}^2 = \frac{g^2 N_f}{12}\left(T^2 + 3\mu^2/\pi^2\right)$, for a range of temperatures and chemical potentials. In the hadronic phase, the Debye mass is suppressed by the generated quark
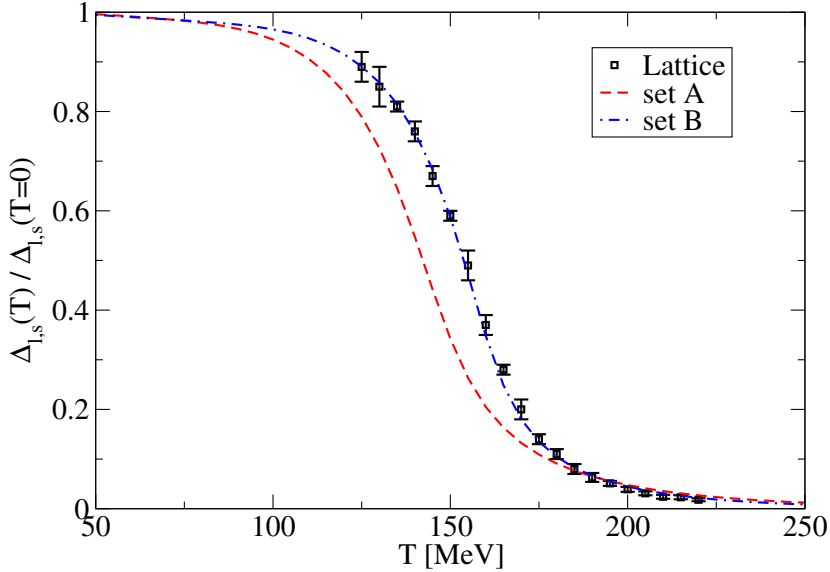
Figure 7.7: The finite condensate $\Delta_{l,s}$, compared to $N_f = 2 + 1$ lattice data [12]. We normalise the condensate to its zero-temperature value, and show results for parameter sets A and B.

mass. In the quark-gluon plasma, it approaches the asymptotic HTL-limit from above. Around the phase transition the Debye mass rises, showing a jump for large chemical potentials where we find a first order phase transition. It is interesting that at small temperatures, $m_{th.}^2$ decreases with the chemical potential and even becomes slightly negative for large μ and small T. This is compensated by the thermal mass from the Yang-Mills sector, which is always larger than the negative contribution from the quark sector. In [37] it has been shown that this behaviour is connected to violations of the Silver-Blaze property. However, this seems to be a relatively small violation. Also, we will concentrate on higher temperatures, where the Silver-Blaze property is not important, and where $m_{th.}^2 > 0$. The behaviour of the Debye mass shows that our gluon is sensitive to the chiral transition and to the chemical potential in a non-trivial way.

We now turn to the quark sector. As a further test of our truncation, we compare the condensate at zero chemical potential to corresponding lattice results [12]. In order to do so, we need to use a version of the condensate that is finite. This is given by $\Delta_{l,s}$, defined in Eq. (3.4). Here, the quadratic divergence between light and strange quark condensate cancels. The result is shown in Fig. 7.7.

We find a clear difference between our parameter sets A and B. For set B, the agreement with the lattice is very good at all temperatures. This is of course due to the fit of the light quark mass and the vertex strength to the lattice condensate. However, with a two-parameter fit it is not trivial that we can obtain a result that agrees pointwise with the lattice. Had we done the same in our HTL-like approximation, we

would not have achieved this level of agreement. This can easily be understood in terms of the Debye screening mass. With the fully dressed quark-loop, we have a suppression of this mass below T_c and an accelerating effect in vicinity of T_c, see the discussion above. The HTL-like approximation misses those features, which leads to a condensate that has a weaker crossover behaviour, see Fig. 6.3. Especially below T_c the condensate lies below the lattice result due to an overestimated thermal effect from the gluon.

For set A, we find a very similar shape of the condensate as a function of temperature. However, T_c is too small by a few MeV when compared to the lattice. This is due to the weaker vertex strength that is necessary to obtain a physical value for the pion decay constant in the vacuum. We also find that the condensate in the chirally symmetric phase is too large compared to the lattice value. In set B, this is compensated by a smaller quark mass. The overestimation of chiral symmetry breaking in the restored phase can be understood in terms of our vertex *ansatz* function Γ. There, we do not take any thermal effects into account. Thermal effects are only present in the Ball-Chiu part of the vertex, which is not very strong. In contrast to that, it has been argued in [77] that the vertex strength d_1 should be reduced above T_c. This was found by comparing spectral functions to lattice results in quenched QCD. The constant d_1 therefore leads to an overestimation of dynamical chiral symmetry breaking in the quark-gluon plasma. In chapter 9, we will improve the vertex truncation by taking meson correlations into account.

Besides the insufficiencies of our truncation, we find that the comparison of our condensate at zero density to lattice data works very well. Although we can not find one parameter set where the vacuum values for the pion observables as well as the comparison to the lattice condensate work at the same time, we find that the difference between sets A and B are not too large. This encourages us to trust our truncation at least at small densities.

We now turn on the chemical potential and solve the coupled set of DSEs. In Fig. 7.8, we show the resulting light and strange quark condensates. We do not remove the quadratic divergence here, and subtract an arbitrary number from the strange quark condensate for the sake of clarity. For the light quark condensate we find a crossover that becomes steeper with growing chemical potential. Eventually it turns into a first order phase transition. The strange quark condensate reacts in a similar way on the transition in the light quark condensate. It has a crossover-like behaviour at small densities and exhibits a jump in the first order regime. However, due to the larger strange quark mass, the condensate continues to drop for larger temperatures. The inflection point of the strange quark condensate is at $T_c^s \approx 245$ MeV, and does not depend strongly on the light-quark chemical potential. At large chemical potential we find that the strange quark condensate first rises slightly before it drops. This is similar to the behaviour of the condensate in simpler truncations, which might hint towards this being a truncation artefact. The reaction of the strange quark condensate on the light quark phase transition is mediated by the gluon. The reduced light quark
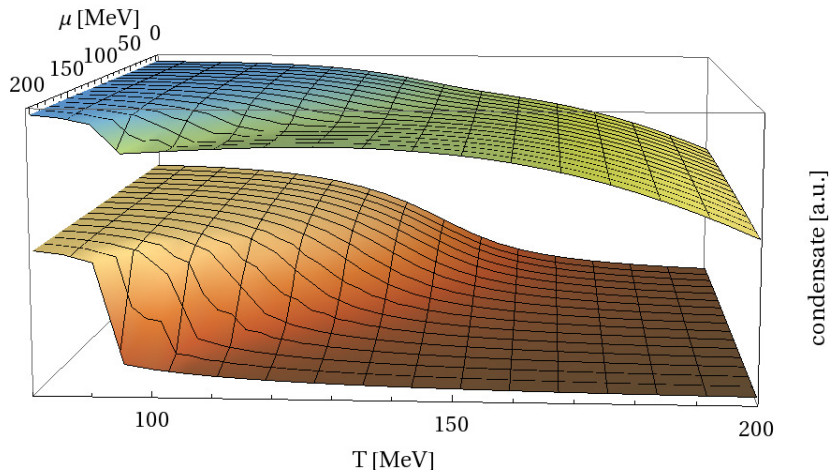
Figure 7.8: The upper surface shows the strange quark condensate and the lower surface that of the light quarks. Here we use parameter set A.
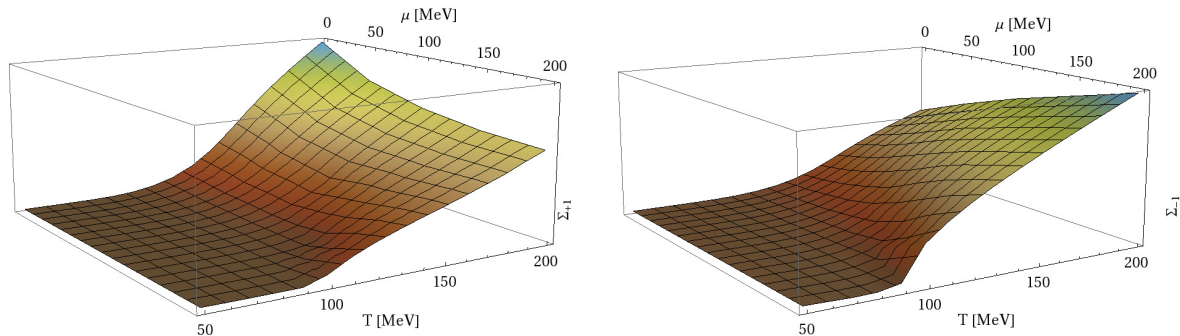

Figure 7.9: The dual condensates Σ_{+1} (left) and Σ_{-1} (right) as functions of T and μ. The units for $\Sigma_{\pm 1}$ are arbitrary. Here we use parameter set C.

mass leads to a larger thermal gluon mass, see Fig. 7.6, which leads to a reduced strange quark mass. This shows how light and strange quarks are coupled in our truncation. The amount of flavour-mixing through this effect is, however, rather small. Additionally, chiral restoration effects in the quark-gluon vertex can be expected to have an important impact on the behaviour of the strange quark at and above the phase transition.

In Fig. 7.9, we show the dual condensates Σ_{+1} and Σ_{-1} at finite chemical potential. As already mentioned in Chapter 6, the condensate at finite chemical potential and boundary conditions $\varphi \notin \{0, \pi, 2\pi\}$ develops an imaginary part. This is the reason why Σ_{+1} and Σ_{-1} differ for $\mu > 0$. We observe that $\Sigma_{-1} > \Sigma_{+1}$ for $\mu > 0$. However, the transition temperature is similar for both. We also note that the phase transition is more pronounced in Σ_{-1}, which motivates to use it to define the deconfinement transition temperature. This we will do in the phase diagram below. In contrast to
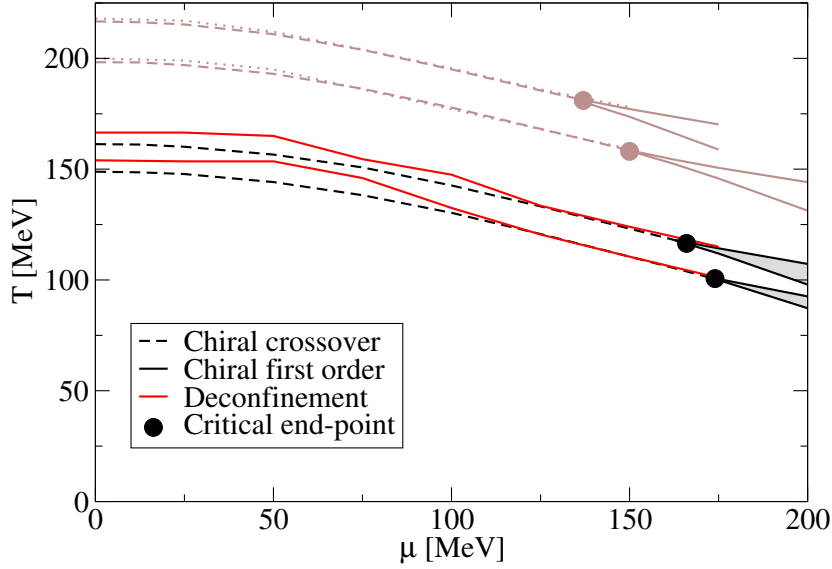
Figure 7.10: The phase diagram for $N_f = 2+1$. The upper lines (larger T) are obtained from parameter set B, the lower lines from parameter set A. In the lighter colours we repeat the results from $N_f = 2$. In all cases, the deconfinement transition is determined from Σ_{-1}.

the quark condensate, we do not observe a clear jump in $\Sigma_{\pm 1}$ at chemical potentials beyond the CEP. The nature of the deconfinement phase transition in this area remains unclear, and could be consistent with a crossover or second order transition. This is mainly due to the elaborate numerics in this region, which makes a finer resolution around T_c cumbersome.

7.6.2 Phase diagram for $N_f = 2 + 1$

From the order parameters that we discussed above, we obtain the phase diagram shown in Fig. 7.10.

We also compare to the $N_f = 2$ results from Fig. 7.5, in order to understand the influence of the strange quark. The main effect is evidently a reduction of the critical temperatures by about 50 MeV, which can be explained by the stronger suppression of the gluon due to the additional quark. The critical end-point moves to slightly larger chemical potentials. This is the known effect of fermionic fluctuations on the CEP, which is rather small here due to the large suppression by the strange quark mass. For parameter set A we find the CEP at $(\mu_{CEP}, T_{CEP}) \approx (174 \text{ MeV}, 101 \text{ MeV})$, such that $\mu_{CEP}/T_{CEP} \approx 1.76$. For parameter set B we find $(\mu_{CEP}, T_{CEP}) \approx (166 \text{ MeV}, 117 \text{ MeV})$, $\mu_{CEP}/T_{CEP} \approx 1.42$. Similar to the $N_f = 2$ case, the CEP in set B is at smaller μ due to the smaller quark mass.

The deconfinement transition shows the same qualitative behaviour as in the $N_f = 2$

case. The strange quark leads to stronger centre symmetry breaking, and thus a weaker crossover. As a consequence, the difference between the critical temperatures for the chiral and deconfinement transitions at small density is a few MeV larger than in the $N_f = 2$ case. For chemical potentials between $25 - 75$ MeV, we find a larger splitting between the chiral and deconfinement pseudo-critical temperatures compared to $\mu = 0$. This effect was already present for two flavours as well as for the HTL approximation, but is more pronounced when strange quarks are taken into account.

In Fig. 7.10, we determine the deconfinement temperature only from Σ_{-1}. This is due to a large numerical error in the determination of the derivative of Σ_{+1}, see the discussion around Fig. 7.9 and appendix B.3 for details. The numerical uncertainties affects only the mid-density area, *i.e.* $\mu \approx 25 - 100$ MeV, where also the effect of a stronger splitting between deconfinement and chiral restoration is observed. At larger chemical potentials we find coinciding phase transitions from the quark condensate, the dressed Polyakov loop and its conjugate.

7.7 Curvature of the critical line

Lattice QCD at large densities is hindered by the fermion sign problem. Nonetheless, it is possible to obtain the curvature of the phase transition line at zero chemical potential, which serves as an important comparison.

We can use a Taylor expansion of $T_c(\mu)$ around $\mu = 0$. The odd terms vanish due to the $\mu \leftrightarrow -\mu$ symmetry, and we find

$$T_c(\mu) = T_c(0) \left[1 - \kappa \left(\frac{\mu}{T_c(0)} \right)^2 + \mathcal{O} \left(\frac{\mu^4}{T_c^4(0)} \right) \right], \qquad (7.16)$$

where κ is the curvature. Different lattice collaborations agree on a value of $\kappa \approx 0.059$ for $N_f = 2 + 1$, see [103] and [113]. For $N_f = 2$, κ seems to be smaller with $\kappa \approx 0.051(3)$ reported in [114]. The increase of the curvature, when more flavours are taken into account, is in line with large-N_c arguments [115].

In order to extract κ, we fit Eq. (7.16) to our result for the chiral $T_c(\mu)$ on the interval $\mu \in [0, 25]$ MeV. For the HTL-like approximation we use $\mu \in [0, 50]$ MeV. For these intervals the μ^4-term is negligible. We summarise our findings in table 7.2, where we also repeat the results for T_c and the position of the CEP. We find that in all our calculations, κ is much larger than in the corresponding lattice results. For $2 + 1$ flavours we find $\kappa \approx 0.28$ with realistic quark masses, which is almost a factor 5 larger than the value extracted from lattice studies. In this regard, we agree with the quark-meson model and its Polyakov-loop extended version [19, 116]. In [116] it has been argued that a part of the discrepancy might be due to volume effects in the lattice calculations. On the other side, the inclusion of effects from the $U_A(1)$ anomaly might lead to a smaller κ in model studies, see [117]. In the present work such effects are not included. A possible way of including anomaly effects might be along the reasoning

	N_f	$T_c(\mu = 0)$	CEP	κ
HTL	2	183	(280,90)	0.23
Set A	2	198	(150,158)	0.41
	2+1	149	(174,101)	0.28
Set B	2	217	(137,181)	0.50
	2+1	161	(166,117)	0.31
Set C	2	202	(171,154)	0.41
	2+1	156	(190,100)	0.30

Table 7.2: Summary for the critical temperature, the location of the CEP and the curvature κ. Temperature and chemical potential are given in MeV.

of [118]. Note also that there is some ambiguity in the determination of κ, since the chiral transition is a crossover around $\mu = 0$. For the definition of T_c, we used the chiral susceptibility here. If we use the maximum of the temperature-derivative of the chiral condensate, the pseudo-critical temperature in the crossover region is smaller ($T_c(0) \approx 142.9$ MeV) while it is unchanged at the CEP. The curvature must therefore be smaller, and indeed we find $\kappa \approx 0.23$ for $N_f = 2 + 1$ with parameter set A, *cf.* $\kappa \approx 0.28$ from the susceptibility. In [103], T_c has been defined from the inflection point of the condensate, therefore we find that a part of the disagreement comes from the different definitions of T_c. However, $\kappa \approx 0.23$ is still almost a factor of 4 too large.

It is interesting that the improved truncation leads to a larger value for κ compared to the HTL-like approximation. We also fail to reproduce the N_f-dependence of κ. In our results κ decreases when strange quarks are included, in contrast to what we discussed above. This might be due to the influence of Goldstone bosons on the phase transition line. We will study this possibility in chapter 9.

The different parameter sets lead to comparable results for κ, especially for $N_f = 2 + 1$. We also find that κ grows monotonically with $T_c(0)$.

7.8 Dressing and Schwinger functions

7.8.1 T and μ dependence of the IR dressing functions

We now take a step back and investigate the dressing functions themselves. We will concentrate on the infrared, since there the medium effects are most pronounced.

To this end we have a look at the real and imaginary parts of the dressing functions, evaluated at $\vec{p}^2 = 0$ and $\omega_p = \pi T$. As an abbreviation we use $F(0) = F(\vec{p}^2 = 0, \pi T)$ for a dressing function $F \in \{A, B, C\}$. The real part of B, *i.e.* Re$B(0)$ shows the typical behaviour of an order parameter of chiral symmetry, just like the chiral condensate that we discussed in Fig. 7.8. In the left part of Fig. 7.11 we show Im$B(0)$. At $\mu = 0$ quarks and antiquarks are symmetrical, thus Im$B(0) = 0$. With growing chemical potential, the difference between quarks and antiquarks grows, which is reflected in a
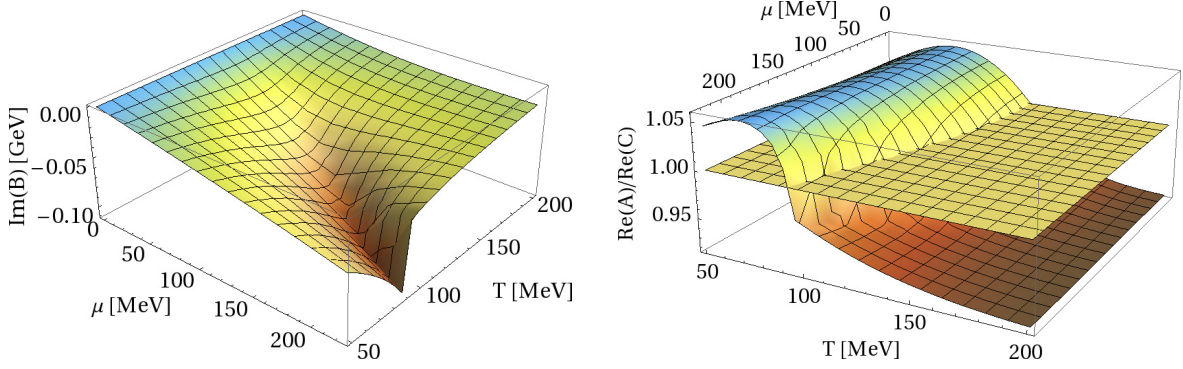
Figure 7.11: The left figure shows $\mathrm{Im}B(0)$, the right figure $\mathrm{Re}A(0)/\mathrm{Re}C(0)$, evaluated at $\vec{p}^2 = 0$, $\omega_p = \pi T$. Here we used parameter set C.

growing $\mathrm{Im}B(0)$. Interestingly, its absolute value is maximal close to the chiral phase transition. In the right part of Fig. 7.11 we show $\mathrm{Re}A(0)/\mathrm{Re}C(0)$. In [77], it was argued that, if A and C were constant, $\sqrt{A/C}$ could be interpreted as the velocity v of a quasi-particle. Thus, in the deconfined region one expects $A/C < 1$. Below T_c, this relation does not hold, and a quasi-particle picture for quarks can not be applied. This scenario seems to hold for all μ. The reversing order of $A(0)$ and $C(0)$ might therefore be connected to the deconfinement transition.

7.8.2 Schwinger function

In section 3.2.4, we discussed a different notion of confinement, the violation of Osterwalder-Schrader axioms for physical particles. To study this at finite temperature we follow [78]. The quark spectral function $\rho(\vec{p}, \omega)$ is defined implicitly by

$$S(\vec{p}, \omega_n) = \int\limits_{-\infty}^{\infty} \frac{d\omega}{2\pi} \frac{\rho(\vec{p}, \omega)}{\mathrm{i}\omega_n - \omega}, \tag{7.17}$$

where we can use the decomposition

$$\rho(\vec{p}, \omega) = -\mathrm{i}\frac{\vec{\not{p}}}{|\vec{p}|}\rho_v(\vec{p}, \omega) + \gamma_4 \rho_4(\vec{p}, \omega) + \rho_s(\vec{p}, \omega). \tag{7.18}$$

We will restrict ourselves to the $\vec{p} = 0$ case, where we define the projectors

$$P_\pm = \frac{1 \mp \gamma_4}{2}, \tag{7.19}$$

which project the quark onto positive and negative energy components.[1] This can be used to distinguish between quarks and antiquarks at finite chemical potential. We

---

[1] In [77,78] the $P_\pm$ defined in Eq. (7.19) have been labelled $L_\pm$.

can then decompose the quark propagator at vanishing spatial momentum as

$$S(\vec{0}, \omega_n) = (S_+(\omega_n)P_+ + S_-(\omega_n)P_-)\,\gamma_4, \tag{7.20}$$

where

$$S_\pm(\omega_n) = -\frac{\mathrm{i}\tilde{\omega}_n C(\vec{0}, \omega_n) \pm B(\vec{0}, \omega_n)}{\tilde{\omega}_n^2 C^2(\vec{0}, \omega_n) + B^2(\vec{0}, \omega_n)}. \tag{7.21}$$

We can define the spectral functions corresponding to $S_\pm$ as

$$\rho_\pm(\omega) = \rho_4(\vec{0}, \omega) \pm \rho_s(\vec{0}, \omega). \tag{7.22}$$

We will now study whether ρ_+ and ρ_- are positive for all ω. Ideally, one could extract $\rho_\pm$ directly from the quark propagator. This can be done by using the maximum-entropy method, for example. However, this is beyond the scope of this work, and we will use a different procedure instead. In [78] a connection between the Schwinger functions that correspond to $\rho_\pm$ and the positivity of $\rho_\pm$ was found. To this end, we define the Schwinger functions

$$S_\pm(\tau) = -T \sum_n e^{-\mathrm{i}\omega_n \tau} S_\pm(\omega_n). \tag{7.23}$$

In [76], the Schwinger function[2] in the vacuum was found to show an oscillating behaviour and to become negative for some values of τ. The first zero crossing was found at $\tau \approx 5.8$ fm. However, at finite temperature the Euclidean time direction becomes finite. A Euclidean time of 5.8 fm can only be accessed at $T \leq 34$ MeV. (Note that this zero crossing was obtained in a different truncation scheme, and might be different in our case.) We can thus expect to find zero crossings of the Schwinger functions only for rather small temperatures. We will therefore rely on an alternative, which only provides a necessary but no sufficient proof for positivity violations. In [78], it was found that

$$\rho_\pm(\omega) \geq 0 \quad \Rightarrow \quad \frac{\partial^2 \ln S_\pm(\tau)}{\partial \tau^2} \geq 0, \tag{7.24}$$

i.e. for a positive definite spectral function the second logarithmic derivative of the Schwinger function is positive definite. Conversely, for a Schwinger function with a negative second logarithmic derivative the spectral functions needs to violate positivity. We can use this as a necessary condition for positivity violation. It is not a sufficient condition, since if the Schwinger function does not fulfil Eq. (7.24), the spectral function might violate positivity nonetheless. That is, we can find a lower bound for the temperature at which the quark spectral function becomes positive definite.

We can turn this into an "order parameter" for positivity violation. We obtain $S_\pm$ from Eq. (7.23) and evaluate the second logarithmic derivative numerically. The amount of Euclidean time where positivity is violated can than be defined as

$$L_\pm = \mu\left(\left\{\tau T \in [0,1] : \partial^2 \ln S_\pm(\tau)/\partial \tau^2 < 0\right\}\right), \tag{7.25}$$

---

[2]In [76] the Schwinger function was defined from the scalar part only, *i.e.* Eq. (7.21) without the C-term in the numerator.

where $\mu(A)$ is the Borel measure of the set A. If $L_\pm > 0$ we find positivity violations, while for $L_\pm = 0$ the quark spectral function $\rho_\pm$ might be positive definite.

7.8.3 Results for $\mu = 0$ with $N_f = 2 + 1$

Let us first investigate the case of vanishing density. For the quenched case, this was discussed in [77], and we can apply these ideas to the unquenched case. We will use our truncation scheme with $2 + 1$ flavours, and we will study the Schwinger function of the light quark.
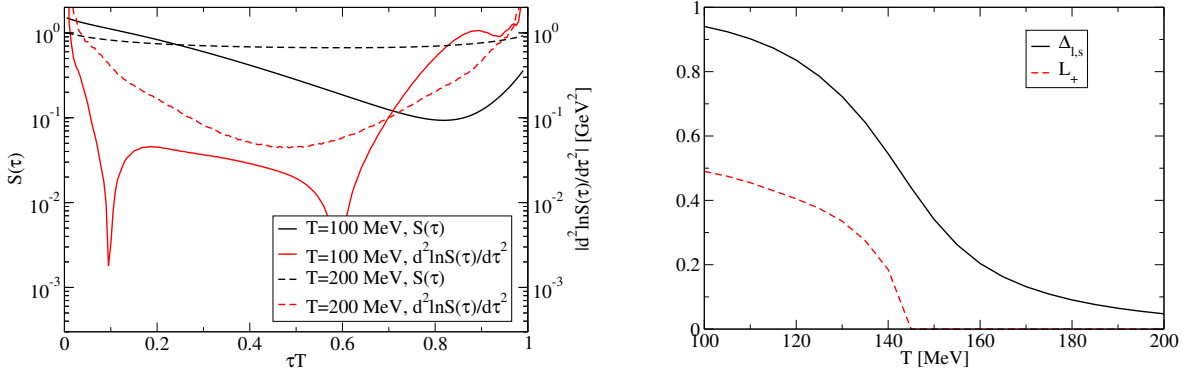

Figure 7.12: Parameter set A with $\mu = 0$ and $N_f = 2 + 1$. Left figure: the Schwinger function and the absolute value of its second logarithmic derivative for $T = 100$ and 200 MeV. Right figure: "order parameter" L_+ as a function of T, together with the finite condensate $\Delta_{l,s}$ as a comparison.

In Fig. 7.12 we show the Schwinger function S_+, its second logarithmic derivative and the "order parameter" L_+ for $\mu = 0$. Here, $S_+(\tau) = S_-(1/T - \tau)$ since quarks and anti-quarks are completely symmetric at vanishing density. In the left figure we compare the situation below and above T_c. At $T = 100$ MeV the Schwinger function is strictly positive, but its second logarithmic derivative is negative over a large range of τ. The negative curvature of S_+ is also visible to the plain eye on the logarithmic plot. This changes for $T = 200$ MeV, where $\partial^2 \ln S_\pm(\tau)/\partial\tau^2 > 0$ for all τ. Thus, we can not find evidence for a violation of positivity, although we would like to stress again that our criterion can not rule it out. The Schwinger function of the strange quark shows positivity violations at temperatures up to $T \approx 220$ MeV. This is connected to the higher chiral restoration temperature for the strange quark.

From L_+, which we show on the right hand side of Fig. 7.12, we can determine the amount of positivity violations as a function of temperature. Clearly, L_+ is reduced with increasing temperature and vanishes at $T = 142.5 \pm 2.5$ MeV. This is very close to the chiral $T_c \approx 149$ MeV (142.9 MeV), determined from the susceptibility (inflection point). This suggests that for $\mu = 0$ the quark changes nature at T_c, and turns from an unphysical particle to one that might be physical in the sense of the Osterwalder-

Schrader axioms. These results are similar to the quenched studies in [77], and the rainbow-ladder studies in [119] We also agree with results from the maximum-entropy method that have been presented in [80]. There, it was found that the spectral function is positive definite above T_c.

7.8.4 Results at finite density

Let us now turn to finite chemical potential. There, quarks and antiquarks are no longer equal. This results in different Schwinger functions $S_+(\tau)$ and $S_-(\tau)$, which also implies that in general $L_+ \neq L_-$.
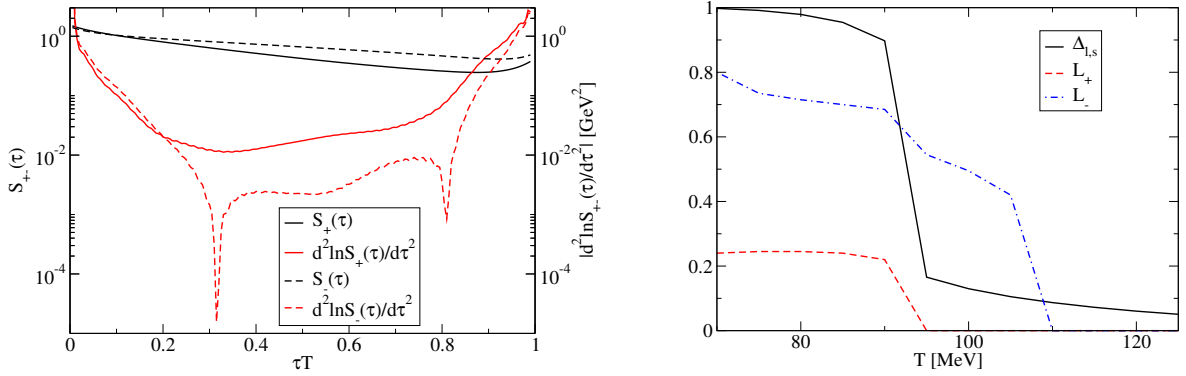

Figure 7.13: Parameter set A with $\mu = 200$ MeV and $N_f = 2+1$. The left figure shows the Schwinger functions S_+ and S_- together with their second logarithmic derivative at $T = 100$ MeV. The right figure shows the condensate and the "order parameters" $L_\pm$ as functions of the temperature.

In the right part of Fig. 7.13, we show L_+ and L_- at $\mu = 200$ MeV and $N_f = 2+1$. This is already in the first order region, with $T_c \approx 93$ MeV, see Fig. 7.10. We find that the possible restoration of reflection positivity coincides with the chiral restoration for S_+ within the numerical precision. However, L_- becomes zero about 15 MeV above the chiral transition. This is a new feature of the Schwinger functions at finite chemical potential and with strange quarks taken into account. We show $S_\pm$ in the region where chiral symmetry is already restored but positivity still violated by S_- in the left part of Fig. 7.13. It is clear that the area where $d^2 \ln(S_-(\tau))/d\tau^2$ is negative is too large to be explained by numerical artefacts.

In Fig. 7.14 we show the phase diagrams for 2 and $2+1$ flavours together with the "deconfinement" temperatures extracted from the point where $L_\pm = 0$. For two flavours the effect described above, *i.e.* the persistence of positivity violations above T_c, is absent. Although L_+ and L_- become zero at slightly different temperatures, this always happens near the chiral restoration temperature, and coincides in the first-order region. For $N_f = 2+1$ this changes. At chemical potentials above 100 MeV clearly an area develops where $L_- > 0$, but chiral symmetry is already restored.
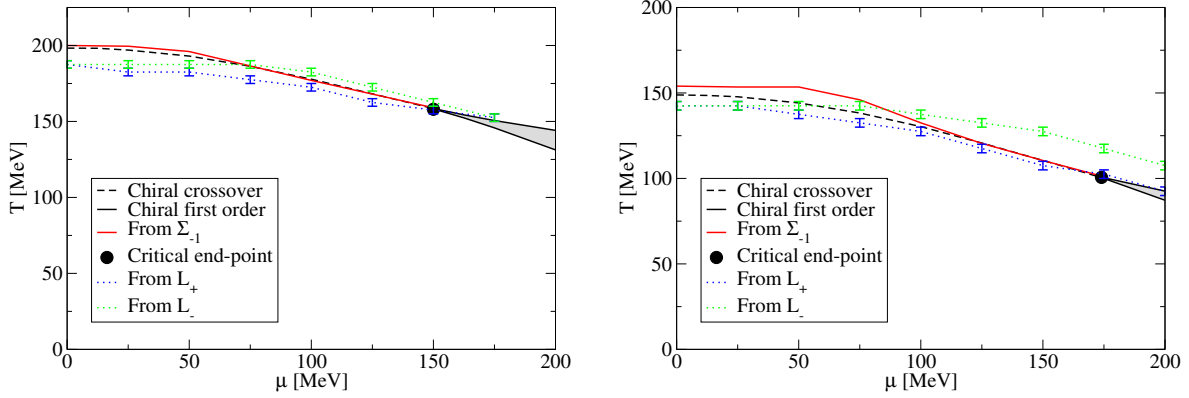
Figure 7.14: The phase diagrams for $N_f = 2$ (left figure) and $N_f = 2 + 1$ (right figure). The temperatures where L_+ and L_- become zero are denoted by the blue and green lines. Again, parameter set A was used.

The origin of this behaviour has to be studied in more detail in future work by obtaining the spectral function directly. From the dual condensate and also the Polyakov-loop potential (see next chapter) we always find near-by transitions for deconfinement and chiral restoration, the behaviour of S_- with $N_f = 2 + 1$ is the only hint so far for a splitting of these transitions.

7.9 Summary

In this chapter, we proposed a novel truncation scheme for the coupled system of unquenched quark and gluon propagators. This is the main progress achieved in this work. We solved the problem of the quadratic divergence in the quark loop at finite temperature, by using a generalisation of the Brown-Pennington projector for finite temperature. With this, we were able to successfully compare the resulting unquenched gluon propagator to recent lattice results of the same object. The agreement is not only qualitatively, but also quantitatively on a good level. From the quark loop we extracted the Debye screening mass, which shows a strong reaction on the chiral phase transition. This can not be captured by the HTL-like approximation that we used in the last chapter. Dressing the quark loop leads to a suppression of the fermionic fluctuations, and thus a CEP at smaller μ than with bare quarks in the loop. This is an important result from our study and suggests that studies in effective models have to treat fermionic fluctuations with great care.

With the gluon being sensitive to the quark sector, we were able to couple light and strange quarks and obtained the first $N_f = 2 + 1$ phase diagram from Dyson-Schwinger equations. At zero density we found that our model can reproduce the condensate obtained on the lattice to a very good accuracy. The effect of the strange quark was found to be mainly a reduction of T_c. At finite density, the critical end-point was found

at a chemical potential about $20 - 30$ MeV larger than without strange quarks.

We determined the deconfinement transition temperature from the dressed Polyakov loop, and found it to be near-by the chiral restoration temperature for $N_f = 2$ and $N_f = 2 + 1$. This is in qualitative agreement with the HTL-like approximation. The difference of the chiral and deconfinement transition temperatures was found to be much smaller than in the HTL-like case, which we can attribute to the sensitivity of the gluon to the chiral dynamics in the fully coupled truncation. However, when strange quarks are taken into account, this difference becomes larger due to the stronger explicit breaking of centre symmetry. At medium chemical potentials we found a larger difference of the transition temperatures than at zero chemical potential. The reason for this behaviour is not well understood yet, and might be an artefact.

As a further test of our model, we compared the curvature of the phase boundary at $\mu = 0$ with lattice results. We found that, similarly to studies in effective models, the curvature is much larger than that obtained on the lattice. We also found a wrong ordering with the number of flavours. While on the lattice $2 + 1$ flavours lead to a larger curvature, in our truncation the curvature was found to decrease. This certainly requires an improvement of our truncation scheme.

We finally gave an outlook on the quark spectral functions and the violation of positivity therein. We found the quark to have a positivity violating spectral function at least up to T_c. At finite density the (possible) restoration of positivity was found to always be near the chiral transition temperatures in the two-flavour case. For $2 + 1$ flavours, however, a small gap was found at large densities where positivity seems to be violated although chiral symmetry is already approximately restored.

Given the success of our truncation to obtain an unquenched gluon propagator in agreement with lattice results, we have a good starting point for further studies of thermal QCD. We will exploit this in the next chapter to obtain the Polyakov-loop potential from the propagators.

8 Polyakov-loop potential

In the last chapters, we used the dual condensate as an order parameter for confinement. This object is sensitive to centre symmetry and reduces to the ordinary Polyakov loop for large quark masses. The main reason to use this observable is that it is unknown how to calculate the ordinary Polyakov loop from correlation functions. Quite recently, a new method to obtain an observable that is closely related to the Polyakov loop has been developed in [72–74]. The idea is to use the background-field method to introduce a constant A_4 gauge field. From this, the Polyakov-loop potential can be deduced, and by finding its minimum we get an upper bound for the Polyakov loop. This procedure has been used for Yang-Mills theory in [72, 73, 120] and for QCD at imaginary chemical potential in [32]. In [72], an integrated version of the flow equation with neglected RG improvement terms has been used. Using this approximation, it was possible to connect the infrared behaviour of the Yang-Mills Green's functions with a vanishing Polyakov loop at small temperatures. In [121], the same *ansatz* has been used in a study to describe the quenched phase transition as well as an input to a chiral model. Going beyond this approximation, in [74], besides a full FRG and a 2PI calculation, the DSE for the background-field has been used to derive the Polyakov-loop potential. We will follow this work in this chapter.

With the Polyakov-loop potential, we can access a second order parameter for centre symmetry, which can be compared to the results from the dual condensate. This will help to clarify how strong the behaviour of the deconfinement line at finite μ, that we found in the last chapter, is affected by artefacts of the dual condensate. This is especially interesting for the larger splitting of chiral and deconfinement temperatures around $\mu = 50 - 75$ MeV that we found, and which was most pronounced in our $N_f = 2 + 1$ calculation.

Furthermore, the Polyakov-loop potential serves as an input in Polyakov-loop extended effective field theories, like the PQM and PNJL models. In these models, the philosophy is to replace the coupling of quarks to gluon fields by a background field that can be associated with a Polyakov loop variable. To this end, the Lagrangian takes the form

$$\mathcal{L}_{P-model} = \bar{q} \left(-\gamma_\mu (\partial_\mu + \mathrm{i}g\bar{A}_\mu) \right) q + \mathcal{U}(\Phi[\bar{A}], \bar{\Phi}[\bar{A}]) + \dots, \tag{8.1}$$

where $\bar{A}$ is the background field from which the Polyakov-loop and its conjugate, Φ and $\bar{\Phi}$, can be obtained. The Polyakov-loop potential is $\mathcal{U}$, a model input that is usually fitted to thermodynamic observables from quenched lattice QCD, see e.g. [22]. In this procedure one usually neglects fermionic contributions in the Yang-Mills sector. When

the Polyakov-loop potential is determined from the QCD Green's functions, this is equivalent to taking the quenched ghost and gluon propagators as input. In [25], fermionic fluctuations were included via scale changes determined from the perturbative running of the QCD coupling. It was found that these contributions are important especially at large μ, where a closer connection between chiral restoration and the deconfinement transition was found. With our results of the non-perturbatively unquenched gluon propagator, we can access the Polyakov-loop potential at zero and finite chemical potential. This serves as a cross-check for model assumptions about this potential. The results of this chapter have been published in [122].

8.1 Background-field method

We will firstly review the basic ideas presented in [72, 74]. We begin with adding a constant field $\bar{A}_\mu$ to the fluctuating field a_μ

$$A_\mu = a_\mu + \bar{A}_\mu, \tag{8.2}$$

such that $\langle A_\mu \rangle = \bar{A}_\mu$. With the covariant derivative $D_\mu(A) = \partial_\mu + igA_\mu$, we can define the Landau-de Witt gauge

$$\bar{D}_\mu a_\mu = 0, \tag{8.3}$$

which is an extension of Landau gauge. As an abbreviation we write $\bar{D}_\mu = D_\mu(\bar{A})$. This leads to a modification of the gauge fixed Lagrangian, Eq. (2.5), according to

$$\frac{1}{2\xi}\text{Tr}_c\partial_\mu A_\mu\partial_\nu A_\nu + i\bar{c}\partial_\mu D_\mu c \quad \rightarrow \quad \frac{1}{2\xi}\text{Tr}_c\bar{D}_\mu a_\mu\bar{D}_\nu a_\nu + i\bar{c}\bar{D}_\mu D_\mu c. \tag{8.4}$$

The bare propagators and vertices change accordingly. See also [123] for details on the background-field formalism.

With the background field we can find an order parameter for confinement. We can define the Polyakov loop as

$$L[A_4] = \frac{1}{N_c}\text{Tr}\mathcal{P}e^{i\int d\tau gA_4(\vec{x},\tau)}, \tag{8.5}$$

where A_4 is in the fundamental representation, see also section 3.2.1. If we evaluate the Polyakov loop for the background-field $\bar{A}_4$ instead of the full fluctuating field we find, due to the Jensen inequality [72],

$$L[\langle A_4 \rangle] \geq \langle L[A_4] \rangle. \tag{8.6}$$

Here $\langle L[A_4] \rangle$ is the expectation value of the Polyakov loop which is usually taken as the order parameter for confinement. Eq. (8.6) implies that if $L[\langle A_4 \rangle] = 0$, also $\langle L[A_4] \rangle = 0$. It can also be shown, that in the centre-symmetric phase, $L[\langle A_4 \rangle] = 0$ [73] and we therefore can use $L[\langle A_4 \rangle]$ as an order parameter for confinement as well. However, $L[\langle A_4 \rangle]$ serves only as an upper bound for $\langle L[A_4] \rangle$, and we can expect an underestimation of the (pseudo-)critical temperatures.

8.2 DSE for the background field

In [74], the DSE for the background field has been derived. To this end, we take the master DSE, Eq. (2.17), and apply it to $\bar{A}_4$. This yields

$$\frac{\delta\Gamma[\Phi]}{\delta\bar{A}_4} = \frac{\delta S[\Phi]}{\delta\bar{A}_4} + \frac{1}{2}S^{(3)}_{\bar{A}_4 aa}G_a - \frac{1}{6}S^{(4)}_{\bar{A}_4 aaa}G_a^3\Gamma^{(3)}_{aaa} - S^{(3)}_{\bar{A}_4 c\bar{c}}G_c + S^{(4)}_{\bar{A}_4 a\bar{c}c}G_c^2 G_a\Gamma^{(3)}_{ac\bar{c}} - S^{(3)}_{\bar{A}_4\psi\bar{\psi}}G_\psi, \tag{8.7}$$

where we adopt the notation from [74], e.g. $S^{(3)}_{\bar{A}_4 aa} = Z_3\frac{\delta^3 S}{\delta\bar{A}_4\delta a\delta a}$ defines the bare vertex of the background field and two gluon propagators. The propagators for gluon, ghost and quark fields are denoted by G_a, G_c and G_ψ, respectively. Eq. (8.7) is shown diagrammatically in Fig. (8.1). It involves one- and two-loop diagrams. Note that the second two-loop diagram, involving a four-point function that connects two ghost fields with the background and a gluon field, only appears in the presence of the background field. The quark loop is shown for one flavour only.
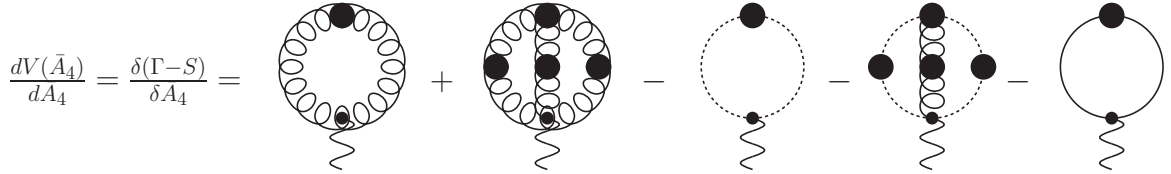
$$\frac{dV(\bar{A}_4)}{d\bar{A}_4} = \frac{\delta(\Gamma - S)}{\delta A_4} =$$

Figure 8.1: The DSE for the background field $\bar{A}$. It is denoted by the wavy line on the bottom, in contrast to the gluon which is represented by the curly line.

We will discard the two-loop diagrams for the sake of simplicity here. This is justified on two grounds. Firstly, we follow the argument of [74], where the renormalisation scheme was chosen such that the two-loop terms are minimised near T_c. Secondly, we shall concentrate on the influence of quarks on the Polyakov-loop potential. As we will see, the quark loop dominates the phase transition in unquenched QCD and the glue part serves more as a confining background, even with the unquenched gluon propagator.

If we neglect the two-loop diagrams, Eq. (8.7) defines $\frac{dV(\bar{A}_4)}{d\bar{A}_4}$ solely in terms of the gluon, ghost and quark propagators, since the vertices are bare. In [74], the vertices $S^{(3)}_{\bar{A}_4 aa}$ and $S^{(3)}_{\bar{A}_4 c\bar{c}}$ have been given as

$$S^{(3)}_{\bar{A}_\rho a_\mu a_\nu} = S^{(3)}_{a_\rho a_\mu a_\nu} + \frac{1}{\xi}\frac{\delta\left(\bar{D}_\mu\bar{D}_\nu\right)}{\delta A_\rho}, \tag{8.8}$$

$$S^{(3)}_{\bar{A}_\rho c\bar{c}} = 2S^{(3)}_{a_\rho c\bar{c}}, \tag{8.9}$$

with the gauge parameter ξ. Eq. (8.9) is evaluated at vanishing momentum of the background field. See also [123] for Feynman rules in the background field method. The last term in Eq. (8.8) contributes to the final expression despite $\xi \to 0$, since it

combines with the longitudinal part $\propto \xi$ of the gluon propagator. We give some details on this evaluation and the vertices for vanishing background field $S^{(3)}_{a_\rho a_\mu a_\nu}$ and $S^{(3)}_{a_\rho c \bar{c}}$ in App. C.1. For the quark fields we find the vertex

$$S^{(3)}_{\bar{A}_\mu \psi \bar{\psi}} = \mathrm{i} g \gamma_\mu. \tag{8.10}$$

The colour structure of the quark loop is detailed in App. C.2. With the vertices and the propagators in presence of the background field, we can solve Eq. (8.7). By numerical integration we can then access the potential $V(\bar{A}_4)$ up to an integration constant. What remains is to define the propagators in the presence of the background field.

8.3 Propagators in the background field

In chapter 7 we used the quark and gluon DSEs to obtain the quark and gluon propagators in Landau gauge for $N_f = 2$ and $N_f = 2 + 1$. The ghost propagator did not play a role so far, and we need to specify it now.
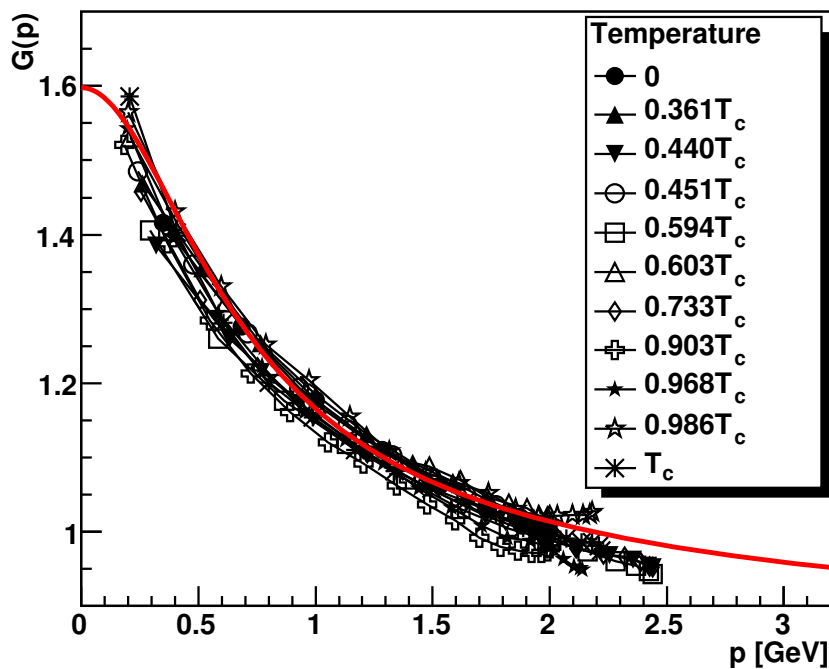

Figure 8.2: The quenched lattice ghost below $T_c^{qu.} = 277$ MeV, together with our fit, represented by the red line. Figure (without our fit) taken from [42].

For the quenched ghost, we can use the lattice results from [42], which correspond to the quenched gluon input in our calculations. Fig. 8.2 shows the propagator for temperatures below the quenched phase transition. This is the only temperature interval

needed in this study. The ghost shows little dependence on the temperature, which can be explained to some degree by the ghost DSE. If one assumes a bare ghost-gluon vertex, an assumption often made in studies of the DSEs for the Yang-Mills system, the ghost is determined in the IR from the transversal gluon propagator. In contrast to the longitudinal gluon, the transversal gluon depends only weakly on the temperature.

This justifies to use a temperature-independent fit for the quenched ghost. We model the fit function with a logarithmic tail in the UV, and a finite IR enhancement. Note that this corresponds to the decoupling solution of the Yang-Mills system. This is also implemented in the gluon propagator, see the discussion in chapter 5. The fit function reads

$$G(p^2) = \frac{a}{bp^2 + 1} + \left(\frac{\beta_0 \alpha_\mu}{4\pi} \log(\hat{p}^2 + 0.1) + 1 \right)^\delta, \tag{8.11}$$

where for the parameters in the IR we find $a = 0.42$ and $b = 2.5 \text{ GeV}^{-2}$. In the UV $\delta = -9/44$ is the anomalous dimension of the ghost, and we choose $\hat{p}^2 = p^2/\Lambda^2$ with $\Lambda = 2$ GeV. The resulting fit function is shown in Fig. 8.2 together with the lattice data.

The ghost propagator is only indirectly affected by the unquenching process. In lattice simulations of quenched [94] and $N_f = 2$ unquenched [112] QCD, the ghost has been found to be almost unchanged. This supports our approximation of taking the quenched ghost as an input also in the $N_f > 0$ case. From the ghost DSE, see Fig. 5.2, we expect the ghost dressing function to be reduced for a reduced gluon propagator. Since the ghost in the picture of the Polyakov-loop potential is confining, we expect an unquenched ghost to lead to weaker confinement, or a larger Polyakov loop.

So far, all propagators have been obtained in Landau gauge. However, we now need the propagators in Landau-de Witt gauge, *i.e.* in the presence of a constant background-field. We will approximate the propagators in the background field by the Landau gauge propagators, by using

$$D(\bar{A}_4; \omega_n, \vec{p}^2) = D(0; \omega_n + g\bar{A}_4, \vec{p}^2), \tag{8.12}$$

where D is any propagator of QCD. This approximation has been justified in [74].

We take $\bar{A}_4$ to be in the Cartan sub-algebra of $SU(3)$. For practical purposes, we take $\bar{A}_4 = \bar{A}_4^3 T^3$ where T^3 is a generator of $SU(3)$. We evaluate the propagators for the matrix-valued argument $\omega_p + g\bar{A}_4$ by evaluating them on the eigenvalues. The gluon and ghost propagators belong to the adjoint, quarks to the fundamental representation of $SU(N_c)$. The corresponding eigenvalues of $\omega_p + g\bar{A}_4$ for the $N_c = 3$ case are

$$ev_{adj.} = \{\omega_p, \omega_p, \omega_p \pm \pi T\varphi, \omega_p \pm \pi T\varphi, \omega_p \pm 2\pi T\varphi\}, \tag{8.13}$$

$$ev_{fund.} = \{\omega_p, \omega_p \pm \pi T\varphi\}. \tag{8.14}$$

Here, we introduced the scalar φ as a measure for the background-field. Evidently, the eigenvalues are periodic in φ, and we can constrain $\varphi \in [0, 1]$. A function f therefore becomes

$$f(\omega_n + g\bar{A}_4) = \sum_{x \in ev} f(x), \tag{8.15}$$

with the eigenvalues ev of either the adjoint or the fundamental representation. With this decomposition, we can obtain $L[\langle A_4 \rangle]$ as a function of φ. To this end, we obtain Eq. (8.5) for $\bar{A}_4$ in the fundamental representation, which yields

$$L(\varphi) = \frac{1 + 2\cos(\pi\varphi)}{3}. \tag{8.16}$$

For $\varphi = \frac{2}{3}$ the Polyakov loop vanishes, and we are in the confined phase. Deconfinement then means that a $\varphi < \frac{2}{3}$ is realised.

8.4 Numerical evaluation

Let us first start with the glue part of the Polyakov-loop potential. We evaluate Eq. (8.7) without the two-loop diagrams and with the vertices in Eqs. (8.8,8.9). We then apply the eigenmode decomposition from Eq. (8.15). One part of the sum can then be written as

$$\frac{dV_{glue}(\varphi)}{d\varphi} = \sum_l \!\!\!\!\!\!\!\!\int \omega_l^\varphi \left(\frac{1}{l^2} + Z_3 D_L(l) + 2Z_3 D_T(l) - 2\tilde{Z}_3 D_G(l) \right), \tag{8.17}$$

where $\omega_l^\varphi = 2\pi T(n + \varphi)$. The propagators are $D_{L,T}(l^2) = \frac{Z_{L,T}(l^2)}{l^2}$ for the gluon and $D_G(l^2) = \frac{G(l^2)}{l^2}$ for the ghost propagator. They are evaluated at $l = (\vec{l}, \omega_l^\varphi)$. The first term comes from the polarisation longitudinal to the gluon momentum, see also App. C.1. It does not receive a dressing in Landau gauge, and is the derivative of the Weiss potential [124].

For the quark loop, we take the vertex Eq. (8.10). For a quark of flavour f we then find

$$\frac{dV_q^f(\varphi)}{d\varphi} = \sum_l \!\!\!\!\!\!\!\!\int \text{Tr}_D[\mathrm{i}\gamma_4 S^f] = 4 \sum_l \!\!\!\!\!\!\!\!\int \frac{\tilde{\omega}_l^\varphi C^f(l)}{(\tilde{\omega}_l^\varphi C^f(l))^2 + \vec{l}^2 \left(A^f(l)\right)^2 + \left(B^f(l)\right)^2}, \tag{8.18}$$

with $\tilde{\omega}_l^\varphi = 2\pi T(n + \frac{1}{2} + \varphi) + \mathrm{i}\mu_f$ where $\mu_{u/d} = \mu$ and $\mu_s = 0$. Eqs. (8.17,8.18) can be integrated numerically with respect to φ, neglecting an integration constant. The full Polyakov-loop potential is then obtained from

$$V(\bar{A}_4) = 2V_{glue}(\varphi) + 4V_{glue}\left(\frac{\varphi}{2}\right) - 4\sum_f^{N_f} \left[V_q^f\left(\frac{\varphi}{2}\right) + V_q^f\left(-\frac{\varphi}{2}\right) \right], \tag{8.19}$$

where we used that $V_{glue}(-\varphi) = V_{glue}(\varphi)$. At finite μ, V_q becomes complex. However, the imaginary parts of $V_q(\varphi/2)$ and $V_q(-\varphi/2)$ cancel, giving a real potential.

8.5 Results

In this section we will use our truncation scheme for $N_f = 2 + 1$ with parameter set A. We obtain the unquenched quark and gluon propagators from their Dyson-Schwinger equations and use those results as an input in Eqs. (8.17,8.18).
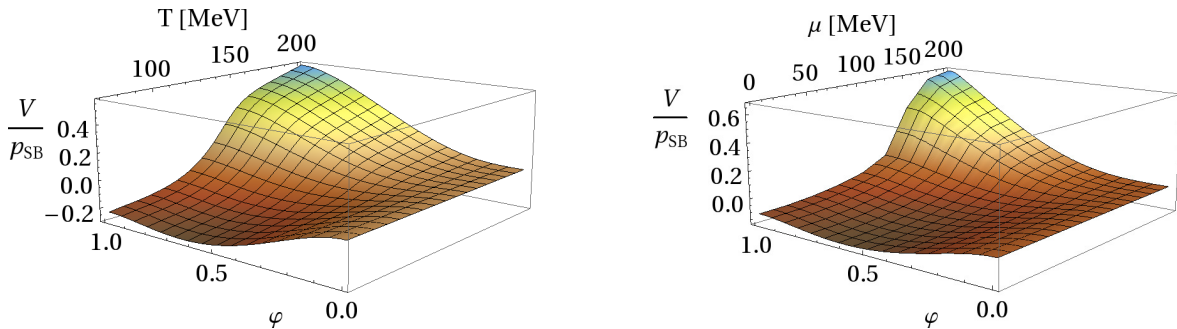

Figure 8.3: The left figure shows the Polyakov-loop potential at $\mu = 0$, the right figure as a function of μ at $T = 115$ MeV. We normalise by $p_{SB} = \frac{19\pi^2}{36}T^4 + \frac{3}{2}T^2\mu^2 + \frac{3}{4\pi^2}\mu^4$.

The resulting Polyakov-loop potential as a function of temperature at $\mu = 0$ is shown in the left part of Fig. 8.3. At small temperatures, the minimum of the potential is close to $\varphi = \frac{2}{3}$, which is the confining value where $L[\langle A_4 \rangle] = 0$. It is not exactly at the confining value due to the presence of centre-symmetry breaking quarks. When the temperature grows, the minimum of the potential moves further away from the confining value, and approaches $\varphi = 0$. This corresponds to $L[\langle A_4 \rangle] = 1$. A similar behaviour is found at finite chemical potential. In the right part of Fig. 8.3 we show the Polyakov-loop potential at fixed $T = 115$ MeV as a function of μ. Again, the minimum moves away from a position close to the confining value, and approaches $\varphi = 0$. We chose the temperature of 115 MeV close to, but above, the critical end-point. The more rapid change of the potential as a function of μ is therefore derived from the steeper chiral crossover. Note that the glue part of the potential is always negative (or zero), while the quark part is positive.[1] This explains the large positive value of the potential around $\varphi = 1$ in the chirally restored phase. There, the contribution of the quark loop is largest.

From the minimum of the potential we determine the Polyakov loop $L[\langle A_4 \rangle]$. The result is shown in Fig. 8.4. It is clear that the transition always happens in the same temperature regime where also the chiral transition takes place. This behaviour can be explained by the quark-loop diagram in Fig. 8.1. If we assume a bare quark of mass M, the integrand of the quark loop goes like $1/(l^2 + M^2)$, *i.e.* it is suppressed with the quark mass. In the chirally broken phase, where the quark mass is large, the quark loop has therefore little effect on the Polyakov-loop potential, which is thus dominated

---

[1]Strictly speaking, the difference $V(\varphi) - V(0)$ is positive/negative.
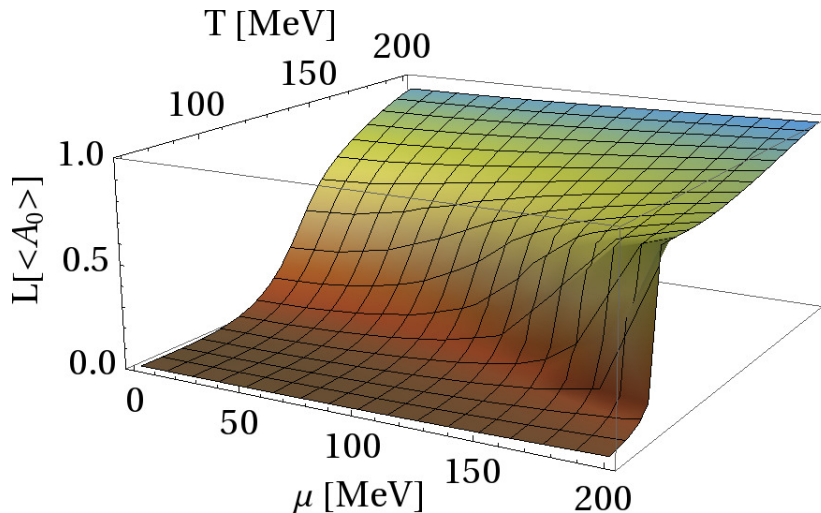
Figure 8.4: The order parameter $L[\langle A_4 \rangle]$ as a function of T and μ.

by the confining glue sector. It is noteworthy at this point that the unquenching of the gluon propagator does not change the strictly confining nature of the pure-glue Polyakov-loop potential. As the temperature approaches T_c, the quark mass is reduced. This leads to a growing contribution of the quark loop, which increases the amount of deconfinement in the potential. In the chirally symmetric phase we then find that the potential is dominated by the quark loop, and $L[\langle A_4 \rangle]$ approaches 1.

At finite chemical potential the effect is the same. We therefore can not find a splitting of chiral and deconfinement transitions in this approach. Once the chiral phase transition becomes first order, the quark mass shows a jump. This is reflected in a jump of the quark loop, and therefore also a jump in the Polyakov loop. This is clearly visible in Fig. 8.1.[2] This is a clear difference to the dressed Polyakov loop, see Fig. 7.9. There, the shape of $\Sigma_{\pm 1}$ was found to be consistent with a second order or crossover transition, while here we clearly find a first order phase transition. Another important difference to the dual condensates is that we can not distinguish between the Polyakov loop and its conjugate, which are in general different at finite chemical potential. For the dual condensates this distinction can be made by using Σ_{+1} and Σ_{-1}.

We now take the derivative of $L[\langle A_4 \rangle]$ with respect to T and determine its maximum. This we will use to define the pseudo-critical temperature of deconfinement. In Fig. 8.5 we show the resulting phase diagram and compare it to the chiral transition and the deconfinement transition obtained from the dressed Polyakov loop. It is important to note that we used the maximum of the T-derivative of the order parameters for all critical lines here. That is why the lines from the chiral and dual condensate are lower in the crossover region than in Fig. 7.10. We find that the critical temperatures

---

[2]Note that for technical reasons we show a continuous surface in the figure, omitting the jump in the order parameter.
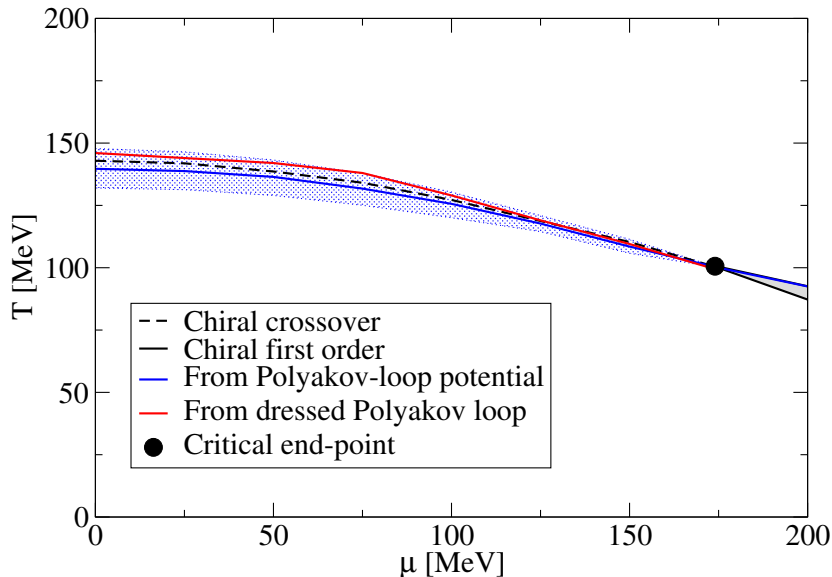
Figure 8.5: The phase diagram for the chiral transition compared to the deconfinement transition obtained from the dressed Polyakov loop as well as the Polyakov-loop potential. The shaded blue area shows the width of the transition from the Polyakov-loop potential.

for all three order parameters agree up to $\Delta T \approx 7$ MeV. They converge to the same temperature when the critical end-point is approached, and coincide there. We also show the width of the deconfinement transition here, which we obtain from

$$\frac{dL[\langle A_4 \rangle]}{dT} > 0.8 \cdot \left.\frac{dL[\langle A_4 \rangle]}{dT}\right|_{max}, \tag{8.20}$$

i.e. the area where the derivative of the Polyakov loop reaches 80 percent of its maximal value. This shows how the transition becomes steeper with growing chemical potential, until it becomes a first-order phase transition at the CEP. We also find that T_c for all three order parameters lies inside this area, which suggests that the difference is only due to the crossover nature of the transition below the CEP.

From the Polyakov-loop potential we therefore confirm our findings from the dressed Polyakov loop. There is no sign of a splitting of the chiral and deconfinement transitions at least up to the CEP. We also confirm our interpretation of the behaviour of T_c determined from the dressed Polyakov loop around $\mu = 75$ MeV. There we found a larger difference to the chiral transition than at smaller or larger chemical potentials. We assumed this to be an artefact of the dual condensates. Indeed, no sign of such a behaviour is found from the Polyakov-loop potential.

8.5.1 Influence of the chemical potential on the glue potential

So far, we considered the full potential, including the quark loop. As an input to Polyakov-loop extended effective models, the pure glue potential, *i.e.* the Eq. (8.7) without the quark loop is of interest. In [125], the glue potential from the FRG was used to improve such effective models at vanishing density. With our solutions of the gluon DSE at finite μ, we are in the position to extend this to the full phase diagram.

The only influence of the chemical potential on V_{glue} is via the quark-loop in the gluon DSE, see Fig. 7.1, since we take the quenched ghost as an input. In our truncation, we can therefore split the unquenched gluon loop in Fig. 8.1 into a loop with the quenched gluon and an unquenching diagram, see Fig. 8.6. We therefore find the only difference of V_{YM} and V_{glue} to be the two-loop diagram in the right of Fig. 8.6.
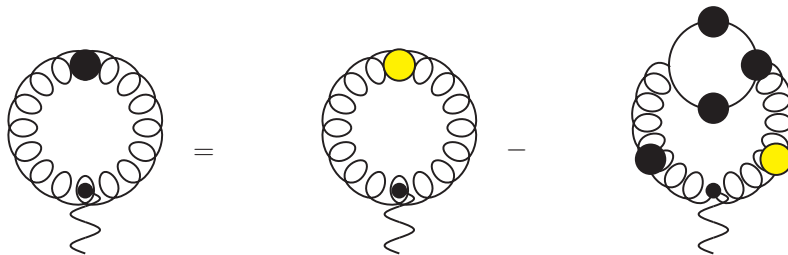

Figure 8.6: The unquenched gluon loop (left) can be split into the quenched loop (yellow dot) and a two-loop diagram involving both propagators and a quark loop.

In Fig. 8.7 we show the pure glue potential V_{glue} at $\mu = 0$, 100 and 200 MeV at $T = 115$ MeV. At the largest chemical potential, we are already in the quark-gluon plasma. Fig. 8.7 is related to the right part of Fig. 8.3, where at the same temperature the full Polyakov-loop potential was shown as a function of chemical potential.

The influence of unquenching the pure glue potential is evidently a reduction of the gluon propagator, and therefore a deeper potential, since the ghost in our approximation is unaffected by the unquenching process. This is visible in Fig. 8.7. With growing chemical potential the quark loop becomes stronger, and therefore the potential deeper. If we would include unquenching effects in the ghost by solving the ghost DSE, we would find a reduction of this effect. Since the effect of the chemical potential on the glue potential is already rather small, we conclude that neglecting a μ-dependence in model studies is well justified.

8.6 Summary

In this chapter, we studied a recently developed method to study the Polyakov-loop potential, based on the Green's functions of QCD, by introducing a background field. We applied this to our results for the unquenched quark and gluon propagators at
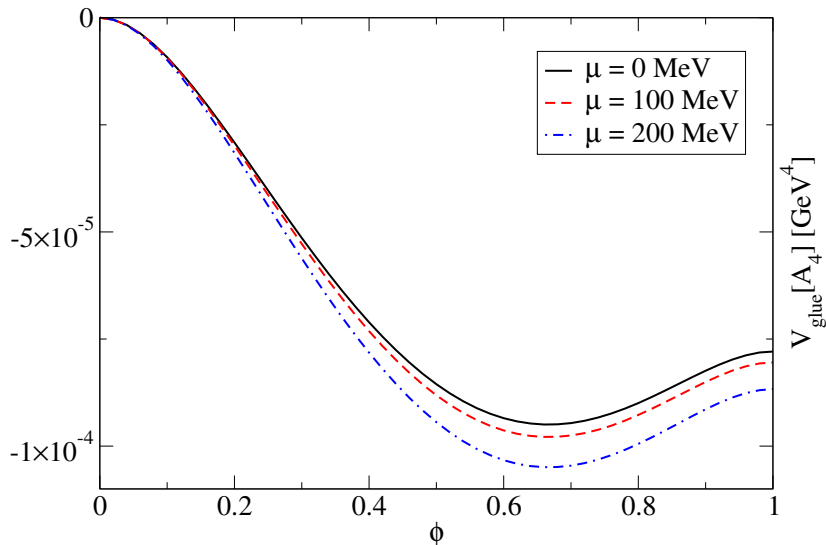
Figure 8.7: The pure glue potential for three different chemical potentials at $T = 115$ MeV.

finite temperature and chemical potential. Thus, we could obtain the Polyakov-loop potential at finite density from QCD degrees of freedom for the first time.

If we obtain the Polyakov loop from the background field, we find an order parameter for confinement. This order parameter shows a transition that is tightly linked to the chiral restoration, since it is triggered by a quark loop. We therefore confirm our earlier findings from the dressed Polyakov loop, in so far as the chiral and deconfinement transitions always happen at similar temperatures. A qualitative difference to the dressed Polyakov loop was found at the first order phase transition at large densities. There, from the Polyakov-loop potential, we find a strong first order phase transition. The dressed Polyakov loop does not show this behaviour, and might even be a crossover or second order phase transition.

In future studies of Dyson-Schwinger equations in a medium, the order parameter obtained in this chapter might be preferred over the dressed Polyakov loop for two reasons. First of all, it is technically much easier to obtain. For the dressed Polyakov loop, the quark DSE needs to be solved for a set of boundary conditions φ. At large densities and temperatures above T_c, we found a jump in φ-direction, which needs to be resolved to a high accuracy in order for the dressed Polyakov loop to be stable. In contrast to that, the Polyakov-loop potential can be obtained from one solution of the quark and gluon DSEs. The numerical costs are therefore much smaller. Secondly, some doubt remains concerning the applicability of the dressed Polyakov loop outside of lattice QCD. This is due to the possibility to find a "deconfinement" phase transition from this order parameter even in the NJL model, which does not feature confinement in the first place. This certainly is an artefact, and raises the question how far our results are affected by the same artificial behaviour.

Finally, the present work is a good starting point for further studies. By being able to obtain the Polyakov-loop potential everywhere in the phase diagram we can make contact to effective models which have to rely on a model input for the potential. A further possibility is to investigate the upper-right corner of the Columbia plot (see Fig. 1.1), *i.e.* the case of heavy quarks.

9 The influence of mesons on the phase diagram

So far, we paid attention mainly to the glue part of our truncation scheme, and used a relatively simple model for the quark-gluon vertex. While this worked quite well so far, there is good reason to improve the vertex *ansatz*. As we have seen in Fig. (7.7), we over-estimate the amount of chiral symmetry breaking in the high-temperature phase. We traced this back to the constant infrared strength, defined by d_1, of our vertex *ansatz* function. In an improved model, d_1 might be taken as temperature dependent. Also, the scalar part of the vertex is known to be important for chiral symmetry breaking, as it vanishes in the chirally restored phase. A study of a truncated form of the vertex DSE, back-coupled to the quark and gluon DSEs, is certainly highly desirable. While this has to remain for future work, one may notice and exploit many physical effects in the vertex. In this chapter, we will use the vertex DSE to introduce the back-reaction of pions onto the quark propagator. Since pions are the pseudo-Goldstone bosons of chiral symmetry breaking, it is no surprise that their interplay is important at the phase transition. Indeed it was shown in [50] that the meson sector dominates the physics at the phase transition for very small quark masses. This leads to the scaling analysis that suggests a second order phase transition in the $O(4)$ universality class.

In [126] a model for the pion back-reaction was introduced in the vacuum. This model was used in [87] and subsequent works to study pion cloud effects in meson phenomenology. In [127] this model was adopted to the CFL phase at large chemical potentials, and in [128, 129] to finite temperature. The main result of [129] is that this model can reproduce the correct $O(4)$ scaling behaviour for $N_f = 2$, if one assumes that the pion decay constant f_π scales appropriately. We will first give a summary of this model and then apply it to the phase diagram in this chapter.

9.1 Pion back-reaction from the vertex DSE

In Fig. (9.1), we show the vertex DSE in terms of two-particle irreducible (2PI) Green's functions. The first three loops belong to the non-Abelian dressing of the vertex, while the last diagram is also present in Abelian theories. It involves a quark-antiquark scattering kernel. It has been argued in [126], that this kernel contains a meson pole, shown in the first diagram of Fig. 9.2, as well as poles from diquarks and baryons (second and third loop).
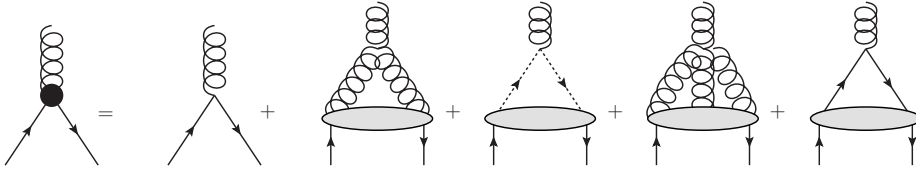
Figure 9.1: The DSE for the quark-gluon vertex. The big blobs symbolise the 2PI Green's function. All internal propagators are dressed, which is not shown here. The dashed line in the second loop corresponds to the ghost propagator.
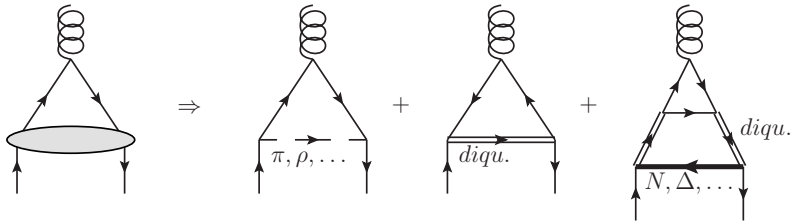

Figure 9.2: The hadron poles in the quark-antiquark scattering kernel. The diagrams describe meson, diquark and baryon exchange.

In the vertex *ansatz* we used so far, one might consider the pion pole to be included effectively. This of course omits all medium effects that the pion might contribute. The basic concept of the pion back-reaction is now to make the pion pole explicit, as shown in the left part of Fig. (9.3). Our old vertex is now considered to be *without* the pion pole, and we add the one-loop term that describes the pion exchange. When this diagram is inserted into the quark's self energy, we get a two-loop diagram, shown in the right part of Fig. (9.3). This two-loop diagram can be approximated by a one-loop diagram, by referring to the homogeneous pion Bethe-Salpeter equation (BSE), see Fig. (2.3). However, this is only an approximation: the quark-gluon vertex in the two-loop diagram is undressed, while it is fully dressed in the BSE. Secondly, with the pion contribution there also exists a pion exchange diagram in the BSE, which is not considered here. This leads to the question how the dressing of the left pion-quark vertex in the right-most diagram of Fig. (9.3) can best be described. In the original work, see [126], both pion-quark vertices where equally dressed with the pion Bethe-Salpeter amplitude. In later work [130], this was believed to be an over-estimation of the pion effects, and one vertex was taken to be bare. However, in the scaling analysis [129] it was shown that the correct scaling at T_c can only be obtained when both vertices have the same scaling behaviour. Since we are not interested in the scaling behaviour here, we will dress only one vertex to avoid over-estimating the impact of the pions on the phase diagram. We checked by explicit calculations that this choice does not affect the results qualitatively.
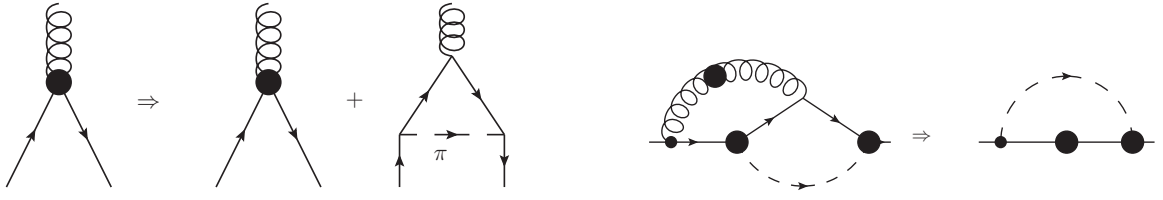
Figure 9.3: The left diagram shows the pion-pole contribution in the vertex. In the pion-exchange diagram, the internal propagators and quark-pion vertices are dressed. In the right diagram we show the approximation of turning the two-loop diagram into a one-loop diagram.
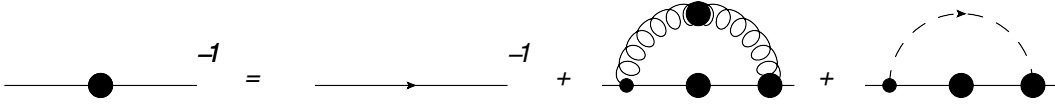

Figure 9.4: The resulting quark DSE with the pion exchange diagram.

This leads to the quark DSE shown in Fig. (9.4). Note that the modification of the quark-gluon vertex is only done on the level of the quark DSE. We omit the additional two-loop diagram that is generated in the gluon DSE, which is a quark-loop with a pion exchange.

9.2 The pion-quark vertex at finite temperature

To close the set of equations, we need to specify the pion-quark vertex. For on-shell pions this is defined by the homogeneous pion BSE, Eq. (2.22).

For the complete back-reaction onto the quarks, one would have to solve the BSE at finite temperature/density. This is not only beyond of the scope of this work, it is also not necessary for an impression of the qualitative effects. In section 2.4 we have repeated the result of solving the BSE in the chiral limit, that entails $\Gamma_\pi(p, P) = \gamma_5 B(p^2)/f_\pi$ in the vacuum. With this, f_π, r_π and M_π could be approximated. We will now have to generalise these approximations to finite temperature.

First of all, the relation $E = B/f_\pi$, where E has been defined in Eq. (2.25) as the dominant BSA dressing, is only true in the chiral limit. When a finite quark mass is introduced, the UV behaviour is different: while the B-function develops a logarithmic running [131], the E-function retains the chiral behaviour, *i.e.* a power law. This affects the finiteness of integrals involving Γ_π, e.g. for r_π, see Eq. (2.28). To amend

the situation we introduce the correct UV behaviour by hand, by using

$$E(p^2) \approx \frac{B(p^2)r(p^2)}{f_\pi}, \tag{9.1}$$

$$r(p^2) = \frac{a}{a + p^2}, \tag{9.2}$$

where we introduce the regulator r with parameter $a = 80$ GeV^2. The regulator is constructed such that $E(p^2) = B(p^2)/f_\pi$ in the IR, and $\propto 1/p^2$ in the UV. The next challenge is to develop a Pagels-Stokar-like formula for f_π at finite temperature.

9.2.1 Pion decay constants at finite temperature

It has been pointed out in [132] that for a system where Lorentz invariance is broken, e.g. when we choose the reference frame of the medium, there are two distinct pion decay constants. While for vanishing temperature f_π is defined though Eq. (2.26), in the medium we have the

$$\langle 0|J_{5,i}^a|\pi^b(P)\rangle = \mathrm{i} f_\pi^s \delta^{ab} P_i, \tag{9.3}$$

$$\langle 0|J_{5,4}^a|\pi^b(P)\rangle = \mathrm{i} f_\pi^t \delta^{ab} P_4, \tag{9.4}$$

where $i \in \{1, 2, 3\}$. In [133, 134] it has been noted that f_π^t and f_π^s have a different behaviour around T_c. Transversal to the heat bath, f_π^s is an order parameter that shows the scaling behaviour $t^{\nu/2}$ with $t = (T_c - T)/T_c$ and critical exponent ν. Longitudinal to the heat bath, f_π^t stays finite even at T_c. Also, the pion velocity can be obtained from $u = f_\pi^s/f_\pi^t$. To generalise Eq. (2.27), we therefore have, in the Bethe-Salpeter formalism,

$$f_\pi^s P_i = 3Z_2 \sum_l\!\!\!\!\!\!\int \mathrm{Tr}\left[\Gamma(l, P)S(l_+)\gamma_5 P_i S(l_-)\right], \tag{9.5}$$

$$f_\pi^t P_4 = 3Z_2 \sum_l\!\!\!\!\!\!\int \mathrm{Tr}\left[\Gamma(l, P)S(l_+)\gamma_5 P_4 S(l_-)\right], \tag{9.6}$$

where $l_\pm = l \pm P/2$. We now take $\Gamma_\pi = \gamma_5 E$, and let $P \to 0$. This yields the generalisation of the Pagels-Stokar formula to finite temperature. The resulting equations are

$$f_\pi^s = 12Z_2 \sum_l\!\!\!\!\!\!\int E\left[\sigma_A \sigma_B + \vec{l}^2 \cos^2\vartheta \left(\frac{\partial \sigma_A}{\partial \vec{l}^2}\sigma_B - \sigma_A \frac{\partial \sigma_B}{\partial \vec{l}^2}\right)\right], \tag{9.7}$$

$$f_\pi^t = 12Z_2 \sum_l\!\!\!\!\!\!\int E\left[\sigma_C \sigma_B + \tilde{\omega}_l \left(\frac{\partial \sigma_C}{\partial P_4}\sigma_B - \sigma_C \frac{\partial \sigma_B}{\partial P_4}\right)\bigg|_{P_4 \to 0}\right], \tag{9.8}$$

where $\sigma_F = F/(\tilde{\omega}_l^2 C^2 + \vec{l}^2 A^2 + B^2)$. Note that in Eq. (9.8), we need the derivative of the quark dressing functions with respect to $P_4 = iM_\pi$. This necessitates a complex continuation of the quark propagator, which is in general needed in the Bethe-Salpeter formalism. This is beyond the scope of this work, however. For the sake of simplicity we will therefore use $f_\pi^t \overset{!}{=} f_\pi^s$. We can solve Eq. (9.7) solely on grounds of the quark propagator for real momenta. This approximation also implies $u = 1$, and can not be used to obtain the $O(4)$-scaling behaviour expected in the chiral limit for $N_f = 2$. However, we are mainly interested in the situation of physical quark masses.

9.2.2 Closing the system of equations

We will take only the E function of the full Bethe-Salpeter amplitude into account, *i.e.* we will use

$$\Gamma_\pi(p, P) = \gamma_5 E(p, P), \tag{9.9}$$

and also apply the regulator defined in Eqs. (9.1,9.2). This is a good approximation, since E dominates the full amplitude. We can expect this to also hold at finite temperature by comparing to finite volume studies, see [135]. There, the Bethe-Salpeter equation has been solved in a finite volume. This is insofar similar to a finite temperature as chiral symmetry is restored below a critical volume. It has been found that E is dominant also close to and below the critical volume.

In [129] it has been shown that with the AxWTI in the medium we have

$$E = \frac{B}{f_\pi^t}, \tag{9.10}$$

in the chiral limit, and a pion propagator

$$D_\pi(\vec{p}^2, \omega_p) = \frac{1}{\omega_p^2 + u^2(\vec{p}^2 + M_\pi^2)}, \tag{9.11}$$

where u is the pion velocity. In order to obtain M_π we will use the Gell–Mann-Oakes-Renner relation for which we need the residue r_π. Since this is obtained from coupling the pion to a pseudo-scalar current, there is only one r_π even at finite temperature. It is straight-forward to adapt the Pagels-Stokar-like relation Eq. (2.32) from the vacuum to finite temperature. The result is

$$r_\pi = Z_2 12 \sum\!\!\!\!\!\!\!\int\!\!\frac{E(l)}{\vec{l}^2 A^2(l) + \tilde{\omega}_l^2 C^2(l) + B^2(l)}. \tag{9.12}$$

With this we can approximate $M_\pi^2 \approx 2mr_\pi/f_\pi^s$ and we have all ingredients needed for the pion-exchange diagram.

We write the quark DSE from Fig. (9.4) as

$$S^{-1} = Z_2 S_0^{-1} + Z_2 \Sigma^{YM} + f_t \Sigma^\pi, \tag{9.13}$$

where Σ^{YM} and Σ^{π} are the gluon and pion exchange diagrams. The factor $f_t = 3$ stems from the $N_f = 2$ flavour trace.[1] Now we project the self-energy onto the quark dressing functions with the projectors from Eq. (2.49), and we obtain

$$\Sigma_A^{\pi} = \sum_l \!\!\!\!\!\!\oint \sigma_A E\left(\frac{p+l}{2}\right) D_{\pi}(q) \frac{\vec{l}\vec{p}}{\vec{p}^2}, \tag{9.14}$$

$$\Sigma_B^{\pi} = \sum_l \!\!\!\!\!\!\oint \sigma_B E\left(\frac{p+l}{2}\right) D_{\pi}(q), \tag{9.15}$$

$$\Sigma_C^{\pi} = \sum_l \!\!\!\!\!\!\oint \sigma_C E\left(\frac{p+l}{2}\right) D_{\pi}(q) \frac{\tilde{\omega}_l}{\tilde{\omega}_p}, \tag{9.16}$$

where the momentum dependence of the Bethe-Salpeter amplitudes has been chosen the same way as in the literature, see e.g. [126].
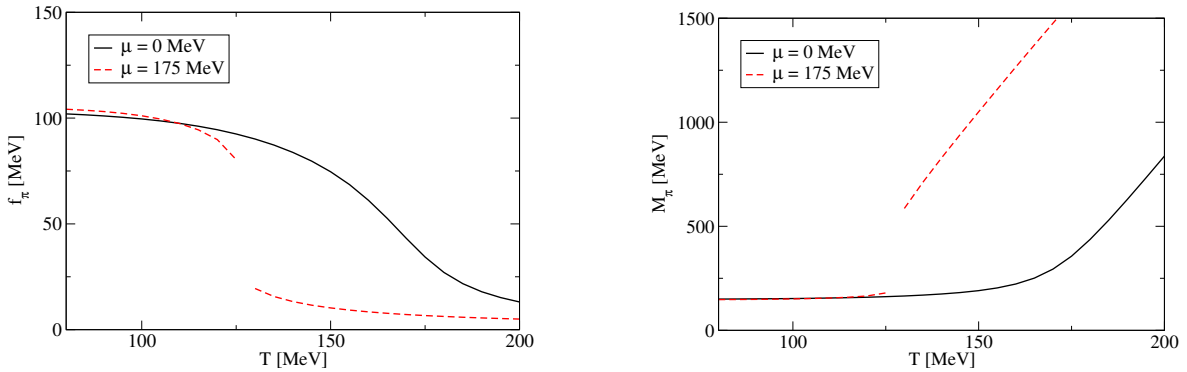
9.3 Results for two flavours

Figure 9.5: The pion decay constant f_{π}^s (left) and mass M_{π} (right) for $\mu = 0$ and $\mu = 175$ MeV.

In this section we will again use the parameter set A, where M_{π} has the physical value for $N_f = 2+1$. In Figure 9.5, we show f_{π}^s and M_{π} as a function of temperature for two densities. Note that our approximations become worse for larger M_{π}, *i.e.* at larger temperatures. The behaviour is nonetheless as expected. While f_{π}^s behaves as an order parameter, M_{π} grows when chiral symmetry is restored. At $\mu = 175$ MeV we observe a jump in f_{π}^s and M_{π} at the first order phase transition. Note that below and above the phase transition $E(0) = B(0)/f_{\pi}$ is roughly the same, since $B(0)$ and f_{π} are equivalent order parameters for the chiral transition. Thus, the pion back-reaction is
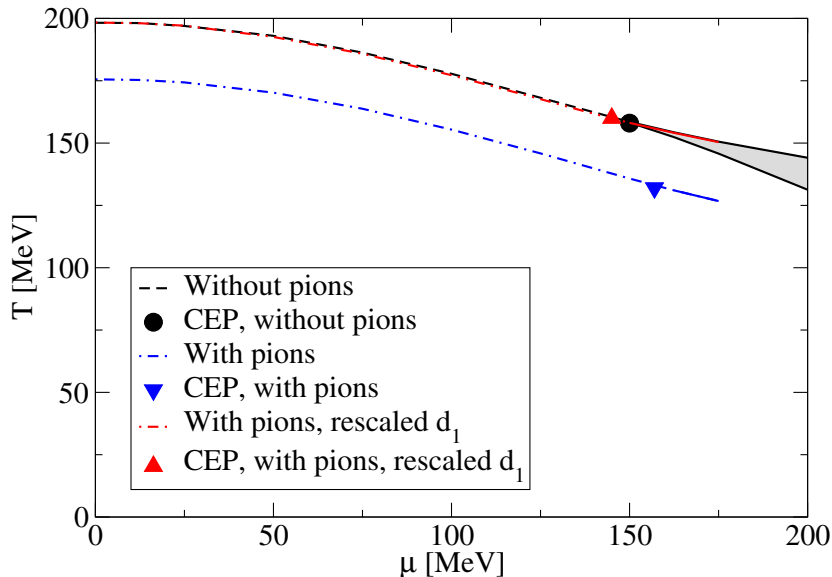
Figure 9.6: The phase diagram with and without pion back-reaction, and with a rescaled vertex strength for better comparison.

only suppressed by the growing thermal pion mass.

In Fig. (9.6), we show the diagram for the chiral phase transition. We compare this to the result from Fig. (7.5), where no back-reaction of pions was included. The effect is mainly a reduction of T_c by about 20 MeV for all μ. The critical end-point is affected only slightly, and moves by a few MeV to larger chemical potentials. To remove the effect of the reduced T_c on the comparison, we also show a result where the vertex strength parameter d_1 is set to 8.5 GeV^2. At this value, $T_c(\mu = 0)$ is almost the same as for the calculation without pion back-reaction. We note that this affects the position of the CEP in the μ direction only slightly. We thus find that upon rescaling the vertex the phase diagram with and without pions is almost identical. This suggests that in future studies the explicit back-reaction of pions may be neglected.

Without rescaling, the curvature with pions taken into account is slightly smaller, with $\kappa = 0.37$, *cf.* $\kappa = 0.41$ without pions. When we rescale the vertex, the curvature increases to $\kappa = 0.45$, and is thus slightly larger than without pion back-reaction. Although this makes our comparison to the lattice data worse, it points towards an interesting effect. In the $N_f = 2 + 1$ calculation, we noticed that the larger number of flavours decreases the curvature. On the lattice, the effect is opposite. If we extrapolate the effect of back-coupling the $N_f = 2$ Goldstone-bosons to $N_f = 2 + 1$, we expect an increase of the curvature. We thus suspect that, if we included an effect that brings our curvature closer to that found in lattice simulations, the back-coupling of Goldstone-bosons might be important to get the correct N_f dependence. This will be further

---

[1]Pictorial, e.g. the u quark couples to a π^+, but only half a π^0. Together with a normalisation factor $\sqrt{2}$ per vertex we obtain $\sqrt{2}^2 \cdot (1 + \frac{1}{2}) = 3$.

investigated in the next section.

We do not show the deconfinement transition in Fig. 9.6. On one hand this is because we do not expect the pion back-reaction to change the general behaviour that we found before, *i.e.* near-by phase transitions. On the other hand, the evaluation of the dual condensate is problematic here. In the quark-pion self-energy, the quark is actually the sea quark, while the test quark is part of the pion. Since we keep the boundary condition φ for the sea quarks physical while we vary it for the test quark, we would have to evaluate the pion for one quark at φ and one at $\varphi = \pi$. How this affects the properties of the pion and the Bethe-Salpeter amplitude is unknown. We will therefore not investigate the dual condensates with pion back-reaction taken into account. Alternatively we could use the Polyakov-loop potential that we studied in the last chapter. However, the mechanism that connects chiral and deconfinement transitions in that potential is not affected by the inclusion of the pions. We therefore have no reason to believe that the results will be any different.

9.4 Results for three flavours

We now further test the hypothesis mentioned above, that the inclusion of Goldstone bosons might yield the correct N_f-dependence of the curvature κ. To this end, we do the same calculations as described above, but with 3 identical light quark flavours. The larger strange quark mass for $N_f = 2 + 1$ leads to larger meson masses, and thus suppresses them further, but only mildly since the physical meson masses are still rather small. We thus expect the strongest effect to come from the number of meson degrees of freedom and not their precise masses. Therefore, we expect the effect of the Goldstone bosons for 3 and $2 + 1$ flavours to be very similar.

Having 3 equal flavours means that the quark loop in the gluon DSE becomes stronger, and that the factor in front of the pion self-energy is increased. In Eq. (9.13), we have to replace the flavour factor $f_t = 3 = \tau^i \tau^i$ with $f_t = 16/3 = \lambda^a \lambda^a$ to accommodate for the larger number of Goldstone bosons.

Without Goldstone bosons we find $T_c(0) = 134.5$ MeV. This is about 14 MeV smaller than in the $2 + 1$ flavour case. For κ we obtain 0.25, which is smaller than 0.28 for $N_f = 2 + 1$. This shows again that κ in our approach depends monotonically on $T_c(0)$.

When we take the Goldstone bosons into account and leave the vertex parameters unchanged, we find $T_c(0) = 103$ MeV and $\kappa = 0.23$. This is qualitatively the same effect that we found for the $N_f = 2$ case, *i.e.* a reduction of $T_c(0)$ as well as a reduction of κ. We then rescale the vertex strength such that we obtain $T_c(0) = 135.5$ MeV. This can be achieved with $d_1 = 9.3$ GeV^2. For the curvature this leads to $\kappa = 0.28$, which is larger than without the back-coupling of Goldstone bosons.

In Tab. (9.1) we summarise our findings for the curvature. If we compare the results without the meson back-coupling and with the rescaled back-coupling, we find that for 2 flavours κ grows by $\approx 9\%$. With 3 equal flavours κ grows by $\approx 11\%$. This is the expected effect, *i.e.* a larger value for κ when more of Goldstone modes are taken into

N_f	no g.b.	with g.b.	with g.b., rescaled
2	0.41	0.37	0.45
$2+1$	0.28	–	–
3	0.25	0.23	0.28

Table 9.1: The curvature for different number of flavours, without and with Goldstone bosons (g.b.) taken into account. Rescaled refers to changing the vertex parameter d_1 such that $T_c(0)$ is the same as without g.b.

account. However, it is rather small and the ordering of κ with N_f is still wrong, even when the Goldstone bosons are taken into account. We therefore found an effect that might be important for the N_f-dependence of the curvature, once we find a κ in the right ballpark.

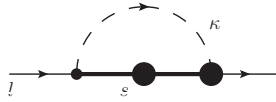## 9.5 Notes about the generalisation to $2+1$ flavours

Figure 9.7: The self-energy of a light quark with a kaon exchange.

So far we only considered two and three equal flavours, hence only the back-reaction of degenerate mesons. In section 7.3, we discussed the effects of strange quarks in unquenched QCD. We argued that additionally to the unquenching effects in the gluon, strange and light quarks couple through the exchange of mesons like kaons. To this end, we can extend the discussion from above to the pseudo-Goldstone bosons of the $N_f = 2+1$ case. This leads to the exchange of the π, κ and η mesons. The resulting equations for light and strange quark are

$$S_l^{-1} = S_{0,l}^{-1} + \Sigma_l^{YM} + 3\Sigma_l^{\pi} + 2\Sigma_l^{\kappa} + \frac{1}{3}\Sigma_l^{\eta}, \tag{9.17}$$

$$S_s^{-1} = S_{0,s}^{-1} + \Sigma_s^{YM} \qquad + 4\Sigma_s^{\kappa} + \frac{4}{3}\Sigma_s^{\eta}, \tag{9.18}$$

where Σ_f^m is the self-energy contribution of meson m on flavour f. Such a model would lead to a stronger reaction of the strange quark on the light-quark phase transition.

Let us now have a closer look on Σ_l^{κ}. For the kaon exchange in the light quark DSE we obtain the diagram in Fig. (9.7). If we project onto the B-function in the usual

way, we obtain

$$B_l(p) = Z_2 Z_m m_l + \Sigma_B^{YM}(p) + 3\Sigma_B^{\pi}(p) + 2\Sigma_B^{\kappa}(p) + \frac{1}{3}\Sigma_B^{\eta}(p), \tag{9.19}$$

$$\Sigma_B^{\kappa}(p) = \sum_l\!\!\!\!\!\!\int \sigma_{B,s}(l) E_\kappa\left(\frac{p+l}{2}\right) D_\kappa(q), \tag{9.20}$$

where $\sigma_{B,s} = B_s/(\tilde{\omega}_l^2 C_s^2 + \vec{l}^2 A_s^2 + B_s^2)$ is determined from the strange quark, and E_κ is the scalar dressing of the kaon Bethe-Salpeter amplitude.

If we now assume $m_l = 0$ but $m_s > 0$, we find a peculiar situation. The Wigner solution of the light quark DSE, *i.e.* $B_l = 0$, is only allowed for $E_\kappa = 0$, since $\sigma_{B,s} > 0$ for all temperatures. This leaves us with two possibilities: either $E_\kappa = 0$ for light quarks in the Wigner phase, or the Wigner phase vanishes when the back-reaction with kaons is taken into account. If we assume the first solution, we set an important constraint on the model for the kaon amplitude. This constraint, however, is not met by our *ansatz* Eq. (9.10). Would we assume that B in this equation is B_l, the kaon decay constant f_κ would vanish for $B_l \to 0$, and $E_\kappa \to \frac{0}{0}$. We therefore need to get a better understanding of the kaon Bethe-Salpeter amplitude at finite temperature before we can employ the meson back-coupling to the $N_f = 2 + 1$ case. However, the situation might change once we improve the approximations made in this model.

9.6 Summary

In this chapter we implemented the back-reaction of Goldstone bosons. This is motivated from the quark-gluon vertex DSE, where a quark-antiquark scattering kernel appears, and is an effective improvement of our vertex *ansatz*. This entails a second unquenching effect, additional to the quark-loop contribution to the gluon propagator. The main effect of including Goldstone modes is a reduction of T_c at all chemical potentials, which is the expected effect for unquenching the theory further. For 2 flavours the pions lead to a T_c about 20 MeV smaller, while the critical end-point moves only slightly to larger μ. We find that a rescaled vertex parameter d_1 can compensate the effect of the pions to a large degree. With the rescaling taken into account the CEP is at almost the same point as without pion back-coupling. One main result of this chapter is thus that the pion contribution, at least in the approximations used here, can be neglected in future studies of the phase diagram with Dyson-Schwinger equations.

However, we found that the curvature of the critical line at $\mu = 0$ is sensitive to the inclusion of pion degrees of freedom. With the rescaled vertex strength, the curvature is increased by about ten percent. When we go from $N_f = 2$ to $N_f = 3$ we find a larger effect in this direction, since more Goldstone degrees of freedom exist. We identified this as a possible explanation for the N_f-dependence of the curvature, which we do not capture correctly in our truncation so far. If we would include some effect that reduces the curvature to a value near that found in lattice simulations, we therefore

might need to include the Goldstone back-coupling in order to obtain the correct results for different number of flavours. We finally made a comment on the back-coupling of mesons in the $N_f = 2 + 1$ case, which can not be achieved in the current approximation scheme.

In future studies, this model might be the basis to include diquark or even baryon degrees of freedom. In Fig. 9.2 the corresponding exchange diagrams have been included.

10 Conclusion and outlook

In this work we studied the chiral and deconfinement phase transition from solutions of quark and gluon Dyson-Schwinger equations. We employed the quark condensate and the dressed Polyakov loop as order parameters for chiral symmetry breaking and confinement, respectively. The starting point was quenched QCD. There, we used input from gauge-fixed lattice calculations for the quenched gluon propagator as an input to the quark DSE. For three (two) colours we found a phase transition consistent with first (second) order, which shows that our order parameters give the expected results.

With the quenched gluon as an input, we then went on to unquenched QCD by adding the quark loop. With bare quarks in the loop, we found a crossover at vanishing density and a CEP at large chemical potential. This is similar to the inclusion of fermionic fluctuations in the PQM model, where the CEP is located at a similar chemical potential. We found the critical temperatures for chiral restoration and deconfinement to be near-by at all chemical potentials.

Then, we introduced a truncation where the fully dressed quark loop was calculated. In this model, we found results for the gluon propagator that are in good agreement with gauge-fixed lattice simulations. We found that, when the fully dressed quark loop is taken into account, the condensate at zero density can be fitted excellently to corresponding lattice results. The full dressing of the quark loop diminishes the effect of the fermionic fluctuations on the CEP, which was found at much smaller chemical potential than with bare quarks in the loop.

We also showed the first solution of the coupled Dyson-Schwinger equations for light and strange quark propagators in the medium. This leads to the strange quark mimicking the chiral phase transition from the light quark, a non-trivial effect that is owed to the unquenched gluon propagator. The impact of the strange quark on the phase transition line for the light quarks was found to be mainly a reduction of the critical temperatures. From the dressed Polyakov loop we found a deconfinement transition that is always near the chiral transition at all chemical potentials, similar to the simpler model with bare sea quarks.

To test a different notion of confinement we then investigated the Schwinger function of the quark propagator, which can be used to test for positivity violations in the quark spectral functions. For two flavours, we found a (possible) restoration of positivity near the chiral transition at all chemical potentials. However, for $2 + 1$ flavours we found a sign for positivity violations above the chiral critical temperature at large chemical potential. This makes further investigations of the spectral functions at finite density necessary.

With the quark, gluon and ghost propagators at our disposal, we then investigated the Polyakov-loop potential. We calculated this potential for the first time at finite chemical potential from the basic QCD degrees of freedom. From the minimum of the Polyakov-loop potential we obtained a second order parameter for centre symmetry. The resulting deconfinement transition temperature was found to be very close to the chiral transition temperature. In this respect we confirmed our findings from the dual order parameters. We further looked at the pure glue potential, and found a rather week dependence on the chemical potential. This is of interest for effective models, where the Polyakov-loop potential is an important input.

In the last part of this work, we further improved our truncation by taking the back-reaction of Goldstone bosons into account. We found little impact of this improvement on the position of the critical end-point. At small densities we identified a mechanism that might explain the behaviour of the curvature of the critical line when the number of flavours is changed. When including Goldstone bosons we found that the curvature becomes larger, and concluded that with more flavours – and thus more Goldstone bosons – the curvature grows. This is in line with results from the lattice. However, the curvature in this work always turns out much larger than predicted by the lattice

We believe that the truncation presented in this work is a good starting point for further explorations of QCD in a hot and dense medium. The results can already be used to obtain the quark spectral function from fitting routines or the MEM. One may also investigate further thermodynamic observables like the quark number susceptibilities (qns). The qns of the strange quark is often used as a phenomenologically motivated order parameter for confinement. It would be interesting to study if the model presented here is capable of reproducing lattice results of the strange qns. If that is possible a continuation to finite chemical potential would be highly interesting.

The inclusions of fermionic fluctuation in a non-perturbative way might also be important when finite magnetic fields are taken into account.

One might also construct a method to continue the quark propagator for complex p_4. A solution of this would be interesting in itself, since the analytic structure of the quark propagator is believed to be connected to quark confinement. This would also open the possibility to study real-time observables, like viscosities, as well as the Bethe-Salpeter equations for mesons, such as the pion. From this one could also improve our approximations for the pion back-reaction.

Further possibilities would be the extension to imaginary or iso-spin chemical potentials. There, no sign problem exists on the lattice. This would lead to comparisons and tests for our truncation of the DSEs.

Finally, the present truncation can be improved in several ways. First of all, there is already finished work and work in progress for a solution of the Yang-Mills sector at finite temperature. If this could be used to also take unquenching effects in the gluon into account, the basic assumption of our truncation of the gluon DSE could be cross-checked and improved. There are several ways of improving our model for the quark-gluon vertex. One might be to study its infrared divergence which was found to

be connected to the $U_A(1)$ anomaly. Including the anomaly might proof important for the curvature of the critical line. In the long term it will certainly be possible to solve the DSE for the quark-gluon vertex in some approximation. This will yield valuable insights in our understanding of chiral symmetry breaking in the medium. Also, the back-reaction of diquarks and baryons might be included along the ideas of the pion back-reaction. These degrees of freedom are believed to be important at large chemical potentials.

Acknowledgements

A Conventions

A.1 Euclidean space

Throughout this work we use a Euclidean space with metric $g_{\mu\nu} = \delta_{\mu\nu}$. The Euclidean quantum field theory can be connected to one in Minkowski space-time by analytic continuation. We use

$$p = (p_1, p_2, p_3, p_4)^T = (\vec{p}, p_4)^T, \quad x = (x_1, x_2, x_3, \tau)^T = (\vec{x}, \tau)^T, \tag{A.1}$$

as a convention for the momenta and coordinate-space vectors. The connection to Minkowski space-time is

$$\tau = -\mathrm{i}t \quad p_4 = \omega_n = \mathrm{i}p_0 \tag{A.2}$$

where t is the Minkowski time variable, and p_0 the zeroth momentum component in Minkowski space-time. The Dirac matrices in Euclidean space obey

$$\{\gamma_\mu, \gamma_\nu\} = 2\delta_{\mu\nu}, \tag{A.3}$$

$$\gamma_1^2 = \gamma_2^2 = \gamma_3^2 = \gamma_4^2 = 1, \tag{A.4}$$

where $\{\cdot, \cdot\}$ is the anti-commutator.

B Numerical details

B.1 The quark DSE

In principle, the evaluation of the quark DSE is straight forward. The divergence is mild, and a simple iterative algorithm is enough to find solutions, even in the first order area. However, some tricks are useful to optimize the numerical cost.
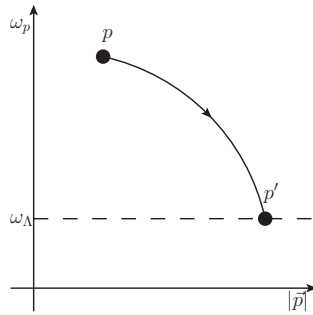

Figure B.1: For large momenta, we can rotate p to p'.

The medium is well-known to affect mainly the infrared part of the dressing functions. Since in the vacuum the dressing functions are $O(4)$-invariant – they do not distinguish between p_4 and $\vec{p}$ – so must be the in-medium dressing functions in the UV. It follows that we can approximate the dressing functions by calculating only up to a maximal Matsubara mode ω_Λ. All higher modes can be rotated to this largest mode, as illustrated in Fig. B.1. Mathematically speaking we have

$$F(\omega_p, \vec{p}^2) \to F(\omega'_p, \vec{p}'^2) = F(\omega_\Lambda, \omega_p^2 - \omega_\Lambda^2 + \vec{p}^2), \tag{B.1}$$

such that $p'^2 = p^2$, where F is some dressing function. This allows us to calculate the dressing functions for a rather small number of Matsubara modes instead of going up to the cut-off. In the quark DSE we usually use $\omega_{-5}\ldots\omega_4$, while for the gluon we only take ω_0 into account.

For large n the Matsubara modes ω_n get dense. This allows, at least in the quark DSE, to substitute the Matsubara sum for large n by a continuous integral. We thus use

$$T \sum_{n=-\infty}^{\infty} \to T \sum_{n=-N-1}^{N} + \int_{-\Lambda}^{\omega_{-N-1}-\pi T} \frac{dp_4}{2\pi} + \int_{\omega_N+\pi T}^{\Lambda} \frac{dp_4}{2\pi}. \tag{B.2}$$

Note, however, that this approximation usually goes horribly wrong in quark-loop diagrams.

B.1.1 Renormalisation

We renormalise by obtaining Z_2 and Z_m in the vacuum, since the medium does not contribute to the divergences. We use a renormalisation point of $\zeta = 80$ GeV, and apply a momentum subtraction scheme. That is, we demand

$$A(\zeta^2) = 1, \tag{B.3}$$
$$B(\zeta^2) = m, \tag{B.4}$$

where $m = m(\zeta)$ is the renormalised bare quark mass.

B.1.2 Finding multiple solutions of the quark DSE

In general, the quark DSE has a large number of solutions (see e.g. [136] for a discussion of this in QED$_3$). In the vacuum, a naïve iteration method is sufficient to find the physical solution. This is also true at finite temperature, as long as the phase transition is not of first order. Around a first order phase transition there is a region of co-existence, where two solutions exist, one of which is energetically preferred. These solutions correspond to the chirally symmetric and restored phases in our case. To find the boundary of the co-existence region we need to find both solutions. This can be achieved by starting the iteration of the quark DSE once with a small seed function B_0 for B, for which we use 10 MeV, and once with a large value, where we choose 1 GeV.

In the unquenched case, with coupled quark and gluon DSEs, we furthermore use the following procedure. We start by obtaining the quark loop from a bare propagator with $m = B_0$. With the resulting unquenched gluon propagator we then solve the quark DSE, and iterate the quark-gluon system. For a small B_0 this means to start with a small interaction strength, which will let the system run into the small-B solution of the quark DSE. For a large B_0 the initial interaction strength is large, and we find the large-B solution.

B.2 The quark loop in the gluon DSE

Due to the quadratic divergence, the evaluation of the quark loop must be treated with great care. We already discussed some of the issues in section 7.2. In the evaluation of the thermal mass $m_{th.}^2$ we furthermore find three more procedures to be necessary. Firstly, the Matsubara sum must be evaluated explicitly, the approximation Eq. (B.2) results in a reappearance of the quadratic divergence. Secondly, the cutoff dependence is rather large in this object, and we find it to converge only at $\Lambda = 2$ TeV. The third

point is that the integral should be performed with an $O(4)$-invariant cutoff, *i.e.*

$$T \sum_n \int d^3p \to T \sum_{n=-N-1}^{N} \int_{\epsilon^2}^{\Lambda'^2-\omega_n^2} d\vec{p}^2 \frac{|\vec{p}|}{2} \int d\Omega, \tag{B.5}$$

where $\Lambda' = \pi T(2N+2)$ is a temperature-dependent cutoff, that is chosen close to the fixed cutoff Λ by taking N from the Matsubara mode closest to Λ.

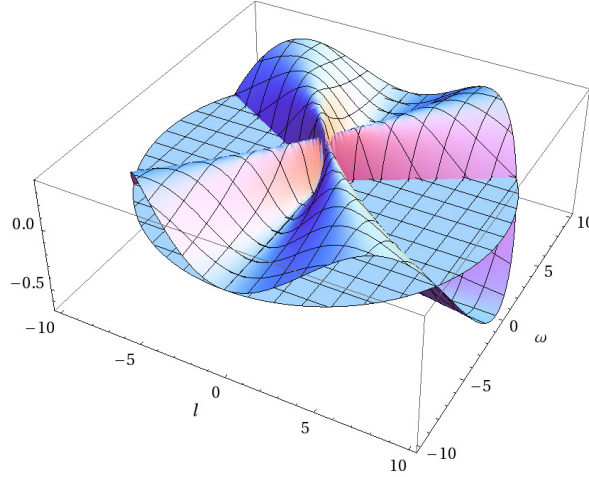

Figure B.2: The integrand of the thermal mass in perturbation theory.

The need for an $O(4)$-invariant cutoff is illustrated in Fig. B.2. The figure shows the integrand of the thermal gluon mass, Eq. (7.15), for $A = C = 1$, $B = 0$. The measure for spherical coordinates is included. The plot shows positive and negative contributions that cancel exactly for $T = 0$, where $\omega = l_4$ is a continuous variable. In hyper-spherical coordinates the integration over the angle ϑ_4, which is the angle between l_4 and $\vec{l}$, cancels and the thermal mass is zero. At finite temperature $\omega = \omega_n$ is discreet, and an integration over ϑ_4 not possible. One thus has cancelling effects only after the Matsubara sum and the spatial integration have been performed.

We furthermore find that the difference $|A-C|$ might lead to a quadratic divergence, if it does not fall off quickly enough. Since this difference is a pure thermal effect, it should go like $|A - C| \propto \exp(-p/T)$ for large p. However, numerically this difference is larger, and needs to be removed by hand. To this end, we set $A(p^2) = C(p^2)$ for $p^2 > 40$ GeV^2, which is an energy scale that has been found to work best.

B.3 Evaluation of the dual condensates

In Eq. (3.17) we defined the dual condensates as Fourier transform of the quark condensate for boundary condition φ. In the numerical evaluation of this, especially at finite density, one runs into a few difficulties.

First of all, for a cut-off Λ and quark mass m the condensate is divergent with $m\Lambda^2$. This term does not depend on φ, and thus drops out in the Fourier transform. This is visible in Fig. 5.5 where we show Σ_{+1} for quenched QCD. There we found a dual condensate that is consistent with zero below T_c, which provides proof that indeed the divergence cancels. Nonetheless, for a large quark mass, the evaluation of Eq. (3.17) becomes quite sensitive on the numerical details. This might be due to the divergence, *i.e.* a bad signal-to-noise ratio. This, together with numerical problems in the quark DSE, unfortunately hinders the limit $m \to \infty$ for the test quark. In this limit the dressed Polyakov loop is dominated by the thin one, which could therefore be accessed, would one be able to take the limit numerically.

If we turn on the chemical potential, we find a jump of the condensate in φ-direction. This was shown in Fig. 6.5 for the HTL-like approximation. The φ-integral has thus to be evaluated with great care. Luckily, we find that the jump appears in most cases well above the deconfinement temperature, and we can ignore this problem if we are just interested in determining the deconfinement temperature. For a determination of $\Sigma_{\pm 1}$ above T_c we apply an adaptive integration method. To this end we employ a Gauss-Kronrod algorithm of orders three and seven. This has been used for Fig. 7.9. The effect of the adaptive integration is a very precise resolution of $\langle \bar{\psi}\psi \rangle_\varphi$ around the jump. The numerical effort for this is huge, since resolving the jump is hindered by critical slowing down, and results in numerical run-times of the order of weeks.

C Evaluation of the background-field DSE

C.1 Yang-Mills part

For the gluon and ghost loop we can follow [74] in the evaluation of the DSE for the background field. In section 8.2 we repeated the vertices for the coupling of the background field to gluon and ghost, leaving the definition of the ordinary vertices open. They are

$$\left(S^{(3)}_{a_\rho a_\mu a_\nu}\right)^{abc}_{\mu\nu\rho}(p,q,k) = g f^{abc}\left(\delta_{\mu\nu}(p-q)_\rho + \delta_{\nu\rho}(q-k)_\mu + \delta_{\rho\mu}(k-p)_\nu\right), \qquad \text{(C.1)}$$

$$\left(S^{(3)}_{a_\rho c\bar{c}}\right)^{abc}_\mu(p,q,k) = g f^{abc} q_\mu. \qquad \text{(C.2)}$$

The ghost loop is evaluated straightforwardly, since the ghost is a scalar. For the gluon loop we encounter an additional complexity by the gauge part of the vertex, Eq. (8.8). The gluon propagator can be written as

$$D_{\mu\nu} = D^{\mathcal{T}}_{\mu\nu} + \xi \bar{D}_\mu \frac{1}{\bar{D}^2} \bar{D}_\nu, \qquad \text{(C.3)}$$

where $\mathcal{T}$ denotes transversal to the gluon momentum. Together with the gauge part of the vertex, Eq. (8.8), we obtain

$$\frac{\delta}{\delta \bar{A}_\mu} \frac{1}{2} \text{Tr}\left[\ln\left(-\bar{D}^2\right)\right], \qquad \text{(C.4)}$$

which is the derivative of the Weiss potential. This is the first part of Eq. (8.17).

C.2 Quark loop

In the last section we ignored the colour structure of the loops. Without the background field any loop of Fig. 8.1 would vanish due to the colour trace involved, e.g. the ghost loop would be $\propto f_{abc}\delta_{ac} = 0$. Let us examine how this changes in the presence of the background field for the quark loop, which has not been discussed in [74]. In the presence of the background field we can write the inverse propagator as

$$S^{-1} = p_4\gamma_4 C + \vec{p}\vec{\gamma}A + B, \qquad \text{(C.5)}$$

where $p_4 = \tilde{\omega}_p + g\bar{A}_4$. If we assume $\bar{A}_4 = \bar{A}_4^3 \frac{\lambda^3}{2}$ we can split the inverse propagator into a part diagonal in colour space and one proportional to λ^3 as

$$S^{-1} = d\mathbb{1} + a\lambda^3. \tag{C.6}$$

The colour structure of the quark loop is then schematically written as

$$S_{ij}\left(\lambda^3\right)_{ji} = (a-d)^{-1} + (a+d)^{-1}, \tag{C.7}$$

such that we recover the quark part of Eq. (8.19).

D Gluon fit at finite temperature

In Tab. (D.1) we show the fit results $a_{T,L}(T)$ and $b_{T,L}(T)$ for the quenched gluon propagator in Yang-Mills theory with two and three colours. The input lattice data is taken from reference [93].

T/T_c	$SU(3)$				$SU(2)$			
	a_L	b_L	a_T	b_T	a_L	b_L	a_T	b_T
0.361	0.29567	1.09275	0.62218	1.29798	0.65152	1.46758	1.47936	2.08134
0.44	0.18260	1.03256	0.52943	1.22042	0.78840	1.60681	1.28255	1.87418
0.451	0.23248	1.07438	0.72195	1.36889	0.45501	1.36958	1.54486	2.11416
0.549	0.16101	1.08178	0.83129	1.48887	0.31802	1.26464	1.31946	1.89318
0.603	0.15188	1.05689	1.01143	1.57588	0.24538	1.1994	1.43415	1.89887
0.733	0.07633	1.01709	2.3809	2.85269	0.19171	1.22958	1.38301	1.88193
0.903	0.07842	1.06605	1.05309	1.46572	0.15347	1.26558	1.53785	1.84233
0.925	0.08227	1.1021	0.99772	1.43206	0.13216	1.22851	1.47611	1.7706
0.947	0.06870	1.06355	1.88604	2.17354	0.13772	1.23005	1.46541	1.75731
0.968	0.06481	1.07286	1.06106	1.47005	0.13040	1.20892	1.441	1.74285
0.974	0.06101	1.05938	1.37587	1.6823	0.1348	1.22137	1.44207	1.74256
0.98	0.05995	1.06543	0.93796	1.38259	0.14110	1.27387	1.45362	1.75598
0.986	0.06154	1.06812	0.98667	1.42748	0.13627	1.24268	1.46095	1.77597
0.991	0.05526	1.04881	1.09137	1.47191	0.13565	1.22437	1.52035	1.84982
0.996	0.07606	1.0386	0.92578	1.37917	0.13972	1.22201	1.40715	1.69906
1	0.13841	0.98595	0.69330	1.27618	0.17256	1.24356	1.45887	1.79928
1.005	0.10538	0.89338	0.59384	1.17859	0.18431	1.22535	1.45696	1.81378
1.01	0.21321	1.00521	0.70669	1.32059	0.25249	1.23504	1.51804	1.88951
1.02	0.24654	1.01209	0.69189	1.28319	0.35245	1.268	1.38173	1.73514
1.025	0.43520	1.19735	0.68257	1.28175	0.48215	1.34332	1.38838	1.74171
1.03	0.34843	1.09821	0.65923	1.25966	0.48564	1.34751	1.39136	1.7691
1.04	0.37110	1.08848	0.70072	1.3089	0.76786	1.54997	1.40566	1.79054
1.06	0.49990	1.16938	0.75533	1.37162	0.87753	1.56108	1.38763	1.77732
1.08	0.63905	1.23382	0.65493	1.22316	1.10256	1.69241	1.34978	1.75341
1.1	0.53422	1.11342	0.63614	1.19496	1.09275	1.64844	1.44497	1.86777
1.81	0.80583	0.84197	1.15243	1.37157	1.77988	0.77193	1.67666	1.61259
2.2	0.52230	0.58698	1.33834	1.26879	2.05434	0.45680	1.5094	1.34957

Table D.1: Fit results for three and two colour quenched QCD.

Note that we used a different normalisation of the gluon propagator then in [42], which is why the values differ at the temperatures that where already used in that reference.

Bibliography

[1] M. Gell-Mann, "A Schematic Model of Baryons and Mesons," *Phys.Lett.* **8** (1964) 214–215.

[2] G. Zweig, "An SU(3) model for strong interaction symmetry and its breaking,".

[3] E. D. Bloom, D. Coward, H. DeStaebler, J. Drees, G. Miller, *et al.*, "High-Energy Inelastic e p Scattering at 6-Degrees and 10-Degrees," *Phys.Rev.Lett.* **23** (1969) 930–934.

[4] M. Breidenbach, J. I. Friedman, H. W. Kendall, E. D. Bloom, D. Coward, *et al.*, "Observed Behavior of Highly Inelastic electron-Proton Scattering," *Phys.Rev.Lett.* **23** (1969) 935–939.

[5] J. C. Collins and M. Perry, "Superdense Matter: Neutrons Or Asymptotically Free Quarks?," *Phys.Rev.Lett.* **34** (1975) 1353.

[6] N. Cabibbo and G. Parisi, "Exponential Hadronic Spectrum and Quark Liberation," *Phys.Lett.* **B59** (1975) 67–69.

[7] U. W. Heinz and M. Jacob, "Evidence for a new state of matter: An Assessment of the results from the CERN lead beam program," `arXiv:nucl-th/0002042 [nucl-th]`.

[8] **PHENIX Collaboration** Collaboration, K. Adcox *et al.*, "Formation of dense partonic matter in relativistic nucleus-nucleus collisions at RHIC: Experimental evaluation by the PHENIX collaboration," *Nucl.Phys.* **A757** (2005) 184–283, `arXiv:nucl-ex/0410003 [nucl-ex]`.

[9] B. Muller, J. Schukraft, and B. Wyslouch, "First Results from Pb+Pb collisions at the LHC," *Ann.Rev.Nucl.Part.Sci.* **62** (2012) 361–386, `arXiv:1202.3233 [hep-ex]`.

[10] L. McLerran and R. D. Pisarski, "Phases of cold, dense quarks at large N(c)," *Nucl.Phys.* **A796** (2007) 83–100, `arXiv:0706.2191 [hep-ph]`.

[11] A. J. Mizher, M. Chernodub, and E. S. Fraga, "Phase diagram of hot QCD in an external magnetic field: possible splitting of deconfinement and chiral transitions," *Phys.Rev.* **D82** (2010) 105016, `arXiv:1004.2712 [hep-ph]`.

[12] **Wuppertal-Budapest Collaboration** Collaboration, S. Borsanyi *et al.*, "Is there still any T_c mystery in lattice QCD? Results with physical masses in the continuum limit III," *JHEP* **1009** (2010) 073, `arXiv:1005.3508 [hep-lat]`.

[13] A. Bazavov, T. Bhattacharya, M. Cheng, C. DeTar, H. Ding, *et al.*, "The chiral and deconfinement aspects of the QCD transition," *Phys.Rev.* **D85** (2012) 054503, `arXiv:1111.1710 [hep-lat]`.

[14] F. R. Brown, F. P. Butler, H. Chen, N. H. Christ, Z.-h. Dong, *et al.*, "On the existence of a phase transition for QCD with three light quarks," *Phys.Rev.Lett.* **65** (1990) 2491–2494.

[15] P. de Forcrand, "Simulating QCD at finite density," *PoS* **LAT2009** (2009) 010, `arXiv:1005.0539 [hep-lat]`.

[16] Z. Fodor and S. Katz, "Lattice determination of the critical point of QCD at finite T and mu," *JHEP* **0203** (2002) 014, `arXiv:hep-lat/0106002 [hep-lat]`.

[17] P. de Forcrand and O. Philipsen, "Constraining the QCD phase diagram by tricritical lines at imaginary chemical potential," *Phys.Rev.Lett.* **105** (2010) 152001, `arXiv:1004.3144 [hep-lat]`.

[18] S. Klevansky, "The Nambu-Jona-Lasinio model of quantum chromodynamics," *Rev.Mod.Phys.* **64** (1992) 649–708.

[19] B.-J. Schaefer and J. Wambach, "The Phase diagram of the quark meson model," *Nucl.Phys.* **A757** (2005) 479–492, `arXiv:nucl-th/0403039 [nucl-th]`.

[20] K. Fukushima, "Chiral effective model with the Polyakov loop," *Phys.Lett.* **B591** (2004) 277–284, `arXiv:hep-ph/0310121 [hep-ph]`.

[21] E. Megias, E. Ruiz Arriola, and L. Salcedo, "Polyakov loop in chiral quark models at finite temperature," *Phys.Rev.* **D74** (2006) 065005, `arXiv:hep-ph/0412308 [hep-ph]`.

[22] C. Ratti, M. A. Thaler, and W. Weise, "Phases of QCD: Lattice thermodynamics and a field theoretical model," *Phys.Rev.* **D73** (2006) 014019, `arXiv:hep-ph/0506234 [hep-ph]`.

[23] B.-J. Schaefer, J. M. Pawlowski, and J. Wambach, "The Phase Structure of the Polyakov–Quark-Meson Model," *Phys.Rev.* **D76** (2007) 074023, `arXiv:0704.3234 [hep-ph]`.

[24] V. Skokov, B. Stokic, B. Friman, and K. Redlich, "Meson fluctuations and thermodynamics of the Polyakov loop extended quark-meson model," *Phys.Rev.* **C82** (2010) 015206, `arXiv:1004.2665 [hep-ph]`.

[25] T. K. Herbst, J. M. Pawlowski, and B.-J. Schaefer, "The phase structure of the Polyakov–quark-meson model beyond mean field," *Phys.Lett.* **B696** (2011) 58–67, `arXiv:1008.0081 [hep-ph]`.

[26] Z. Fodor and S. Katz, "Critical point of QCD at finite T and mu, lattice results for physical quark masses," *JHEP* **0404** (2004) 050, `arXiv:hep-lat/0402006 [hep-lat]`.

[27] R. Gavai and S. Gupta, "The Critical end point of QCD," *Phys.Rev.* **D71** (2005) 114014, `arXiv:hep-lat/0412035 [hep-lat]`.

[28] P. de Forcrand and O. Philipsen, "The Chiral critical point of N(f) = 3 QCD at finite density to the order (mu/T)**4," *JHEP* **0811** (2008) 012, `arXiv:0808.1096 [hep-lat]`.

[29] M. G. Alford, A. Schmitt, K. Rajagopal, and T. Schäfer, "Color superconductivity in dense quark matter," *Rev.Mod.Phys.* **80** (2008) 1455–1515, `arXiv:0709.4635 [hep-ph]`.

[30] T. Kojo, Y. Hidaka, K. Fukushima, L. D. McLerran, and R. D. Pisarski, "Interweaving Chiral Spirals," *Nucl.Phys.* **A875** (2012) 94–138, `arXiv:1107.2124 [hep-ph]`.

[31] S. Carignano, D. Nickel, and M. Buballa, "Influence of vector interaction and Polyakov loop dynamics on inhomogeneous chiral symmetry breaking phases," *Phys.Rev.* **D82** (2010) 054009, `arXiv:1007.1397 [hep-ph]`.

[32] J. Braun, L. M. Haas, F. Marhauser, and J. M. Pawlowski, "Phase Structure of Two-Flavor QCD at Finite Chemical Potential," *Phys.Rev.Lett.* **106** (2011) 022002, `arXiv:0908.0008 [hep-ph]`.

[33] L. Fister and J. M. Pawlowski, "Yang-Mills correlation functions at finite temperature," `arXiv:1112.5440 [hep-ph]`.

[34] C. D. Roberts and S. M. Schmidt, "Dyson-Schwinger equations: Density, temperature and continuum strong QCD," *Prog.Part.Nucl.Phys.* **45** (2000) S1–S103, `arXiv:nucl-th/0005064 [nucl-th]`.

[35] D. Nickel, J. Wambach, and R. Alkofer, "Color-superconductivity in the strong-coupling regime of Landau gauge QCD," *Phys.Rev.* **D73** (2006) 114028, `arXiv:hep-ph/0603163 [hep-ph]`.

[36] D. Müller, M. Buballa, and J. Wambach, "Dyson-Schwinger approach to color superconductivity at finite temperature and density," `arXiv:1303.2693 [hep-ph]`.

[37] D. Müller, *QCD at finite density with Dyson-Schwinger equations.* PhD thesis, TU Darmstadt, 2013.

[38] A. Maas, J. Wambach, B. Gruter, and R. Alkofer, "High-temperature limit of Landau-gauge Yang-Mills theory," *Eur.Phys.J.* **C37** (2004) 335–357, `arXiv:hep-ph/0408074 [hep-ph]`.

[39] B. Gruter, R. Alkofer, A. Maas, and J. Wambach, "Temperature dependence of gluon and ghost propagators in Landau-gauge Yang-Mills theory below the phase transition," *Eur.Phys.J.* **C42** (2005) 109–118, `arXiv:hep-ph/0408282 [hep-ph]`.

[40] C. S. Fischer, "Deconfinement phase transition and the quark condensate," *Phys.Rev.Lett.* **103** (2009) 052003, `arXiv:0904.2700 [hep-ph]`.

[41] C. S. Fischer and J. A. Mueller, "Chiral and deconfinement transition from Dyson-Schwinger equations," *Phys.Rev.* **D80** (2009) 074029, `arXiv:0908.0007 [hep-ph]`.

[42] C. S. Fischer, A. Maas, and J. A. Muller, "Chiral and deconfinement transition from correlation functions: SU(2) vs. SU(3)," *Eur.Phys.J.* **C68** (2010) 165–181, `arXiv:1003.1960 [hep-ph]`.

[43] C. S. Fischer, J. Luecker, and J. A. Mueller, "Chiral and deconfinement phase transitions of two-flavour QCD at finite temperature and chemical potential," *Phys.Lett.* **B702** (2011) 438–441, `arXiv:1104.1564 [hep-ph]`.

[44] C. S. Fischer and J. Luecker, "Propagators and phase structure of Nf=2 and Nf=2+1 QCD," *Phys.Lett.* **B718** (2013) 1036–1043, `arXiv:1206.5191 [hep-ph]`.

[45] S. Hands, J. B. Kogut, M.-P. Lombardo, and S. E. Morrison, "Symmetries and spectrum of SU(2) lattice gauge theory at finite chemical potential," *Nucl.Phys.* **B558** (1999) 327–346, `arXiv:hep-lat/9902034 [hep-lat]`.

[46] R. Crewther, P. Di Vecchia, G. Veneziano, and E. Witten, "Chiral Estimate of the Electric Dipole Moment of the Neutron in Quantum Chromodynamics," *Phys.Lett.* **B88** (1979) 123.

[47] P. Harris, C. Baker, K. Green, P. Iaydjiev, S. Ivanov, *et al.*, "New experimental limit on the electric dipole moment of the neutron," *Phys.Rev.Lett.* **82** (1999) 904–907.

[48] M. E. Peskin and D. V. Schroeder, "An Introduction to quantum field theory,".

[49] V. Gribov, "Quantization of Nonabelian Gauge Theories," *Nucl.Phys.* **B139** (1978) 1.

[50] R. D. Pisarski and F. Wilczek, "Remarks on the Chiral Phase Transition in Chromodynamics," *Phys.Rev.* **D29** (1984) 338–341.

[51] R. Alkofer, M. Q. Huber, and K. Schwenzer, "Algorithmic derivation of Dyson-Schwinger Equations," *Comput.Phys.Commun.* **180** (2009) 965–976, `arXiv:0808.2939 [hep-th]`.

[52] G. Eichmann, A. Krassnigg, M. Schwinzerl, and R. Alkofer, "A Covariant view on the nucleons' quark core," *Annals Phys.* **323** (2008) 2505–2553, `arXiv:0712.2666 [hep-ph]`.

[53] C. Llewellyn-Smith, "A relativistic formulation for the quark model for mesons," *Annals Phys.* **53** (1969) 521–558.

[54] R. Cutkosky and M. Leon, "Normalization of Bethe-Salpeter Wave Functions and Bootstrap Equations," *Phys.Rev.* **135** (1964) B1445–B1446.

[55] N. Nakanishi, "Normalization Condition and Normal and Abnormal Solutions of the Bethe-Salpeter Equation," *Phys.Rev.* **138** (1965) B1182–B1192.

[56] P. Maris, C. D. Roberts, and P. C. Tandy, "Pion mass and decay constant," *Phys.Lett.* **B420** (1998) 267–273, `arXiv:nucl-th/9707003 [nucl-th]`.

[57] H. Pagels and S. Stokar, "The Pion Decay Constant, Electromagnetic Form-Factor and Quark Electromagnetic Selfenergy in QCD," *Phys.Rev.* **D20** (1979) 2947.

[58] J. Greensite, "An introduction to the confinement problem," *Lect.Notes Phys.* **821** (2011) 1–211.

[59] T. Kugo and I. Ojima, "Local Covariant Operator Formalism of Nonabelian Gauge Theories and Quark Confinement Problem," *Prog.Theor.Phys.Suppl.* **66** (1979) 1.

[60] T. Kugo, "The Universal renormalization factors Z(1) / Z(3) and color confinement condition in nonAbelian gauge theory," `arXiv:hep-th/9511033 [hep-th]`.

[61] **SESAM Collaboration** Collaboration, G. S. Bali, H. Neff, T. Duessel, T. Lippert, and K. Schilling, "Observation of string breaking in QCD," *Phys.Rev.* **D71** (2005) 114513, `arXiv:hep-lat/0505012 [hep-lat]`.

[62] J. I. Kapusta, "Finite temperature field theory,".

[63] S. Elitzur, "Impossibility of Spontaneously Breaking Local Symmetries," *Phys.Rev.* **D12** (1975) 3978–3982.

[64] S. R. Edwards, A. Sternbeck, and L. von Smekal, "Exploring a hidden symmetry with electrically charged quarks," *PoS* **LATTICE2010** (2010) 275, arXiv:1012.0768 [hep-lat].

[65] C. Gattringer, "Linking confinement to spectral properties of the Dirac operator," *Phys.Rev.Lett.* **97** (2006) 032003, arXiv:hep-lat/0605018 [hep-lat].

[66] F. Synatschke, A. Wipf, and C. Wozar, "Spectral sums of the Dirac-Wilson operator and their relation to the Polyakov loop," *Phys.Rev.* **D75** (2007) 114003, arXiv:hep-lat/0703018 [HEP-LAT].

[67] E. Bilgici, F. Bruckmann, C. Gattringer, and C. Hagen, "Dual quark condensate and dressed Polyakov loops," *Phys.Rev.* **D77** (2008) 094007, arXiv:0801.4051 [hep-lat].

[68] K. Morita, V. Skokov, B. Friman, and K. Redlich, "Probing deconfinement in a chiral effective model with Polyakov loop at imaginary chemical potential," *Phys.Rev.* **D84** (2011) 076009, arXiv:1107.2273 [hep-ph].

[69] E. Bilgici, F. Bruckmann, J. Danzer, C. Gattringer, C. Hagen, *et al.*, "Fermionic boundary conditions and the finite temperature transition of QCD," *Few Body Syst.* **47** (2010) 125–135, arXiv:0906.3957 [hep-lat].

[70] K. Kashiwa, H. Kouno, and M. Yahiro, "Dual quark condensate in the Polyakov-loop extended NJL model," *Phys.Rev.* **D80** (2009) 117901, arXiv:0908.1213 [hep-ph].

[71] K. Fukushima, "Relation between the Polyakov loop and the chiral order parameter at strong coupling," *Phys.Rev.* **D68** (2003) 045004, arXiv:hep-ph/0303225 [hep-ph].

[72] J. Braun, H. Gies, and J. M. Pawlowski, "Quark Confinement from Color Confinement," *Phys.Lett.* **B684** (2010) 262–267, arXiv:0708.2413 [hep-th].

[73] F. Marhauser and J. M. Pawlowski, "Confinement in Polyakov Gauge," arXiv:0812.1144 [hep-ph].

[74] L. Fister and J. M. Pawlowski, "Confinement from Correlation Functions," arXiv:1301.4163 [hep-ph].

[75] K. Osterwalder and R. Schrader, "Axioms for euclidean Green's functions," *Commun.Math.Phys.* **31** (1973) 83–112.

[76] R. Alkofer, W. Detmold, C. Fischer, and P. Maris, "Analytic properties of the Landau gauge gluon and quark propagators," *Phys.Rev.* **D70** (2004) 014014, `arXiv:hep-ph/0309077 [hep-ph]`.

[77] J. A. Mueller, C. S. Fischer, and D. Nickel, "Quark spectral properties above Tc from Dyson-Schwinger equations," *Eur.Phys.J.* **C70** (2010) 1037–1049, `arXiv:1009.3762 [hep-ph]`.

[78] J. A. Mueller, *A Dyson-Schwinger Approach to Finite Temperature QCD*. PhD thesis, TU Darmstadt, 2010.

[79] S.-x. Qin, L. Chang, Y.-x. Liu, and C. D. Roberts, "Quark spectral density and a strongly-coupled QGP," *Phys.Rev.* **D84** (2011) 014017, `arXiv:1010.4231 [nucl-th]`.

[80] S.-x. Qin and D. H. Rischke, "Quark Spectral Function and Deconfinement at Nonzero Temperature," `arXiv:1304.6547 [nucl-th]`.

[81] R. Alkofer, C. S. Fischer, F. J. Llanes-Estrada, and K. Schwenzer, "The Quark-gluon vertex in Landau gauge QCD: Its role in dynamical chiral symmetry breaking and quark confinement," *Annals Phys.* **324** (2009) 106–172, `arXiv:0804.3042 [hep-ph]`.

[82] C. S. Fischer and R. Williams, "Probing the gluon self-interaction in light mesons," *Phys.Rev.Lett.* **103** (2009) 122001, `arXiv:0905.2291 [hep-ph]`.

[83] L. Chang, Y.-X. Liu, and C. D. Roberts, "Dressed-quark anomalous magnetic moments," *Phys.Rev.Lett.* **106** (2011) 072001, `arXiv:1009.3458 [nucl-th]`.

[84] M. Hopfer, A. Windisch, and R. Alkofer, "The Quark-Gluon Vertex in Landau gauge QCD," *PoS* **CONFINEMENTX** (2013) 073, `arXiv:1301.3672 [hep-ph]`.

[85] E. Eichten and F. Feinberg, "Dynamical Symmetry Breaking of Nonabelian Gauge Symmetries," *Phys.Rev.* **D10** (1974) 3254–3279.

[86] J. S. Ball and T.-W. Chiu, "Analytic properties of the vertex function in gauge theories. 2.," *Phys.Rev.* **D22** (1980) 2550.

[87] C. S. Fischer and R. Williams, "Beyond the rainbow: Effects from pion back-coupling," *Phys.Rev.* **D78** (2008) 074006, `arXiv:0808.3372 [hep-ph]`.

[88] A. Maas, "The high-temperature phase of Yang-Mills theory in Landau gauge," `arXiv:hep-ph/0501150 [hep-ph]`.

[89] A. Maas, J. Wambach, and R. Alkofer, "The High-temperature phase of Landau-gauge Yang-Mills theory," *Eur.Phys.J.* **C42** (2005) 93–107, arXiv:hep-ph/0504019 [hep-ph].

[90] M. Q. Huber and L. von Smekal, "Gluon propagator at finite temperature,". To be published.

[91] C. S. Fischer and J. A. Mueller, "Quark condensates and the deconfinement transition," *PoS* **CPOD2009** (2009) 023, arXiv:0908.2530 [hep-ph].

[92] A. Cucchieri, A. Maas, and T. Mendes, "Infrared properties of propagators in Landau-gauge pure Yang-Mills theory at finite temperature," *Phys.Rev.* **D75** (2007) 076003, arXiv:hep-lat/0702022 [hep-lat].

[93] A. Maas, J. M. Pawlowski, L. von Smekal, and D. Spielmann, "The Gluon propagator close to criticality," *Phys.Rev.* **D85** (2012) 034037, arXiv:1110.6340 [hep-lat].

[94] R. Aouane, V. Bornyakov, E. Ilgenfritz, V. Mitrjushkin, M. Muller-Preussker, *et al.*, "Landau gauge gluon and ghost propagators at finite temperature from quenched lattice QCD," *Phys.Rev.* **D85** (2012) 034501, arXiv:1108.1735 [hep-lat].

[95] C. S. Fischer, A. Maas, and J. M. Pawlowski, "On the infrared behavior of Landau gauge Yang-Mills theory," *Annals Phys.* **324** (2009) 2408–2437, arXiv:0810.1987 [hep-ph].

[96] A. Maas, "Constructing non-perturbative gauges using correlation functions," *Phys.Lett.* **B689** (2010) 107–111, arXiv:0907.5185 [hep-lat].

[97] P. Buividovich, E. Luschevskaya, and M. Polikarpov, "Finite-temperature chiral condensate and low-lying Dirac eigenvalues in quenched SU(2) lattice gauge theory," *Phys.Rev.* **D78** (2008) 074505, arXiv:0809.3075 [hep-lat].

[98] M. Hopfer, M. Mitter, B.-J. Schaefer, and R. Alkofer, "A dual order parameter from fundamentally colour charged matter," *Acta Phys.Polon.Supp.* **6** (2013) 353–358, arXiv:1211.0166 [hep-ph].

[99] C. S. Fischer and R. Alkofer, "Nonperturbative propagators, running coupling and dynamical quark mass of Landau gauge QCD," *Phys.Rev.* **D67** (2003) 094020, arXiv:hep-ph/0301094 [hep-ph].

[100] C. S. Fischer, "Infrared properties of QCD from Dyson-Schwinger equations," *J.Phys.* **G32** (2006) R253–R291, arXiv:hep-ph/0605173 [hep-ph].

[101] M. Le Bellac, *Thermal Field Theory*. Cambridge University Press, 1996.

[102] T. K. Mukherjee, H. Chen, and M. Huang, "Chiral condensate and dressed Polyakov loop in the Nambu-Jona-Lasinio model," *Phys.Rev.* **D82** (2010) 034015, `arXiv:1005.2482 [hep-ph]`.

[103] G. Endrodi, Z. Fodor, S. Katz, and K. Szabo, "The QCD phase diagram at nonzero quark density," *JHEP* **1104** (2011) 001, `arXiv:1102.1356 [hep-lat]`.

[104] M. Pennington, "Strong Coupling Continuum QCD," *AIP Conf.Proc.* **1343** (2011) 63–68, `arXiv:1104.2522 [nucl-th]`.

[105] N. Brown and M. Pennington, "Studies of Confinement: How Quarks and Gluons Propagate," *Phys.Rev.* **D38** (1988) 2266.

[106] N. Brown and M. Pennington, "Studies of Confinement: How the Gluon Propagates," *Phys.Rev.* **D39** (1989) 2723.

[107] W. Weise, "Nuclear chiral dynamics and phases of QCD," *Prog.Part.Nucl.Phys.* **67** (2012) 299–311, `arXiv:1201.0950 [nucl-th]`.

[108] A. Andronic, P. Braun-Munzinger, and J. Stachel, "Hadron production in central nucleus-nucleus collisions at chemical freeze-out," *Nucl.Phys.* **A772** (2006) 167–199, `arXiv:nucl-th/0511071 [nucl-th]`.

[109] Z. Fodor, "Selected results in lattice quantum chromodynamics," *PTEP* **2012** (2012) 01A108.

[110] P. Gerber and H. Leutwyler, "Hadrons Below the Chiral Phase Transition," *Nucl.Phys.* **B321** (1989) 387.

[111] M. Blank and A. Krassnigg, "The QCD chiral transition temperature in a Dyson-Schwinger-equation context," *Phys.Rev.* **D82** (2010) 034006, `arXiv:1004.5301 [hep-ph]`.

[112] R. Aouane, F. Burger, E.-M. Ilgenfritz, M. Muller-Preussker, and A. Sternbeck, "Landau gauge gluon and ghost propagators from lattice QCD with Nf=2 twisted mass fermions at finite temperature," `arXiv:1212.1102 [hep-lat]`.

[113] O. Kaczmarek, F. Karsch, E. Laermann, C. Miao, S. Mukherjee, *et al.*, "Phase boundary for the chiral transition in (2+1) -flavor QCD at small values of the chemical potential," *Phys.Rev.* **D83** (2011) 014504, `arXiv:1011.3130 [hep-lat]`.

[114] P. de Forcrand and O. Philipsen, "The QCD phase diagram for small densities from imaginary chemical potential," *Nucl.Phys.* **B642** (2002) 290–306, `arXiv:hep-lat/0205016 [hep-lat]`.

[115] D. Toublan, "A Large N(c) perspective on the QCD phase diagram," *Phys.Lett.* **B621** (2005) 145–150, `arXiv:hep-th/0501069 [hep-th]`.

[116] J. Braun, B. Klein, and B.-J. Schaefer, "On the Phase Structure of QCD in a Finite Volume," *Phys.Lett.* **B713** (2012) 216–223, `arXiv:1110.0849 [hep-ph]`.

[117] J. Braun, "The QCD Phase Boundary from Quark-Gluon Dynamics," *Eur.Phys.J.* **C64** (2009) 459–482, `arXiv:0810.1727 [hep-ph]`.

[118] R. Alkofer, C. S. Fischer, and R. Williams, "U(A)(1) anomaly and eta-prime mass from an infrared singular quark-gluon vertex," *Eur.Phys.J.* **A38** (2008) 53–60, `arXiv:0804.3478 [hep-ph]`.

[119] A. Bender, D. Blaschke, Y. Kalinovsky, and C. D. Roberts, "Continuum study of deconfinement at finite temperature," *Phys.Rev.Lett.* **77** (1996) 3724–3727, `arXiv:nucl-th/9606006 [nucl-th]`.

[120] J. Braun, A. Eichhorn, H. Gies, and J. M. Pawlowski, "On the Nature of the Phase Transition in SU(N), Sp(2) and E(7) Yang-Mills theory," *Eur.Phys.J.* **C70** (2010) 689–702, `arXiv:1007.2619 [hep-ph]`.

[121] K. Fukushima and K. Kashiwa, "Polyakov loop and QCD thermodynamics from the gluon and ghost propagators," `arXiv:1206.0685 [hep-ph]`.

[122] C. S. Fischer, L. Fister, J. Luecker, and J. M. Pawlowski, "Polyakov loop potential at finite density," `arXiv:1306.6022 [hep-ph]`.

[123] L. Abbott, "The Background Field Method Beyond One Loop," *Nucl.Phys.* **B185** (1981) 189.

[124] N. Weiss, "The Effective Potential for the Order Parameter of Gauge Theories at Finite Temperature," *Phys.Rev.* **D24** (1981) 475.

[125] L. M. Haas, R. Stiele, J. Braun, J. M. Pawlowski, and J. Schaffner-Bielich, "Improved Polyakov-loop potential for effective models from functional calculations," `arXiv:1302.1993 [hep-ph]`.

[126] C. S. Fischer, D. Nickel, and J. Wambach, "Hadronic unquenching effects in the quark propagator," *Phys.Rev.* **D76** (2007) 094009, `arXiv:0705.4407 [hep-ph]`.

[127] D. Nickel, *Color-superconductivity from a Dyson-Schwinger perspective*. PhD thesis, TU Darmstadt, 2007.

[128] J. Mueller and C. Fischer, "Studying pion effects on the chiral phase transition," `arXiv:0811.2923 [hep-ph]`.

[129] C. S. Fischer and J. A. Mueller, "On critical scaling at the QCD $N_f = 2$ chiral phase transition," *Phys.Rev.* **D84** (2011) 054013, `arXiv:1106.2700 [hep-ph]`.

[130] C. S. Fischer, D. Nickel, and R. Williams, "On Gribov's supercriticality picture of quark confinement," *Eur.Phys.J.* **C60** (2009) 47–61, `arXiv:0807.3486 [hep-ph]`.

[131] V. Miransky, "On dynamical chiral symmetry breaking," *Phys.Lett.* **B165** (1985) 401–404.

[132] R. D. Pisarski and M. Tytgat, "Propagation of cool pions," *Phys.Rev.* **D54** (1996) 2989–2993, `arXiv:hep-ph/9604404 [hep-ph]`.

[133] D. Son and M. A. Stephanov, "Pion propagation near the QCD chiral phase transition," *Phys.Rev.Lett.* **88** (2002) 202302, `arXiv:hep-ph/0111100 [hep-ph]`.

[134] D. Son and M. A. Stephanov, "Real time pion propagation in finite temperature QCD," *Phys.Rev.* **D66** (2002) 076011, `arXiv:hep-ph/0204226 [hep-ph]`.

[135] J. Luecker, C. S. Fischer, and R. Williams, "Volume behaviour of quark condensate, pion mass and decay constant from Dyson-Schwinger equations," *Phys.Rev.* **D81** (2010) 094005, `arXiv:0912.3686 [hep-ph]`.

[136] K. Raya, A. Bashir, S. Hernández-Ortiz, A. Raya, and C. Roberts, "Multiple solutions for the fermion mass function in QED3," `arXiv:1305.2955 [nucl-th]`.